NTNU
Norwegian University of
Science and Technology

Behaviour of End plate connections of high strength steel subjected to bending moment

Firoz Feruzi Kassim

Foreword

This master thesis was conducted at the department of structural engineering at the Norwegian University of Science and Technology (NTNU) during the spring of 2016. This master thesis constitutes 20 weeks, which corresponds to 30 credit points.

This report deals with the capacity and the rotational stiffness of the end plate connections of high strength steel with rectangular hollow section, which is also a continuation of the previous student's work at the department of structural engineering. Laboratory tests were conducted to determine the capacity and the rotational stiffness of the end plate connections of high strength steel subjected to moment. The results obtained are then further compared to the results obtained from Abaqus CAE and hand calculations, which were done accordingly to NS EN 1993-1-8.

I would like to thank my supervisor Professor Arne Aalberg from the department of structural engineering, for good academic support during the development of this thesis. Furthermore, I would like to thank the engineer Steinar Seehuus, for assistance with the laboratory experiments.

Abstract

NS-EN 1993-1-8 is part of the Eurocode 3 series, which deals mainly with the design of joints in steel structures. It provides rules and procedures for calculating the capacity and the rotational stiffness of joints in a steel-framed structure. The sets of rules and guidelines provided in NS EN 1993-1-8 are mainly applied for structural joints connections with either H or I section and covering various steel grades from S 235 to S 460. Different types of connections such as in this case rectangular hollow sections with extended end plate connections are not covered in the Eurocode including structures with high strength steel. Therefore, this investigation focuses on examining the structural behaviour of end plate connections of high strength steel subjected to bending moment when applying the rules from the NS EN 1993-1-8.

Series of laboratory tests were conducted on two different joint specimens and both of them consisted of end plates that were made of high strength steel, i.e. Weldox 700. Numerical analyses of these tests were conducted in Abaqus CAE so as to observe the deformation patterns of the connection. The results obtained from the numerical simulations were compared to the experimental results and hand calculations from the Eurocode.

The comparisons shows that the hand calculations generally overestimates the initial stiffness obtained from the experiment depending on the specimen and it's bending axes.The numerical simulations substantially underestimates the initial stiffness from the experimental results, yet gives good prediction concerning other results. Both analysis models, i.e. the numerical simulation and hand calculation show that it's difficult to predict the initial stiffness.

The capacity calculations from both analysis models produces acceptable results that are within the range of the capacity obtained from the experiment.

A parameter study was conducted in the finite element program Abaqus CAE in order to determine the optimal number of elements within the thickness of the end plate. This was executed by assigning different volume elements (C3D8R and C3D20R) to the end plate, which was modelled as simply supported beam so as to determine the deflection in the middle. The deflection obtained in Abaqus was then compared to the analytical deflection.

Finally the Abaqus models, which were used in the numerical analysis in this investigation were evaluated to determine if the analysis produced were accurate. This was done by increasing the number of elements on the RHS profile and then comparing its results to the original Abaqus models that were used in this investigation.

Sammendrag

NS-EN 1993-1-8 er en del av Eurocode 3, som hovedsakelig beskriver regler og prosedyrer som gjelder for å beregne kapasitet og rotasjonsstivhet i knutepunkter i stålkonstruksjoner. Retningslinjene i NS EN 1993-1-8 gjelder i hovedsak knutepunkter for enten H eller I profiler, og dekker flere stålfastheter fra S 235 til S 460. Andre typer knutepunkter og konstruksjoner i høyfast stål, og i dette tilfellet rektangulære hulprofiler med endeplateforbindelser, dekkes ikke av Eurocoden. Det er derfor i denne rapporten lagt vekt på å undersøke ytelsen i endeplateforbindelser i høyfast stål, utsatt for bøyningsmoment etter retningslinjene i NS EN 1993-1-8.

Serier av laboratorieforsøk ble gjennomført på to forskjellige knutepunktsgeometrier, og begge disse hadde endeplater i høyfaststål (Weldox 700). Numeriske analyser av disse forsøkene ble kjørt i Abaqus CAE for å se flytemønstrene i forbindelsene. Resultatene fra disse simuleringene ble sammenlignet med eksperimentelle resultater og håndberegninger i NS EN 1993-1-8.

Sammenligningene viser at håndberegningene sjenerelt overvurderer den initielle stivheten som er beregnet utifra eksperimentene, avhengig av geometrien og dens bøyningsakse. De numeriske analysene undervurderer den initielle stivheten fra de eksperimentelle resultatene i stor grad, men gir allikevel gode anslag når det gjelder andre resultater. Begge analysemodellene, den numeriske simuleringen og håndberegningen, viser at det er vanskelig å forutse den initielle stivheten.

Kapasitetsutregningene fra både håndberegning og numeriske analyse gir akseptable resultater som ligger innenfor rammen for kapasitet som er regnet fra eksperimentet.

En parameterstudie ble gjennomført i Abaqus CAE for å finne det optimale antallet elementer i tykkelsen på endeplaten. Dette ble utført ved å legge til C3D8R- og C3D20R-elementer på endeplaten. Endeplaten var modellert som et fritt opplagt bjelke for å finne nedbøyning på midten. Nedbøyningen som ble funnet i Abaqus ble deretter sammenlignet med den beregnede nedbøyningen.

Til slutt ble Abaqus-modellene som ble brukt i de numeriske analysene i denne oppgaven, evaluert for å avgjøre om analysene var nøyaktige. Dette ble gjort ved å øke antallet volumelementer på hulprofilen og endeplaten, og så sammenligne disse resultatene med de opprinnelige Abaqus-modellene som ble brukt i oppgaven.

Table of Contents

vi

List of figures

List of tables

1 Introduction

NS-EN 1993-1-8 is part of the Eurocode 3 series which deals mainly with the design of joints in steel structures [1]. It provides rules and procedures for calculating the capacity and the rotational stiffness of joints in a steel-framed structure. The Eurocode classifies joints by either their strength or stiffness, which depends on the chosen method analysis and the classification of the joint. There is three types of global analysis method which are presented in chapter 3.

EC3-1-8 uses a component method of moment joint design, in which the characteristics of a joint can be determined from the properties of its basic components [1]. These basic joint components subjected to different forces are found on the Eurocode. Each of them are evaluated according to their application of rules set by the standard in terms of design resistance, stiffness coefficient and rotation capacity

The sets of rules and guidelines provided in NS EN 1993-1-8 are mainly applied for structural joints connections with either H or I section and covering various steel grades from S 235 to S 460 [1]. Therefore, this investigation focuses on examining the structural behaviour of high strength steel end plate connections subjected to bending moment when applying the rules from the NS EN 1993-1-8.

Brief introduction of the yield line theory for transverse loaded plates are provided on chapter 4, which is the basis of the hand calculations concerning the connections plastic moment capacity and emerging yield line patterns when the end plate is subjected to tension. Different possible yield mechanisms of the connection are investigated also in chapter 7. Furthermore, relevant chapters from the Eurocode, which are the basis of rotational stiffness calculations are also presented on chapter 4.

Chapter 5 gives a brief introduction of the test specimens and the laboratory procedures taken to obtain the required results. The initial stiffness and the capacity of different test specimens were obtained by conducting elastic and plastic procedures respectively, which are then presented on chapter 6.

The results obtained from the hand calculations, which were done accordingly to NS EN 1993-1-8 and the basis of the yield line theory presented on chapter 4 are presented in chapter 7. Furthermore, the comparisons between the hand calculations and the experimental results are made and discussed on chapter 8.The numerical analysis were conducted by simulating the laboratory tests presented in chapter 9 and the results obtained were compared to the experimental results and discussed on chapter 10. The rotational stiffness and the capacity of the specimens were the main criterion for assessing the comparisons of the hand calculations and numerical analysis to the laboratory test. Discussions about the uncertainties observed from these comparisons are also made.

The parameter study was conducted in this investigation, which is presented on chapter 11 to determine an optimal number of elements across the thickness of the end plate. Furthermore, the resolution of the problem that occurred during the numerical analysis are presented and discussed.

2 Previous work

2.1 General

The sets of rules and guidelines provided in NS EN 1993-1-8 are mainly applied for structural joint connections with either H or I section and also covering various steel grades from S 235 to S 460. Different types of connections such as the hollow sections with both end plate connections and splice connections are not covered in the Eurocode including structures with high strength steel. Therefore, different theses from the previous students have focused on the structural behaviour of such joint connections when subjected to axial tension or bending moment. Most students determined the joint connections' capacities and rotational stiffness by conducting hand calculations based on the Eurocode, numerical analysis and laboratory experiments with chosen geometries. The following chapters presents the relevant students' work, which are relevant to this investigation.

2.2 Work of Fredrik Torp Karlsen

Fredrik Karlsen's master from 2011 deals with end plate joints with rectangular hollow sections which are bolted to each other in a splice connection [2]. The connection is subjected to axial tension with constant speed on the upper end while the lower end is firmly attached to the machine. His objective of the thesis was to determine how NS EN 1993-1-8 predicts the stiffness of the joint by component method and how well the yield line mechanisms model the capacity.

He had conducted numerical analysis, hand calculations and laboratory test in order to determine the capacity and the stiffness of the joints. This involved 6 test specimens whereby 4 of them had 4 bolts and the 2 other specimens had 8 bolts in the joints. He concluded that the specimens with 4 bolts had the same failure mechanism as predicted by the T-stub model of Eurocode, which wasn't the same case for joints with 8 bolts. In addition, the numerical FE simulations results were consistent with the experiment's response for all the specimens concerning their stiffness while the Eurocode model overestimates the values too high.

2.2.1 Karlsen's model

Karlsen's thesis has led to other students following his experimental framework and conducting further analysis with different geometries [3]. The results obtained were made compared to Karlsen's results so as to observe how the various parameters affect the result. Since most of these students dealt with end-plates with steel strength (quality) of S355, some of them incorporated end-plates of high strength steel into their research.

Inger-Marie Torstvedt and Bjørg Edvardsen Egeland [4] conducted their thesis in 2013, which dealt with the similar work as Karlsen that is splice connections with rectangular hollow section (RHS) subjected to axial tension. The main purpose of their work was to investigate how accurate the Karlsen stiffness model is compared to the NS-EN 1993-1-8 [1] when calculating the capacity and stiffness of the RHS. They cooperated with Lauknes concerning end plates made of high strength steel that is Weldox 700.

Kristian Lauknes' thesis from 2013 also dealt with this subject matter involving splice connections with end-plates made up of both Weldox 700 and S355.The three specimens of splice connections consisted of a HUP section with Weldox 700 and two H-sections with

both Weldox 700 and S355 and all of them were subjected to axial tension. Lauknes had retrieved HUP –S355 profile from Egeland and Torstvedt [4] so as to compare its effect to HUP-W700.He observed that the Eurocode model underestimated the capacities of H- and HUP sections for both steel qualities while the numerical FE model overestimated. Both these models were compared to the results from the laboratory tests. In stiffness' case, the Eurocode gave conservative results by overestimating the stiffness of all specimens and the profile sections that had Weldox 700 qualities where stiffer than their counterparts with S355. Lauknes had proposed a reduction factor for connections with high strength steel quality so as reduce the utilization capacity to the level closer to S355.

Lauknes also cooperated partly with Egeland and Torstvedt in 2013. Although high strength steel was not their main subject, they focused partially on the effects of using the end-plates with high strength steel quality has on the joints stiffness in splice connection [4]. Egeland and Torstvedt had a HUP profile with end plates of S-355 and its effects obtained from the laboratory tests were compared to Lauknes' HUP profile with end plate of Weldox 700. They concluded that splice connections joints with high strength steel end-plates had 40% higher initial stiffness compared joints with steel quality of S355. The increased stiffness was due to the change in the material properties of the end-plate.

Knutsen and Oma also dealt with splice connections in 2014 [5], which consisted of hollow sections with end-plates of both S355 and Weldox 700. Their main subject of interest was calculating the initial stiffness through the processes of numerical FE analysis, laboratory tests and hand calculations based on NS EN 1993-1-8. They had also conducted a parameter study in Abaqus dealing with curvatures in the plates caused by welding and pre-tensioning of the bolts. The effects of these properties of the end plates and bolts yielded a doubling of initial stiffness.

The laboratory tests were conducted with 4 test specimens which had two different joints geometries and each of them had end-plates with steel grades of S355 and Weldox 700. These specimens were also subjected to axial tension.

The results from the numerical analysis were compared to experimental-and hand calculations results. Knutsen and Oma concluded that numerical simulations underestimates the initial stiffness compared to the experimental results with huge margin but the rest of the response were consistent with each other. They reckoned that Eurocode also underestimates the initial stiffness and its capacity calculations gave conservative results for both splice connections with S355 and Weldox 700.

2.3 Work of Ina Birkeland

Ina Birkeland conducted her master thesis in 2011, which was approximately a year after the NS EN 1993 was officially made the only valid standard for the design of steel structures in Norway [6]. Previously it has been common to assume that a joint was usually classified as either pinned or rigid. Many researches continued to prove that structural joint's behaviour observed would lie somewhere between nominally pinned and continuous (rigid) boundaries. Therefore a new boundary was included in NS EN 1993-1-8, which is semi-rigid.

This led Birkeland to evaluate the credibility of the Eurocode 3 when it comes to structural joints in portal frames. Birkeland investigated how the classification boundaries were derived and analysed how these affect the resulting moment-and deflection distributions for portal frames with different geometries.

She initially demonstrated how the classification boundaries for stiffness of the beam column joints in the Eurocode was obtained by observing a portal frame with pinned supports at the column bases. The vertical loads were applied at the top of both columns. The structural behaviour of the portal frame was analysed with and without bracing system. The dimensionless parameters such as $\hat{c}$ and ρ were imposed from the relationship between the portal frame's buckling and plastic capacity. In order to classify when a joint can be considered rigid, whereby $\hat{c}$ is the relative joint stiffness and ρ is the ratio between the flexural stiffness of the beam and column.

Since the classification boundaries is derived in terms of plastic capacity setting, Birkeland investigated if the boundaries set by the Eurocode was consistent with the elastic design parameters. By doing so the structural analysis of the portal frames with different geometries of rigid beam-column and rigid column-base joints was conducted in Focus construction frame program with linear elastic analysis. The program was used to monitor the deviation in moment and displacement from an infinitely rigid frame to rigid frame obtained the Eurocode. Furthermore, the dimensionless parameters and the 5 % criterion are factors which defined if a frame with and without bracing system was rigid. The 5% criterion is defined as the percentage change from a frame with infinitely rigid corners to having a rigid corner, which is defined by the Eurocode is less than 5%. These factors assures that that the elastic requirements are satisfied.

Ina Birkeland's main conclusions were that the beam-column joints can be classified as rigid when $\rho > 2$ is satisfied but smaller ρ will give non conservative results.

Whereas the beam-column joints can be classified by its stiffness in terms of the three boundaries this is not same case for column-base joints. The Eurocode does not provide the pinned limit for the column bases. Birkeland numerically analysed the rotational stiffness of a column base, which consisted of two anchor bolts and a base plate. The Abaqus results showed that the rotational stiffness of the pinned column base joints was much greater than the pinned limit. Therefore all column-bases would be classified as semi-rigid and the pinned limit would be unnecessary.

2.3.1 Work of Arne Martin Uhre

Arne Martin Uhre's master thesis from 2014 is a continuation of Ina Birkeland's master thesis which deals with elastic global analysis of a one-storey (portal) frame [7]. He focuses on the elasticity factors of a two-story frames by evaluating its moment and displacement when a frame is exposed to different load combinations and stiffness changes. In addition, he also focuses on classification boundaries of a column base.

Uhre points out that the standard's classification boundaries for joints were developed from the capacity of a simple frame and elasticity factors such as displacement and moment were not taken into consideration. Therefore he assess if the classification boundaries corresponds well with the elastic analysis for a two-storey frame.

Uhre concluded that the percentage change of the elastic parameters values decreases for both unbraced and braced as the graph converges to zero as ρ increases. These values obtained are relatively similar to Birkeland's results. The slight difference was that Birkeland's results were more conservative than Uhre's. Therefore Uhre points out that the 5 % criterion should be revaluated when dealing with multi-storey frames.

Furthermore, he researches whether a stiffness boundary classification for a nominally pinned column base is needed since NS-EN 1993-1-8 does not consider it. Uhre investigates this by calculating the capacity and rotational stiffness of an ideal pinned column base consisting of two bolts and an endplate. The calculations are based on the standard and the results are compared to the ones obtained in the experiments.

Series of laboratory experiments were conducted on the column base, which is anchored horizontally as a cantilever beam to a stiff wall by two bolts on each side of the extended end plate that is welded to a hollow section. The capacity and the rotational stiffness of the column base was determined by placing load on the tip of the hollow section beam in both major and minor axis. The rotation and deflection of the column during bending was recorded by a clinometer and a tape measure.

The results obtained from the experiment showed that a pinned column base had a much higher rotational stiffness in both axis compared to the limits defined according to the NS EN 1993-1-8. Therefore a pinned boundary was also unnecessary as Birkeland's numerical results showed.

Finally, a linear elastic analysis was conducted between a two-story frames with an infinitely rigid column base and a column base with varying stiffness. The focus construction program was used to analyse how a frame with hollow profile behaves with known column base stiffness values, which were obtained from the experiments and the Eurocode. Uhre concluded that the loading on either weak or strong axis of the joint has a big effect on the moment in the column base and the horizontal deflection of the frame. In addition, a frame with flexural stiffness ratio of $\rho = 0{,}47$ satisfied the 5 % criterion.

2.3.1.1 Uhre's model

Thomas Bringsvor [8] and Eirik Kirkerud [9]conducted their master thesis separately in 2015. They dealt with examining the response and behaviour of an end-plate connections which consists of a bolted joints of hollow sections with welded end-plates when exposed to bending moment. They followed Uhre's procedure whereby a point load was placed at the tip of the cantilevered hollow profile. The numerical FE simulations, hand calculations and the laboratory experiments processes had been conducted from this model. The joint's capacity and stiffness properties are retrieved through these processes when calculating bending moment about the weak and strong axis of the cantilevered beam in each loading cases.

In Bringsvor's case the cantilevered end-plate connection had three different geometries one being the main model which is similar to Uhre's in terms of geometry of the column base. The second geometry has a thinner end plate compared to the main model. The third geometry's endplate has the same thickness as the main model. The only difference between the two is that the second geometry has two bolts which are further placed from each other.

Bringsvor concluded that the main model had overall the highest stiffness and capacity based on numerical simulations. The third geometry had both higher capacity and stiffness in the strong axis than the second geometry. These results were only consistent with the experimental results. The hand calculations gave conservative results whereby the moment-capacity and stiffness for both strong-and weak axis were overestimated.

Eirik Kirkerud had used 4 bolts in his end-plate connections instead of two as Uhre and Thomas did. Two of these bolts where placed on each side of the extended end-plate. Eirik had two column bases with different end-plate thicknesses at 8 mm and 6 mm.

The results from each cases were compared and evaluated. Eirik observed the results of moment capacity of the joints for both models were similar in the elastic part but not as precise as the plastic capacity part. He points out that Abaqus model can be used as a good reference model but it does not give favourable results as the laboratory tests does. He also conducted several Abaqus simulations and hand calculations to determine the rotational stiffness about the weak and strong axis of two other alternative geometries of end-plates with varying thickness between 4 and 10 mm.

He observed that the results from both calculation models were consistent with each other at thinner end-plates but it continued to deviate more as the plate thickness increased. A stiffness reduction factor of 0,5 gave better results with less deviation but he was unable to justify if this factor could be used as part of joint design due to lack of basis to support it.

3 Analysis, classification and modelling

3.1 General

This chapter deals with the rules presented in NS EN 1993-1-8 concerning the classification and the analysis of a joint. The NS-EN 1993-1-8 is a standard Eurocode 3 which deals mainly with the design of joints in steel structures [1]. It provides rules and procedures for calculating the capacity and the rotational stiffness of joints in a steel-framed structure.

There are three simplified joint models according to the moment-rotation behaviour, which are;

- Simple (Pinned), whereby the assumption is that the joint does not transmit bending moments.
- Continuous (Rigid), whereby the joint transmits bending moments with zero rotation. This has no effect on the analysis.
- Semi-continuous (semi-rigid), the joint behaves partially as simple and continuous. This needs to be taken into account in the analysis.

These models are demonstrated on the diagram below:
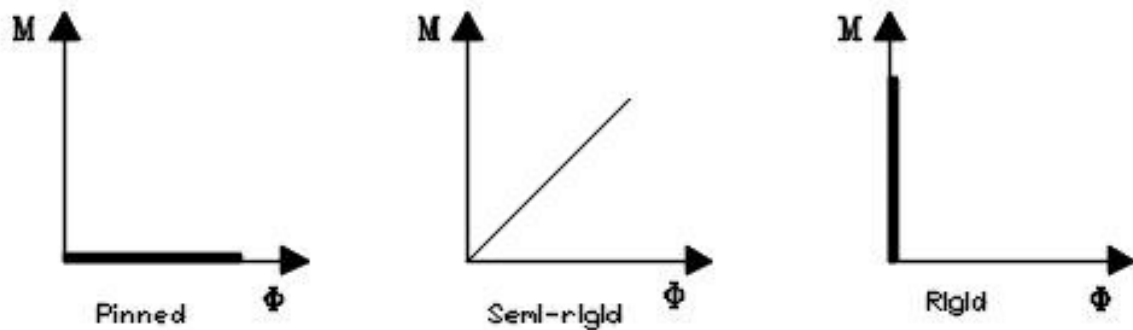
Figure 3.1: Simplified joint model

3.2 Global analysis

The Eurocode classifies joints by either their strength or stiffness, which depends on the chosen method analysis and the classification of the joint. There is three types of global analysis method which are presented on the following subchapters and the table 3.1 and each of them have its own classification of the joint.

Method of global analysis	Classification of joint		
Elastic	Nominally pinned	Rigid	Semi-rigid
Rigid-Plastic	Nominally pinned	Rigid and full strength	Partial strength
Elastic-Plastic	Nominally pinned	Rigid and full strength	Semi-rigid and partial strength Semi-rigid and full strength Rigid and partial strength
Type of joint model	Simple	Continuous	Semi-continuous

Table 3.1: Type of joint model

3.2.1 Elastic global analysis

The structural analysis assumes that the steel joints in this region have a linear strain-stress behaviour and it said to be reversible. It should be classified according to their rotational stiffness including having a sufficient strength to transmit the forces and moments acting at the joints resulting from the analysis.

The rotational stiffness of a semi-rigid joint is shown in the moment-rotation graph, which is also known as $M - \varphi$ curve shown in figure...
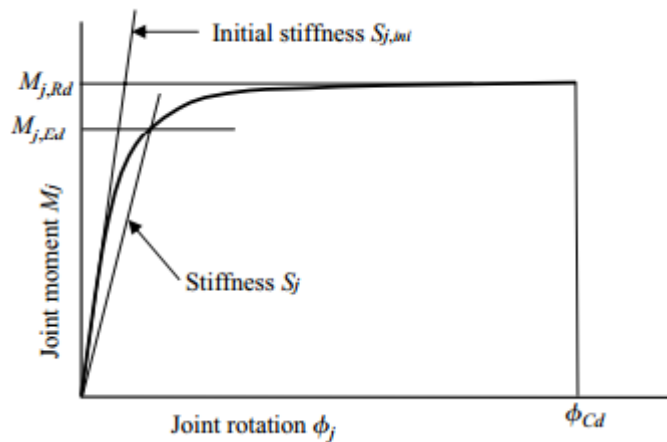
Figure 3.2: Characteristics of a moment joint

The graph is considered linear elastic if $M_{j,Ed}$ does not exceed $2/3M_{j,Rd}$ and the rotational stiffness in this region is known as initial rotational stiffness $S_{j,ini}$ shown in fig a. On the other hand the rotational stiffness may be taken as $S_{j,ini}/\eta$ in the analysis as a simplification to $M_{j,Ed} \leq 2/3M_{j,Rd}$, for all values of the moment $M_{j,Ed}$ shown in fig b. η is the stiffness modification coefficient and it is equal to 3 for the column base.
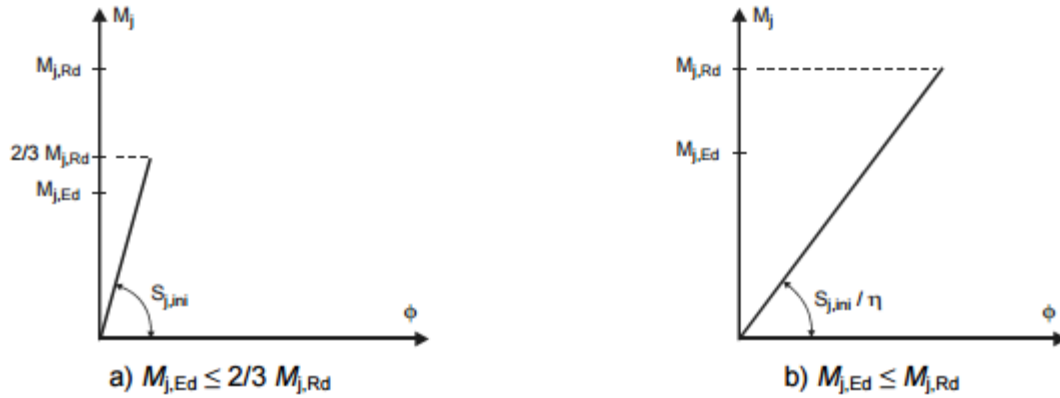
Figure 3.3: Rotational stiffness for elastic global analysis

3.2.1.1 Classification boundaries for joints

The joints may be classified as rigid, semi-rigid or nominally pinned in the elastic global analysis according to its rotational stiffness. This is done by comparing its initial rotational stiffness $S_{j,ini}$ with the classification boundaries shown on figure 3.4.

Figure 3.4: Classification of joints by stiffness
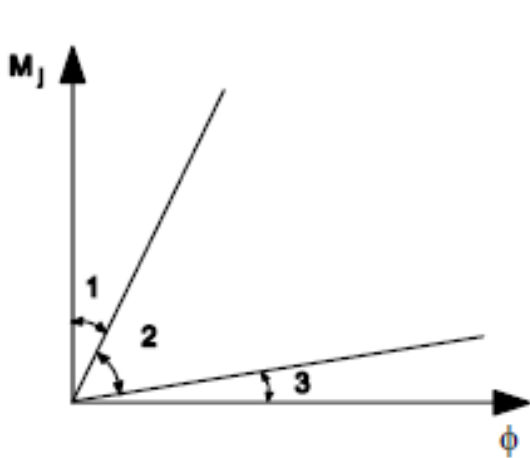
Zone 1: rigid, if $S_{j,ini} \geq \frac{k_b E I_b}{L_b}$

Where:

- $k_b = 8$ for frames where the bracing system reduces the horizontal displacement by at least 80%
- $k_b = 25$ for other frames provided that in every storey $\frac{K_b}{K_c} \geq 0{,}1$

Zone 2: Semi-rigid

Joints that do not meet the requirements of either zone 1 or zone 2 are classified as semi-rigid.

Zone 3: Nominally pinned,

Joints are classified as nominally pinned if $S_{j,ini} \leq 0{,}5 \frac{E I_b}{L_b}$

The rules for determining $S_{j,ini}$ are only applied to joint connections with H or I sections, which are found in clause 6.3.1. The determination of $S_{j,ini}$ for joints with hollow sections are not provided in the standard. Yet, it states that the joint may be classified on the basis of experimental evidence of previous satisfactory performance in similar cases or by calculations based on test evidence.

3.2.1.2 Classification of column bases

The standard only provides a rigid classification of a column base and not the pinned. The reason for this is looked in depth by Ina Birkeland [6] and Arne Uhre Martin [7].

These are the boundaries presented by the standard:

- Frames with bracing system that reduces the horizontal displacement by at least 80% and where the effects of deformation may be neglected:
  - if $\lambda_0 \leq 0,5$;
  - if $0,5 < \lambda_0 < 3,93$ and $S_{j,ini} \geq 7 (2 \lambda_0 - 1) EI_C/L_C$;
  - if $\lambda_0 \geq 3,93$ and $S_{j,ini} \geq 48 EI_C/L_C$
- Otherwise if $S_{j,ini} \geq 30 EI_C/L_C$.

  Where:

λ_0 is the slenderness of a column in which both ends are assumed to be pinned;

I_c, L_c are as given in figure 3.4

3.2.2 Rigid-plastic global analysis

The joints in the rigid-plastic global analysis are classified according to their strength as full-strength, nominally pinned or partial strength. The process is done by comparing its design moment resistance $M_{j,Rd}$ with the design moment resistances of the component members in the joint connection.

The joints in this analysis needs to meet these criteria so as to be classified:

Nominally Pinned joints: when $M_{j,Rd}$ is not greater than 0,25 times the design moment resistance required for a full-strength joint, provided that it also has sufficient rotation capacity: $M_{j,Rd} \leq 0,25 M_{j,Rd}$

Full-strength joint: The design resistance of a full strength joint should not be less than that of connected members $M_{j,Rd} \geq M_{full-strength}$

Partial-strength joints: A joint that neither meets the criteria of full-strength joint nor a nominally pinned joint: $0,25 M_{j,Rd} < M_{j,Rd} < M_{full-strength}$

3.2.3 Elastic-plastic global analysis

In the case of elastic-plastic global analysis, the joint are classified according to both stiffness and strength. The standard provides the rules to determine the static design resistances of joint connections with hollow sections in section 7.Furthermore, the connections with H or I sections are classified according to the values of $M_{j,Rd}, S_j$ and $\emptyset_{cd}$.

These moment-rotation characteristic of the joints are used to determine the distribution of internal forces and moments. Figure 5.2 shows the simplification of the bi-linear design moment rotation characteristic.
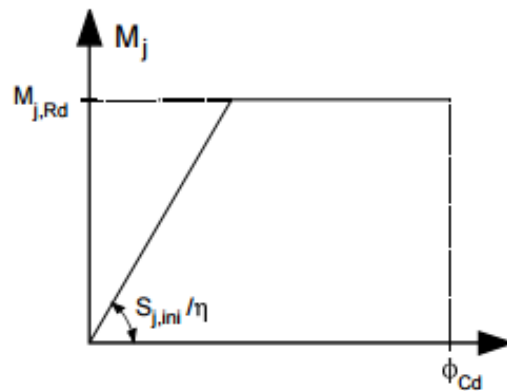
Figure 3.5: Simplified bi-linear design moment-rotation characteristics

4 Basis of design

4.1 General

This chapter deals briefly with the principles of yield mechanism and capacity in steel plates subjected to loads, which is determined by using the yield line theory. Most of these contents are obtained from different academic journals and the designs of steel construction by Per Kristian Larsen [10].

4.2 Yield line theory for transverse loaded plates

The yield line theory was developed by K.V Johansen so as to determine the collapse load of reinforced concrete slabs and it is based on the theory of plasticity. This theory can be applied to structures or materials that can be described as rigid perfectly plastic. This requires the absence of large deformations, ensuring that elastic strains can be neglected, and adequate ductility [11].

The plasticity theory aims to predict the collapse load of structure by means of the three limit analysis theorems: upper bound, lower bound and uniqueness. The yield line theory is based on the upper bound theorem and this can be applied to concentrated loaded plates that obey yield conditions such as Tresca and von Mises. Such plates can also be analysed by yield lines. Yield line analysis provides non-conservative solutions unless correct mechanisms are chosen [11].

4.2.1 Kinematic mechanism

When a plate is uniformly loaded plastic hinges are formed as straight lines which are known as yield lines. The assumption of the yield line theory is that during failure the increase of plastic deformation is concentrated in a number of yield lines. The parts bounded by those lines and plate edges is where the plastic deformation does not change, i.e. plates remain plane between yield lines. Since, the elastic deformation also remains constant, these parts of the plate behave like rigid bodies. The yield lines formed on the plate are permanent and do not disappear after unloading. When the loading on the plate continues yield lines develops in patterns, which is known as a mechanism. Hence the maximum load capacity is reached. [12]
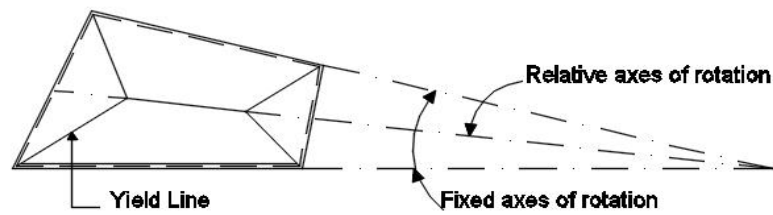
Figure 4.1: Fixed and relative rotational axis *[10]*

According to the upper-bound theorem, if the shape of the failure mechanism is known, the failure load can directly be obtained with the principle of virtual work. On a plate in the state of failure, a small plastic deformation is imposed and the resulting work performed by the external loads and the internally dissipated energy are calculated [12].

The expression of the external and internal plastic work are respectively $W_{ext} = M_p \emptyset$ and $W_{int} = \sum m_p l\theta$. The yield moment m_p is equal to $0{,}25t_p^2 f_y$. These expression were obtained by considering a uniformly loaded plate segment, which is freely supported along CD and the yield line is apparent along AB [10].
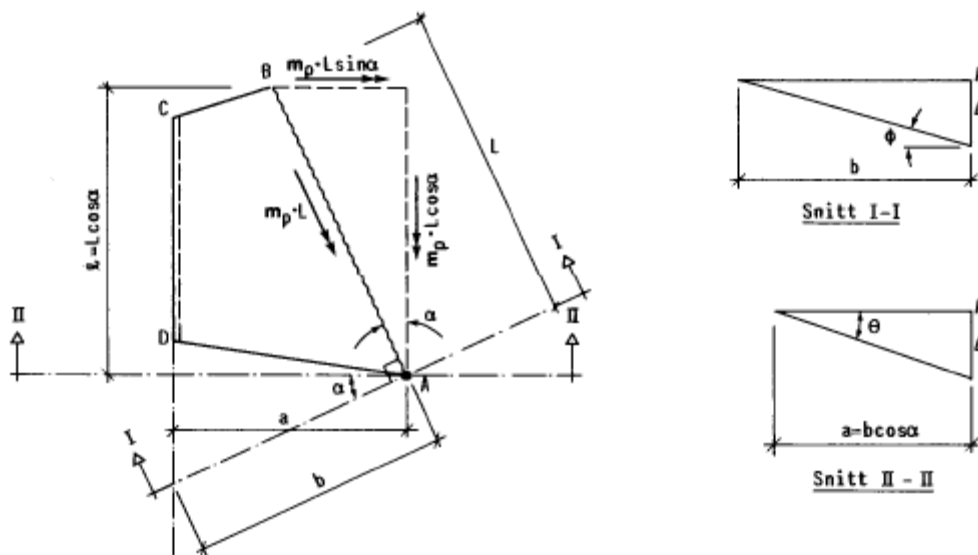
Figure 4.2: Skew yield line with regard to support axis of rotation

4.2.2 Yield criterion for plates

The Yield line criterion defines the strength of a given slab element subjected to a general moment field [13] and this criterion can be applied to bending plates. is solely based on bending moments [10].

In order to implement the yield criterion, the plate's membrane forces and shear forces are neglected and small displacements are assumed. These assumptions leads to the von Mises criterion that is being able to express the initial yielding in terms of bending moments as formulated on the expression (4.1) and m_y is the moment per unit length [10]:

$$M_x^2 + M_y^2 + 3M_x M_y = \left(\frac{1}{6}t^2 f_y\right)^2 = m_y^2 \tag{4.1}$$

The expression (4.2) demonstrates the full plasticity (yielding) across thickness of the plate [10]

$$M_x^2 + M_y^2 + 3M_x M_y = \left(\frac{1}{4}t^2 f_y\right)^2 = m_p^2 \tag{4.2}$$

If the plate's moments are transformed into principal moments M_1 and M_2 in the same procedure as principal stresses then (4.2) can be expressed as:

$$M_1^2 + M_2^2 - M_1 M_2 = m_p^2 \tag{4.3}$$
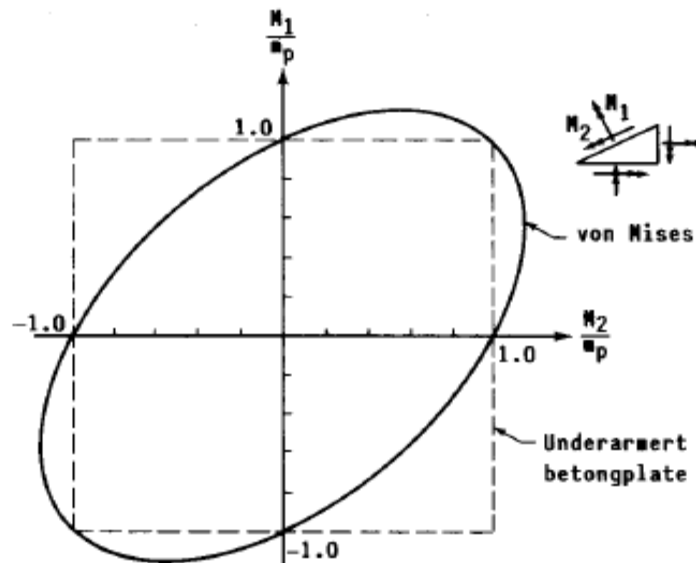
Figure 4.3: Yield criterion for plates

The von Mises criterion shows that a plate can resist moments that are normal M_1 and parallel M_2 to the yield line being equal to or larger than m_p when acting in the same direction. If they act in the opposite direction due to stress combinations (tension-compression or compression-tension) this leads to hardening of the steel and development of membrane forces. This is due to m_p giving non-conservative results.

14

Therefore the criterion is only applied to moments acting in the same direction and thus neglecting membrane forces and shear forces as mentioned earlier.

4.3 Design resistance for structural joints

4.3.1 General

This chapter deals with the use of the NS EN 1993-1-8 when calculating the strength and capacity of structural joints with end-plate connections. Most of the information presented in this chapter are obtained from the standard [1].

4.3.2 Component method

EC3-1-8 uses a component method of moment joint design, in which the characteristics of a joint can be determined from the properties of its basic components [1]. These basic joint components are generally displayed in tables 6.1 and 6.11 based on their load situations.

Each of them are evaluated according to their application of rules set by the standard in terms of design resistance, stiffness coefficient and rotation capacity. For instance, the calculation of the capacity and the rotational stiffness for an end-plate in a joint connection subjected to bending is found in 6.2.6.5 and 6.3.2 respectively.

4.3.3 Equivalent T-stub in tension

A structural joint with bolted connections exposed to tension may be used by an equivalent t-stub as shown on figure (4.4) to model the design resistance of the following components:

- Column flange in bending
- End-plate in bending
- Flange cleat in bending
- Base plate in bending under tension.
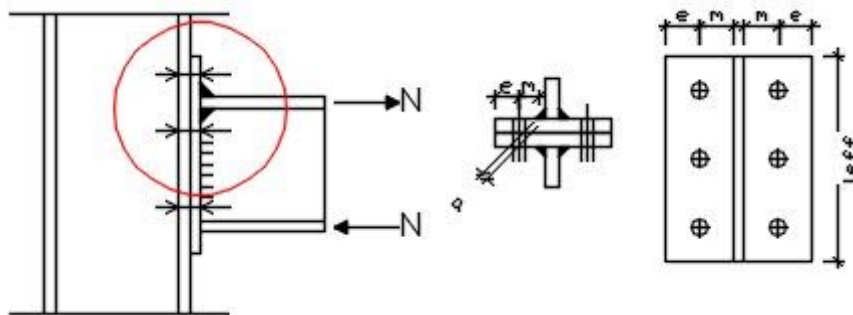
Figure 4.4: Bolted connections

The t-stub model in EC3-1-8 is applied to connections with H and I sections [1]. Therefore assumptions and modifications are made so as to apply the t-stub model to connections with hollow sections, which is dealt in depth in chapter 7.

4.3.4   Capacity for equivalent T-stub

The resistance of the equivalent T-stub in tension are calculated for three possible modes of failure. The design resistance formulas for each possible for modes are displayed in table 6.2 in the Eurocode [1].The resistance is taken as the minimum of the values for the three modes. Only mode 1 and 2 experiences prying actions and this occurs when the T-stub is under tensile loading, both bolts hold the parts in place and compressive prying actions develops at both edges of the bending flange as shown on figure 4.5.Past students have shown how the resistances formulas [7] [9] [2]are derived and therefore these modes are displayed briefly below with B_{Rd} as the tension resistance for the bolts and Q represents the prying forces:
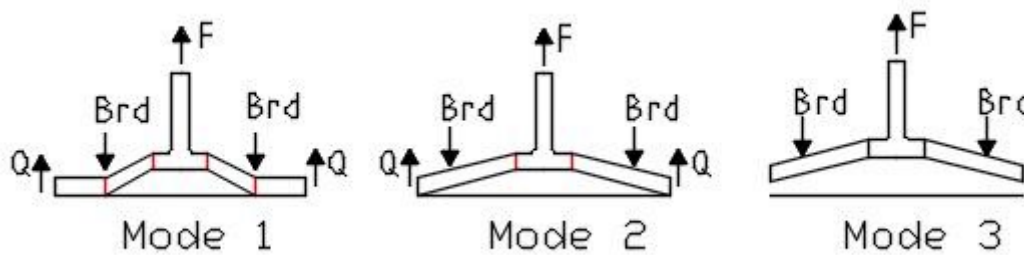
Figure 4.5: Failure mechanisms

Mode 1 complete flange yielding

This form of failure mode occurs when plastic hinges develops in the flange where both bolts are placed and in both web-flange junction as demonstrated in figure by a red line... The T-stub in this case experiences complete flange yielding and its capacity is determined from this equation in this investigation:

$$F_{T,1,Rd} = \frac{4M_{pl,1,Rd}}{m} \tag{4.4}$$

Mode 2 Bolt failure with flange yielding

In this case the plastic hinges also develops at the T stub web-flange junction as demonstrated on the figure by two red lines. The flange does not completely yield but bolts failure occurs. The capacity of the T-stub flange is determined from this equation, which is the combination of the bolt's-and the plate's capacity.

$$F_{T,2,Rd} = \frac{2M_{pl,2,Rd} + n\sum F_{t,Rd}}{m + n} \tag{4.5}$$

16

Mode 3 Bolt failure

There is no initial yielding in the T-stub flange, the bolts experiences failure due to rupture under tensile loading. Therefore the capacity in mode 3 is only calculated for the bolts as demonstrated in the equation.

$$F_{T,2,Rd} = \sum F_{t,Rd}$$

(4.6)

4.3.5 Effective lengths

The effective length is an equivalent length that gives us a good estimate for capacity when we apply the equivalent T-stub design model. The effective length is not equivalent to the physical length of the joint of interest.

The Eurocode groups yield lines mechanisms into two types based on their differences in shapes on T-stub flanges' surface, which are circular and non-circular. The T-stub flanges effective length of these yield lines mechanism are represented respectively as circular patterns ($l_{eff,cp}$) and non-circular patterns ($l_{eff,np}$).

The effective length of an equivalent T-stub is calculated for each of the possible yield line patterns as displayed on figure 4.6 and 4.7 [1]. That are relevant to the location of a bolt row in a joint, which in this case is the bolt row outside tension flange of beam. The smallest value of the effective lengths corresponding to all possible yield lines mechanisms in the specific T-stub flange is chosen. The chosen effective length is then used to calculate the plastic moment capacity of the T-stub shown on expression:

$$M_{pl,i,Rd} = W f_y = \frac{bh^2 f_y}{4\gamma_{Mo}} = \frac{l_{eff} t_p^2 f_y}{4\gamma_{Mo}} \tag{4.7}$$

The value obtained is then later used to calculate the design resistance for each modes as shown formula on figure 4.4 and 4.5.

Bolt-row location	Bolt-row considered individually	
	Circular patterns $\ell_{eff,cp}$	Non-circular patterns $\ell_{eff,nc}$
Bolt-row outside tension flange of beam	Smallest of: $2\pi m_x$ $\pi m_x + w$ $\pi m_x + 2e$	Smallest of: $4m_x + 1,25e_x$ $e + 2m_x + 0,625e_x$ $0,5b_p$ $0,5w + 2m_x + 0,625e_x$

Table 4.1: The effective lengths of an end-plate

The figure below demonstrates a pair of bolts in endplates with relevant yield mechanisms and the effective lengths corresponding to these yield patterns are given in table 6.6 and shown on figure 4.6 and 4.7 [10].
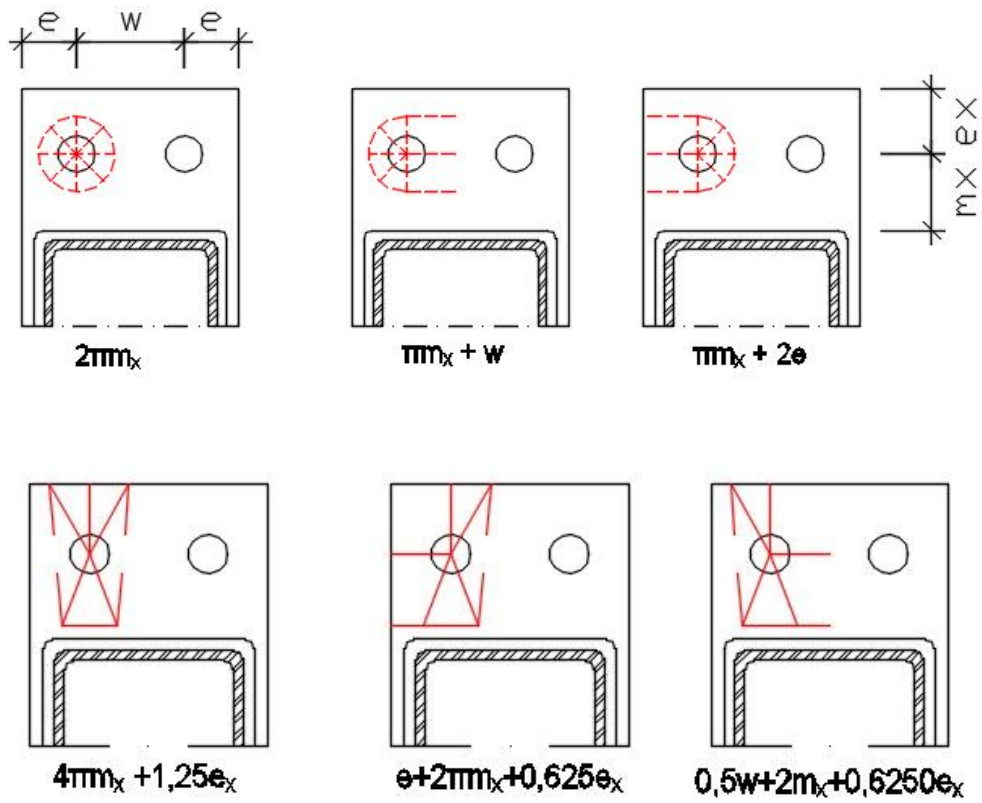
Figure 4.6: Yield mechanisms in end-plates with circular and non-circular patterns
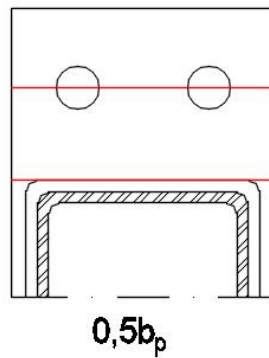
Figure 4.7: The relevant yield pattern

Figure 4.7 shows the possible yield patterns when both specimens are bent about the strong axis. This is based on the previous students' experimental observation. This yield pattern is dealt with in chapter 7.2.

4.4 Rotational stiffness

4.4.1 General

According to the Eurocode the rotational stiffness of a joint should be determined from the flexibilities of its basic components, each represented by an elastic stiffness coefficient k_i as stated on clause 6.3.2 [1]. Table 4.2 displays the relevant basic joint components and its respective diagrams. These are bolt in tension and end-plate bending, which are obtained from table 6.11.

4.4.2 Spring model principle

The rotational stiffness is derived from the elastic stiffness of the components and their elastic behaviour of each component is represented by a spring. The force-deformation relationship of each of the spring (i) is given by [14]:

$F_i = k_i E \Delta_i$:

Where

- F_i = the force in the spring i
- k_i = the stiffness coefficient of the component i
- E = the Young Modulus
- Δ_i = the spring deformation i

The spring components in a joint are combined into a spring model. Figure 2 shows for example the spring model for an unstiffened welded beam-to-column joint.
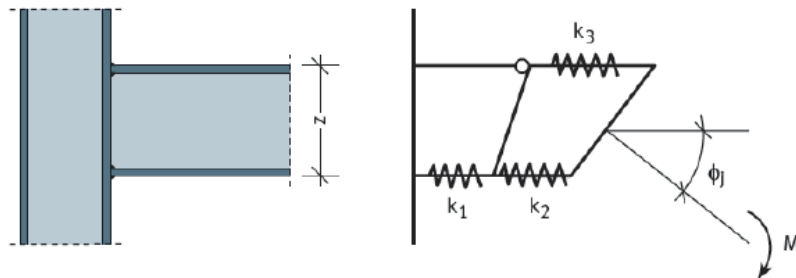
Figure 4.8: Spring model for calculations of rotational stiffness of beam column connection

Each spring components contributes their forces F and the moment acting in the spring model is equal to Fz whereby z is the lever arm. The equation for determining the rotational stiffness is shown on the expression (4.8). Furthermore, the initial rotational stiffness $S_{j,ini}$ is also given by the same expression 4.8 with the stiffness ratio μ being equal to 1.

$$S_j = \frac{M_j}{\Phi_j} = \frac{Fz}{\frac{\sum \Delta_i}{z}} = \frac{Fz^2}{\frac{F}{E}\sum \frac{1}{k_i}} = \frac{Ez^2}{\mu \sum_i \frac{1}{k_i}} \qquad (4.8)$$

4.4.3 Stiffness coefficients for basic joint components

The components in a column base that are affected by bending are the end-plate and the bolts. The end-plate is mainly subjected to bending while the bolts outside the tension flange of beam are subjected to tension caused by the bending of the column base joint.

Table shows the expressions for determining the stiffness coefficient of the basic components mentioned.
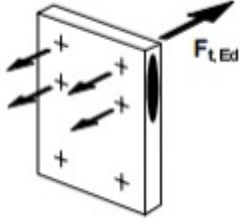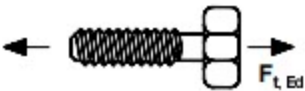
Component	Stiffness Coefficient k_i
End plate in bending (for a single bolt-row in tension)	$k_5 = \dfrac{0{,}9 l_{eff} t_p^3}{m^3}$ l_{eff} is the smallest of the effective lengths. m in this case is equal to m_x for a bolt row located in the extended part of an extended end-plate.
Bolts in tension (for a single bolt-row in tension)	$k_{10} = \dfrac{1{,}6 A_s}{L_b}$ L_b is the bolt elongation length

Table 4.2: Basic joint components

The bolt elongation L_b is equal to the grip length (total thickness of material and washers), plus half the sum of the height of the bolt head and the height of the nut (reference). The diagram including its formula is displayed on figure 4.9 and expression (4.9).
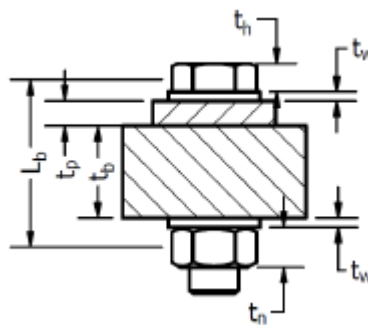
Figure 4.9: Details of the bolt

$$L_b = \frac{t_h + t_n}{2} + t_w + t_p + t_b \tag{4.9}$$

The previous students have shown how these expressions were obtained [7], and therefore these expressions are briefly presented as (4.10) and (4.11). Since the end-plate and the bolts are subjected to the same force their stiffness coefficients k_5 and k_{10} are calculated in series [15] so as to obtain the total stiffness coefficient k_{tot} of the system. This is demonstrated on the expression below:

$$\frac{1}{k_{tot}} = \frac{1}{k_5} + \frac{1}{k_{10}}$$

(4.10)

The inverse total of the stiffness is used on expression 4.10 to calculate the rotational stiffness of the entire joint, which is an assembly of the basic components. An alternative way of expressing the expression (4.10) is by including the initial rotation, which is shown on the expression (4.12):

$$k_{tot} = \frac{1}{\frac{1}{k_5} + \frac{1}{k_{10}}}$$

(4.11)

$$S_{j,ini} = k_{tot} E z^2$$

(4.12)

4.5 High strength steel (HSS)

4.5.1 Background

The development of new materials and an increased technical knowledge of materials have contributed to technological and economic growth within different industries and sectors, which in return have led to traditional construction materials such as steel to undergo rapid development [10].

Furthermore difficult industrial tasks such as oil extraction in climatically challenging areas at greater depths has also led to the demand and development of higher performance materials in constructions. Therefore higher strength steel are applicable in such cases due to having enhanced corrosion resistance, good welding properties and higher toughness at low temperatures.

The structural steel grade S355 used to be considered as high strength steel (HSS) over 30 years ago. Currently, $fy = 355 - 460 \, Mpa$ are the main constructional steel for hot rolled plates and H-sections in Europe [10].

Steels with nominal yield stress equal to or more than 460 MPa are considered as high strength steel according to Eurocode 3 [1]. On the other hand steels with nominal yield stress above 690 MPa are usually classified as very high strength steels (VHSS). The use of both high-and very strength steel in many structures all over the world has increased in the last decade because of their economic benefits in comparison to ordinary steels. Therefore, the trend towards the use of HSS and VHSS in constructions continues. [16]
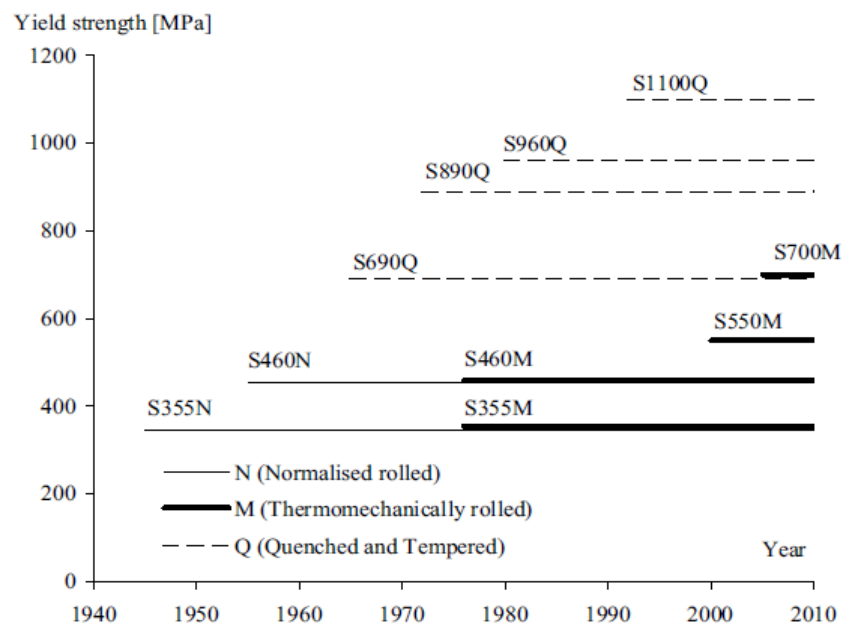
Figure 4.10: Development of high strength structural steel grades

As you can see from the figure S700 is becoming a common used steel grade.

4.5.2 Mechanical properties

The mechanical properties of high strength steel is still not as known as ordinary steel grades due to its recent usage. Therefore further investigation of mechanical properties of high strength steel is still ongoing [17]. Some important mechanical properties will be explained briefly [18]:

Stress-Strain Curves: The stress-strain curve below shows the mechanical properties of HSS and mild steels.
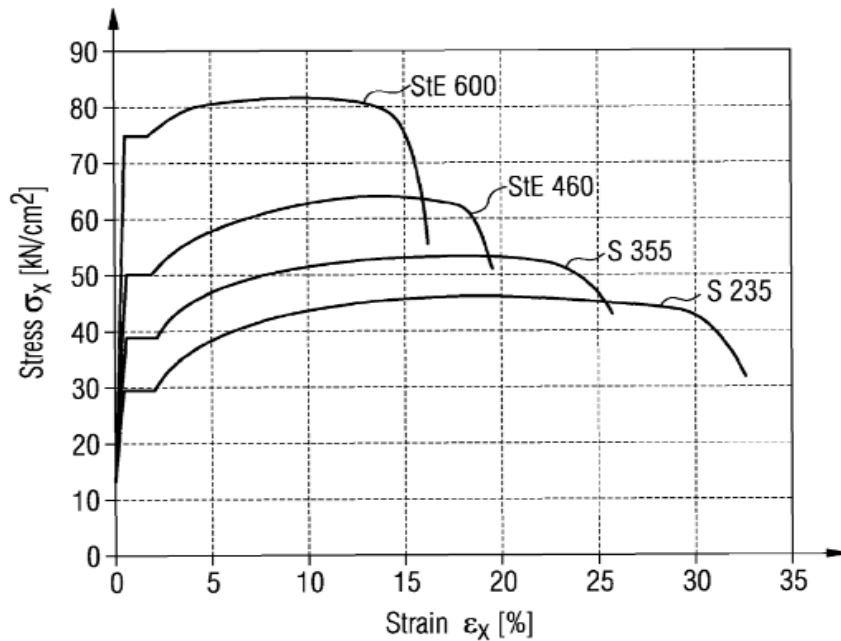
Figure 4.11: Stress strain curves of different high strength steel grades

Figure 4.11 shows that as the steel strength increases, the length of the yield plateau becomes shorter including the fracture strain. In some cases when the yield plateau is absent, the $f_{0,2}$ stress can then be used as yield stress for the HSS [10].

Ductility: The ductility of the HSS becomes poor as the steel strength increases, which further emphasised on the stress-strain curve since the yield length plateau for HSS is shorter than the mild steels.
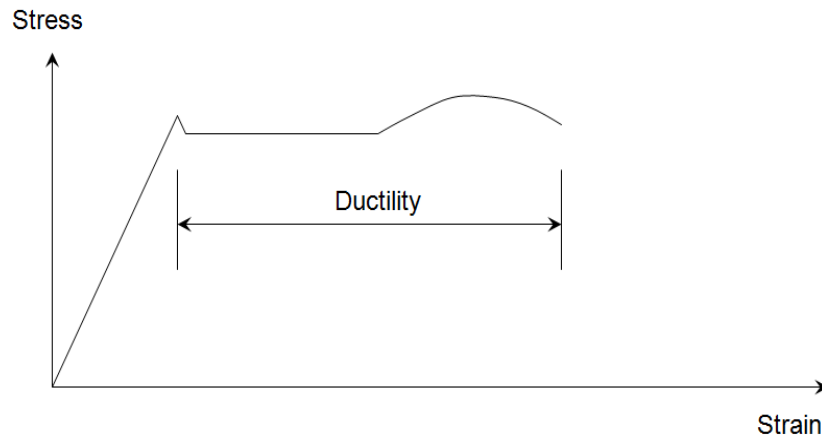
Figure 4.12: Stress-strain ductility

Toughness: The toughness of the HSS is much better than the ordinary ones, which is also helpful at lower temperatures.

Weldability: Furthermore, HSS show generally improved weldability compared to ordinary structural steels and they are suitable for all current welding methods.

4.5.3 Benefits of using HSS

The main advantages of high strength steel is that it contributes to reduced weight and dimensions. Design stresses can be increased and plate thickness may be reduced, resulting in significant weight savings. Reduced plate thickness also contributes to save on welding costs as well as on fabrication, erection and transportation costs. Simplified structural components and construction techniques are often possible, particularly for large structures, and foundation costs may also be reduced due to lower dead weight. For instance weight reduction of bridge construction can be achieved with 60% when S690 steel grades are used. The reduction of the structural means less consumption of steel in construction, which is beneficial for the environment [18].

Although the structural strength and stiffness of HSS can be relatively easily derived, this is not the same case for the evaluation of the deformation. Since HSS has large elastic strengths, however there is no corresponding increase in the Young's modulus, which is constant as the yield stress increases. This may bring some problems with serviceability limit states [19]

Currently the material costs for HSS are still higher than the mild steel grades. Nevertheless, the continuous testing and research and promotion of such material will help to establish new detailed design codes. Thus, the demand of HSS is expected to increase, which will lead to its price reduced in the future [18].

4.5.4 Codes and standards

The sets of rules and guidelines provided in NS EN 1993-1-8 as mentioned earlier are mainly applied to structural joints connections with either H or I section and also covering various steel grades from S 235 to S 460. The NS EN 1993-1-12 provides an additional rules for the extension of NS EN 1993 standards up to steel grades S700 [20].

The additional rules provided for NS EN 1993-1-8 by NS EN 1993-1-12 is only applicable for high strength steel grades in elastic global analysis and not plastic global analysis [20].

The reason is that high strength steel are less ductile compared to the mild steels and a joint with this kind of steel is likely to act as plastic hinges during deformation [15]. Therefore, this is not compatible with elastic global analysis.

	NS-EN 1993-1-1	NS-EN 1993-1-12
f_u/f_y	$\geq 1,10$	$\geq 1,05$
Elongation at failure	$\geq 15\ \%$	$\geq 10\ \%$
Ultimate strain (ε_u)	$\varepsilon_u \geq 15\ f_y/E$	$\varepsilon_u \geq 15\ f_y/E$

Table 4.3: Ductility requirements for mild steels and high strength steels

The table shows the ductility requirements for the highs strength steel are lower in NS EN 1993-1-12 compared to NS EN 1993-1-1 [21]. There have been recent breakthrough in steel making technologies that have produced high strength steel with enhanced tensile mechanical properties, especially in terms of deformability and ductility and the need for plastic global analysis restriction have not yet been discussed [15].

4.5.5 Examples of HSS application

Currently, high strength steels are mostly used in mechanical engineering, ship engineering, offshore engineering and civil engineering. High strength steels were also used in some significant structures and landmark constructions and these are some of the examples [22]:

Figure 4.13: New York freedom tower
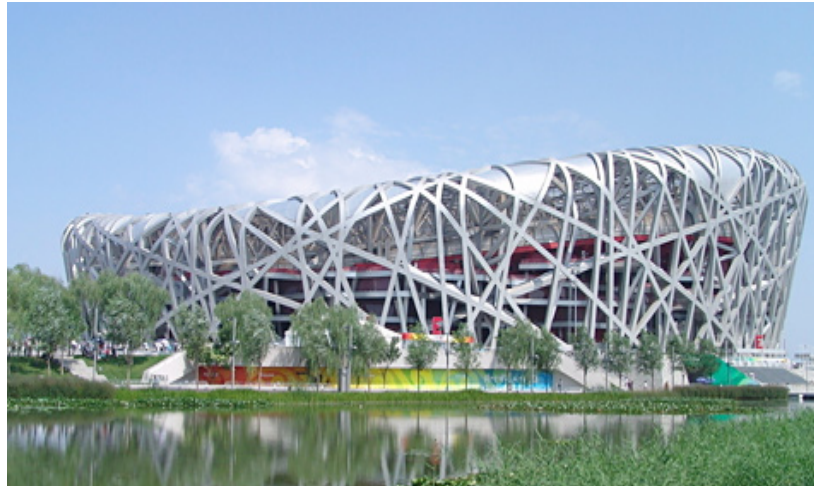
Figure 4.14: The Beijing Bird's Nest Olympic Stadium

Furthermore several bridges have been constructed with the use of high strength steel in Japan since 1960. Most of these bridges constructed have 500-600 MPa yield strength and 800 MPa has also been used in several bridge projects [18]. These are some of the existing bridges in Japan.

Figure 4.15: Tokyo Gate Bridge.

Figure 4.16: The Akashi Kaikyo Bridge

The automotive industry also takes the advantages of using very high strength steels with yield strengths of up to 1350 MPa (Xiao-Ling Zhao) and they have greater strength to weight ratios compared to mild steel and high strength steel. VHSS is mostly used as a cost effective solution for enhancing particularly vehicle safety. Despite the benefits of using VHSS as a structural material, it is still limited due to lack of research supporting its use and relevant design guidelines [23].

The table below shows the general application of different steel grades.

Yield strength	Type	Typical Examples	Potential Application
<460	Mild Steel	S235-S420	Buildings
460-600	Conventional High strength steel (CHSS)	S460 S550	Bridges, High rise buildings
690-1100	Very high Strength Steel (VHSS)	S690 S890 S960 S1100	Cranes, Bridges, Offshore structures

Table 4.4: Typical examples and application of various structural steel types

5 Laboratory experiment

5.1 General

The laboratory experiment is part of the investigation model, which were conducted on the end-plate connections of high strength steel. Both elastic and plastic experimental procedures were executed and their main purpose was obtaining the stiffness and the capacity of the end plate connections with different geometries respectively. The results obtained from this model are thus compared to the Abaqus and hand calculations.

The experimental procedures conducted in this investigation follows Uhre's test program conducted, which he conducted on his thesis [7] including Bringsvor and Kirkerud [9].Therefore this investigation also serves as an extension of end plate connections investigation with higher steel grade.

The equipment used to perform this investigations are listed below and demonstrated on figure 5.1. The weight of 5 kg shown on figure 5.1 was not used in the experiment, it serves only as an illustration:

- Weights (10, 20, 50 kg)
- Clinometer
- Tape measure
- Digital Vernier calliper
- Feeler gauge
- Weld gauge

Figure 5.1: Equipment used *[8]*

The rotation and deflection of the column during bending was recorded by a clinometer and a tape measure. The clinometers were placed on both sides of the hollow profile at the column base point so as to record its rotation about an axis when subjected to load. The data recorded during the experiments are registered on the computer where the clinometers are connected to. The feeler gauge was used to measure the gap between the end plate's surface and the stiff wall. Figure 5.2 demonstrates the functions of the equipment used.

Figure 5.2: Functions of the equipment

5.2 Test specimens

The behaviour of an extended end plate connections of high strength steel subjected to the bending moment is investigated on two specimens, which are modelled as column-bases .As mentioned prior this investigation is an extension study. Therefore the geometries are not significantly altered. The specimens are presented in the following chapters with a brief background about them. The thickness of the end plates for both specimens are 6 mm, the reason for this particular value is presented in the appendix D.

The cross section drawings of the specimens are presented in the following chapters are theoretical. Accurate measurements of these specimens were taken so as to document the uncertainties. The measurement were conducted on the actual test specimens in the laboratory before the experiments were carried out. These drawings are presented in the appendix A.

The table below shows the dimensions of the subcomponents for both test specimens which presented in the following chapters.

Table 5.1: Dimensions of the subcomponents

Column's cross sectional dimension	Welds throat thickness	Bolts diameter and class
RHS 80x80x4 mm	4 mm	M16, 8.8

5.2.1 Specimen A

The notion of specimen A was introduced by Ina Birkeland [6] whereby she investigated the significance of a pinned limit boundary of column base on Abaqus since the Eurocode disregards it. The column base initially consisted of an H-profile that was welded to a base plate and both these elements were anchored vertically to a 500 x 500 mm concrete slab. The anchor bolts were fastened on both side of the profile's web.

This investigation was proceeded by Uhre and the initial profile of specimen A depicted by Birkeland was altered to a hollow profile as shown on figure 5 so as to fit his research. The thickness of Uhre's end plate was 8 mm and this was reduced to 6 mm by Bringsvor on his research, which is also mentioned on chapter 2.
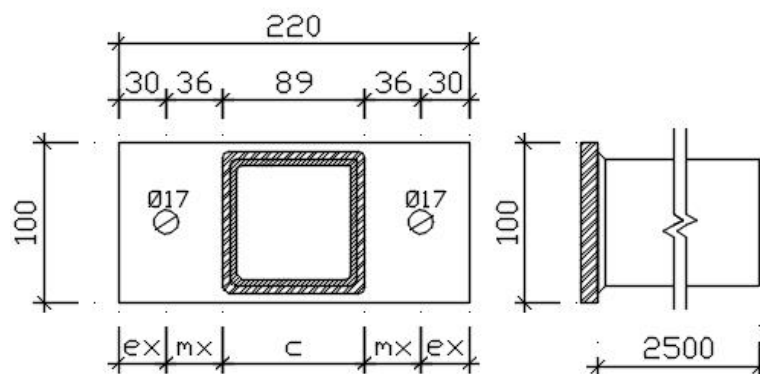
Figure 5.3: Specimen A

5.2.2 Specimen B

Specimen B has an identical geometry to Kirkerud's (reference) column base. The only difference is that the end-plate's steel grade is consisted of Weldox 700 instead of S355, this is also the same case for specimen A. Specimen B as demonstrated on figure 5.2, which contains 4 bolts. The 2 bolts are fastened to the rigid wall on both sides of the extended end plate. The capacity and the stiffness of Specimen B is also obtained from two configurations that is bending about the major and minor axis.
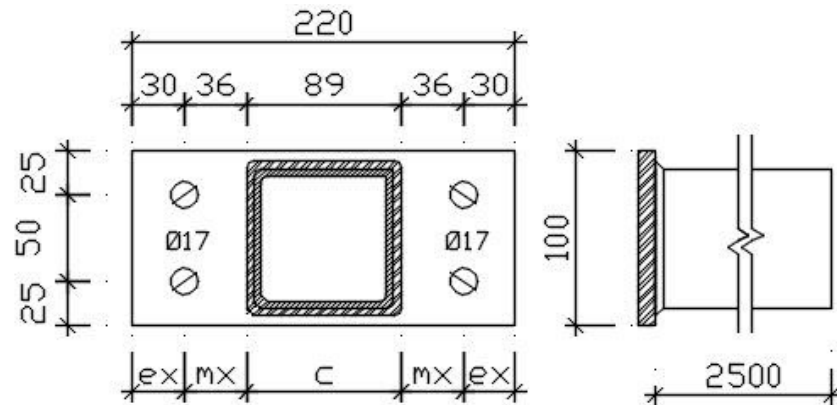
Figure 5.4:Specimen B

5.2.3 Definition of the strong and weak axis bending

Both specimens are subjected to loading about its weak-and strong axis as demonstrated on figure 5.4:
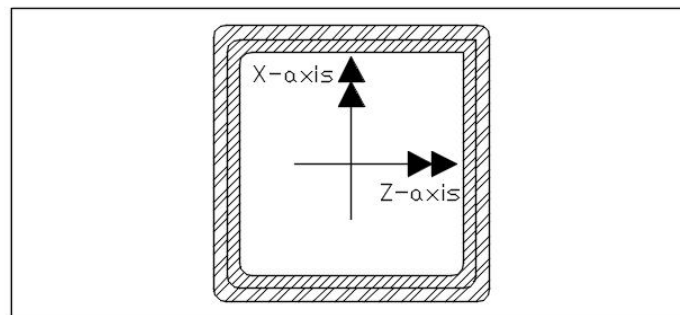
Figure 5.5: Test specimens

5.3   Equipment setup

The column base was anchored horizontally as a cantilever beam, which was fastened to a 30 mm thick steel plate with M16 bolts, which is also fastened to a 50 mm thick wall. The 30 mm steel plate is assumed to be taken as an infinitely rigid plate in hand calculations including the Abaqus model in which Uhre crosschecked in his experiment [7]. The bolts in the connections for both specimens are fastened with a tightening torque at 80 Nm.
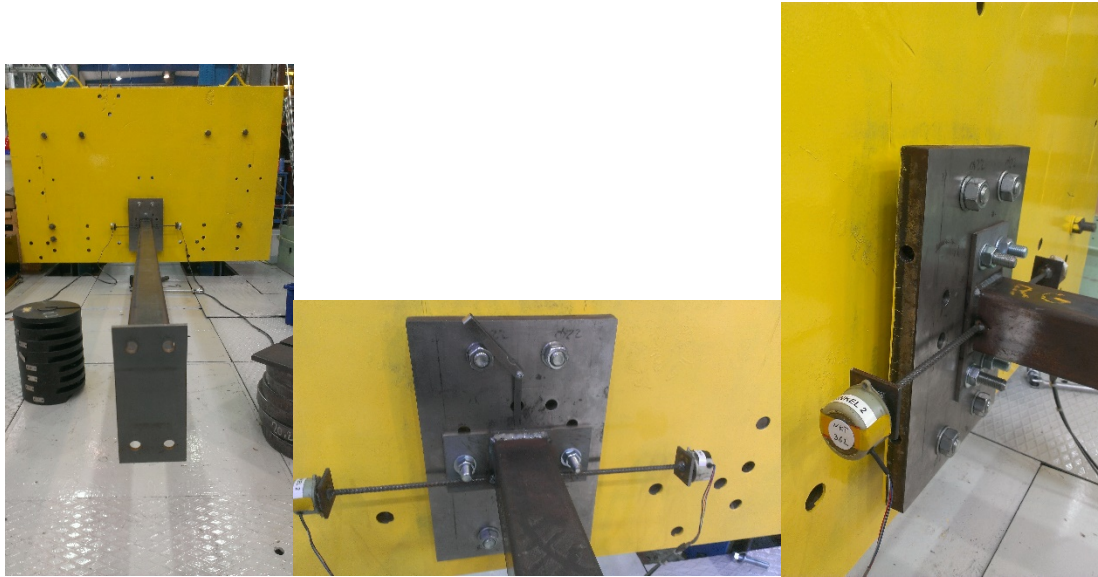
Figure 5.6: Equipment setup

The clinometers are placed on both sides of the hollow profile as shown on figure 5.4. The steel rods that hold the clinometers are welded to the hollow profile. The data recorded are registered in the computer where by the rotational change in the column base are displaced on the screen against time as a graph. The two rotational values from each clinometers are also displayed on the computer when the column base is subjected to a specific load. Both of these values contribute to less uncertainty when averaged so as to obtain a specific value at a specific load.

5.3.1 Objects used and loading point

Two hollow columns with specimen A and B were welded to each side of the column as displayed on figure 5.5. They were marked as AA and RG, which is known as object 1 and 2. The specimen on object 1 were loaded about the weak axis and the same for object 2, about the strong axis. The detail drawings of the connections for AA and RG are shown on the appendix A.

Their lengths are 2.54 m and 2.75 m, which is from the outer end plate tip to the other and this corresponds to its respective moment arms as displayed on table 5.3. Longer moment arm were preferred in relation to their actual length, this avoids heavier weights at shorter moment arm.
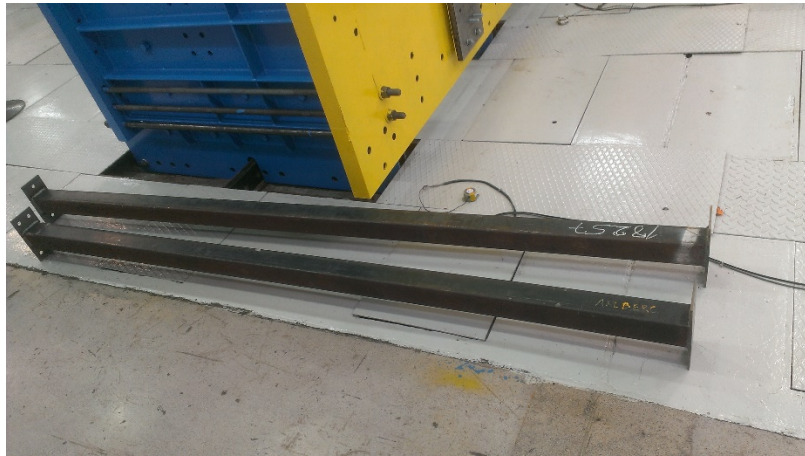
Figure 5.7: Test objects

Test objects	Actual Length (m)	Moment arm (m)
Object 1 (weak axis)/ AA	2,54	2,35
Object 2 (strong axis)/RG	2,75	2,50

Table 5.2: Test objects

The column as mentioned is mounted as a cantilever beam and the moment arm is measured and marked. The weights were placed at its centre on a marked particular point and a flat steel plate of 10 kg was also used especially for heavier weights so as to create stability when the pile of weights got higher. The steel plate has a hole at its centre, which makes it easier to place the weight at its centre on the column.
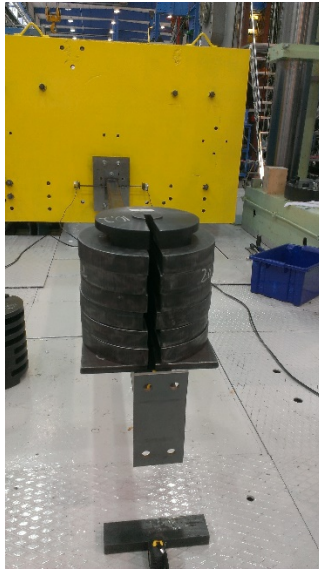
Figure 5.8: Figure of flat steel plate and weight

The deflection of the column was recorded by a tape measure, which was placed at the bending tip of the column as demonstrated on the figure 5.7. The tape measure is a placed under a steel block, which serves as a reference point when measuring deflection for all experimental series.

Figure 5.9: Tape measure at the tip of the column

5.4 Procedure (elastic and plastic procedures)

Two kinds of experimental procedures were conducted in this investigation, which are the plastic and elastic procedures. The elastic experiments were conducted in order to determine the initial stiffness of both end plate specimens. This was conducted by loading and unloading weights on the column base in sequence at low load levels as shown in chapter 6 including the appendix F. An estimate of how much the column base could withstand the weights whilst being in the elastic region was considered, which is also based on the previous students assumptions [7] [9] .

Finally, the capacity of the end plate is determined by loading both specimens with increasing weights until the end plate is permanently deformed. This procedure is known as the plastic procedure. Figure 5.8 shows permanent deformation of specimen B when bent about the strong axis.

Figure 5.10: Plastic procedure at a weight of 360 kg

The weights were applied in increments of 10 kg in the elastic procedure and the maximum weight used in each series would increase by increments of 20 kg as demonstrated in the tables in the chapter 6. Although this is not the case for specimen A, which is subjected to moment about weak axis as shown in chapter 6.2.1, whereby 8 series in total were conducted as shown on table.

In total 4 experimental attempts were conducted when loading the specimens about its weak and strong axis for the elastic and plastic procedures. 1 attempt is generally equivalent to 6 series whereby the first 5 series were conducted with elastic analysis and the last one is full plastic analysis. This is demonstrated on the table 5.3.

Specimens / End plate thickness (mm)	Bending axis	Number of elastic series	Number of plastic series
Specimen A 6,3	Weak axis	7	1
	Strong axis	5	1
Specimen B 6,3	Weak axis	5	1
	Strong axis	5	1

5.4.1 Data collection

The raw data of the deflections were registered manually on the excel sheet during the experiment and the data from the clinometer were retrieved automatically on the computer, which were saved on the spreadsheet beforehand.

The feeler gauge as mentioned was used to measure the gap between the end plate's surface and the stiff wall. The gap on the edge of the plate was also measure so as to observe the curvature of the end plate, which tends to curve after being welded to a hollow profile [8].

The gap measurements are measured initially before the first series are initiated and after the last series is conducted. The gap is also measured when the end plate is permanently deformed. They are also measured at the same reference point, which is on the middle and on the edge of the end plate.

Figure 5.11: Feeler gauge measurement on the gap

The gap between the end plate and the rigid plate were measured at 0.10-0.20 mm, which is less than gap Bringsvor usually measured at 0.50-1.0mm [8]. Based on this observation, The Weldox 700 end plate has less curvature compared to the mild steel therefore less gap.

5.4.2 Uncertainties

During the experiment, the clinometer would record larger rotation at lower load levels. Uncertainties. This was solved by calibration on the excel sheet, whereby the initial recorded value was deducted from each row.

38

6 Results from the laboratory

6.1 General

This chapter represents the results obtained from conducting elastic and plastic experiments for both specimens in the laboratory. For the elastic experimental results, the number of loading and unloading sequence for each series are represented in the table including the elastic linear graph. This is also the same case for the plastic results where by the results are represented in the curves including the maximum weight for each series. This is applied to the specimens when bent about each respective axis.

6.2 Elastic procedure

In the elastic global analysis, the initial stiffness is determined by conducting multiple elastic series of loading-unloading weight on the steel joint with an increasing maximum weight for each series. These series are demonstrated on the appendix F.

All the $M - \varphi$ graphs for each series are collected on a single graph as an average in order to determine the final initial stiffness of the joint bending about the respective axis as shown on this chapter. The initial stiffness is the average initial loading, which usually lies in the range 10-30 kg.

6.2.1 Specimen A: Bending about the weak axis

In this scenario, six elastic series were conducted where by the maximum weight of each series are displayed on the table 6.1. Figure 6.1 displays the average graph of the collective series in terms of moments and its rotation. The curve is perfectly elastic, which shows the loading and the unloading process. The initial stiffness of specimen A when bent about the weak axis $S_{jini,z,A}$ is shown on the expression (6.1) and demonstrated on figure 6.1:

$$S_{jini,z,A} = 191,2 \; kNm/rad \tag{6.1}$$
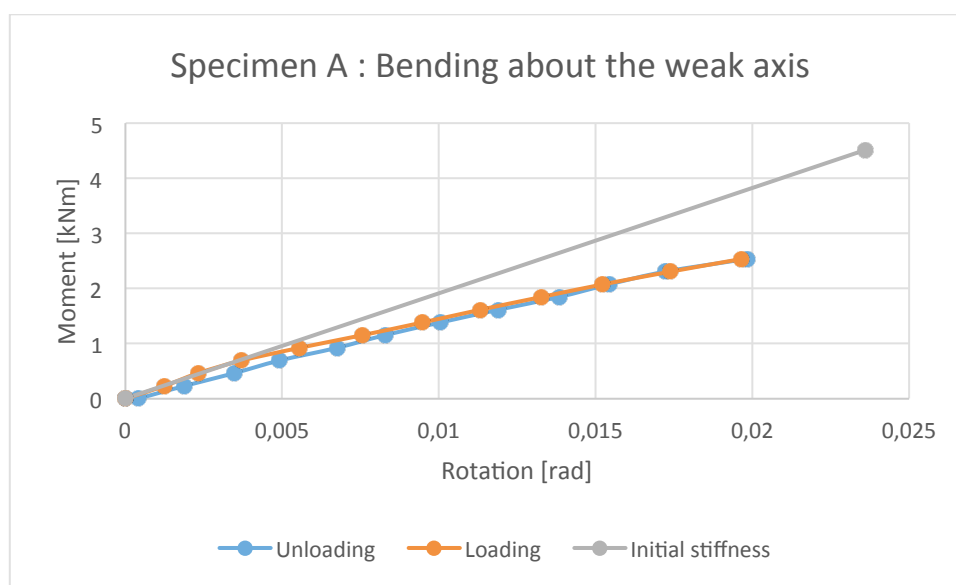
Figure 6.1: Stiffness curve for specimen A, weak axis

The initial stiffness 191.2 kNm/rad was obtained by averaging the stiffness of the initial loading in the range of 10-30 kg on the connection. This loading range corresponds to the moment range of 0.23-0.69 kNm, i.e. the three initial values on the loading sequence that are approximately less than 1kNm as shown on figure 6.1. The initial stiffness curve is then obtained by dividing the moment to where the curve stops, which in this case is 4.5 kNm.

$$Rotation\ [rad] = \frac{M[kNm]}{S_{jini,z,A}[kNm/rad]} = \frac{4,5}{191,2} = 0,024\ rad \qquad (6.2)$$

Then the initial curve is graphed from the origo to the last point at (0.024, 4.5). This method of calculating the initial stiffness in the elastic region was obtained from Uhre' work [7] and it is same applied to the initial stiffness in the following chapters.

Table 6.1 shows the maximum weight of each series with their corresponding increase in moment.

Series	1	1	2	3	4	5	6
Weight [kg]	50	60	70	80	90	100	110
Moment [kNm]	1,15	1,38	1,61	1,84	2,07	2,31	2,53

Table 6.1: The maximum weight for each series

6.2.2 Specimen A: Bending about the strong axis

In this scenario, five elastic series were conducted where by the maximum weight of each series are displayed on the table 6.2. Figure 6.2 displays the graph of the collective series in terms of moments and its rotation. The curve is perfectly elastic, which shows the loading and the unloading process. The initial stiffness of specimen A when bent about the strong axis $S_{jini,y,A}$ is shown on the expression (6.3) and demonstrated on figure 6.2:

$$S_{jini,y,A} = 463{,}7 \ kNm/rad \tag{6.3}$$
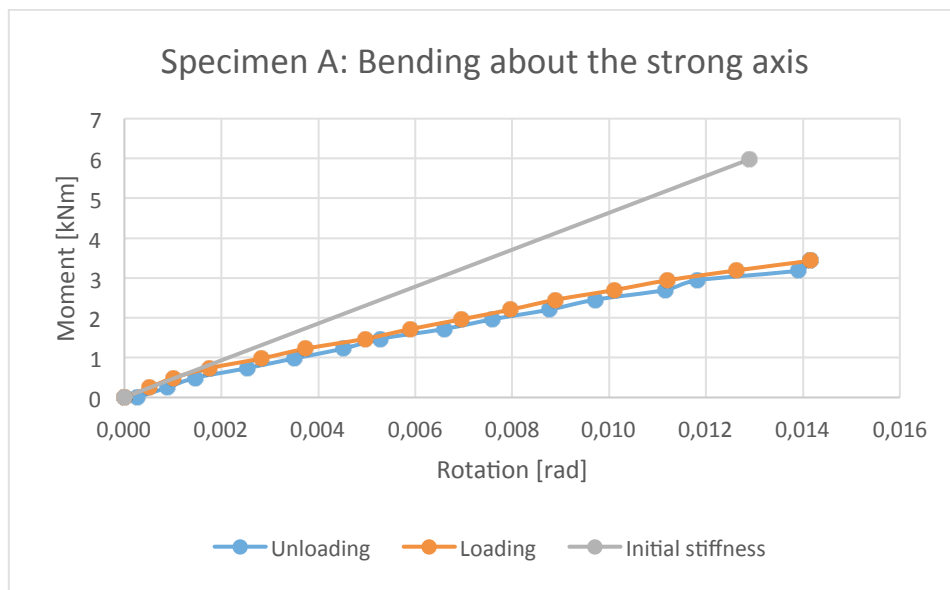
Figure 6.2: Stiffness curve for specimen B, strong axis

The maximum weight in each series increases with an interval of 20 kg in order to observe to what extent the joint is still in the elastic region due to the end plate having a much higher capacity. The outcome of this is fewer series were performed as displayed on the table below.

Series	1	2	3	4	5
Weight [kg]	60	80	100	120	140
Moment [kNm]	1,47	1,96	2,45	2,94	3,43

Table 6.2: The maximum weight for each series

6.2.3 Specimen B: Bending about the weak axis

In this scenario, five elastic series were conducted where by the maximum weight of each series are displayed on the table 6.3. Figure 6.3 displays the graph of the collective series in terms of moments and its rotation. The curve is also perfectly elastic, which shows the loading and the unloading process. The unloading curve is shifted to the right in relation to the loading curve due to the average of its data giving slightly different numbers compared to the loading curve. The initial stiffness of specimen B when bent about the weak axis $S_{jini,z,B}$ is shown on the expression (6.4) and demonstrated on figure 6.3:

$$S_{jini,z,B} = 429,63 \; kNm/rad \qquad (6.4)$$
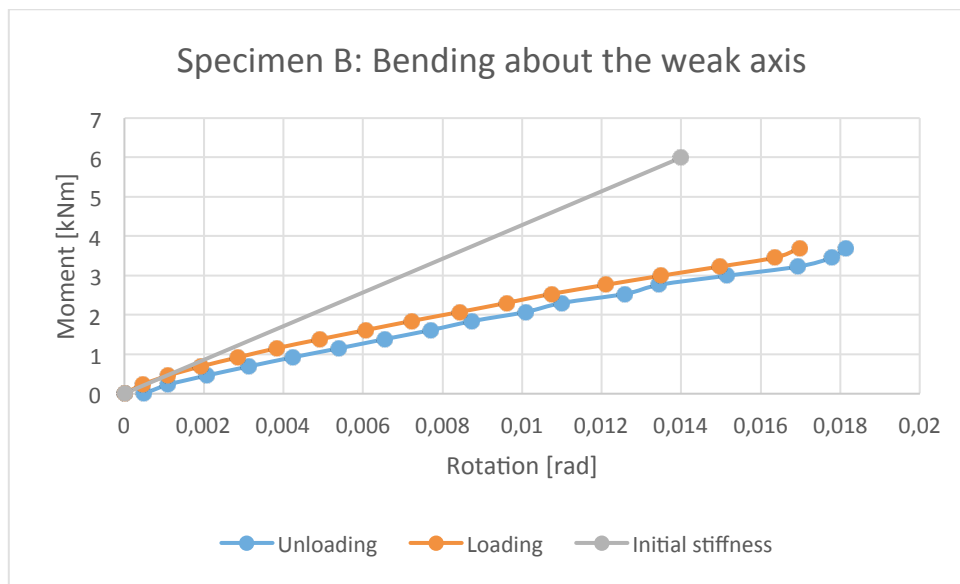
Figure 6.3: Stiffness curve for specimen B, weak axis

The maximum weight in each series also increases with an interval of 20 kg as the previous case. The only difference in this case is that the maximum weights of each series has increased at weight of 20 kg. The basis of this intuitive decision is that Kirkerud had 70 kg as his initial maximum weight in his investigation for specimen B while in this case its 80 kg due to the higher capacity of HSS. This is applied to specimen B in general.

Series	1	2	3	4	5
Weight [kg]	80	100	120	140	160
Moment [kNm]	1,84	2,31	2,77	3,23	3,69

Table 6.3: The maximum weight for each series

6.2.4 Specimen B: Bending about the strong axis

In this scenario, five elastic series were conducted where by the maximum weight of each series are displayed on the table 6.4. Figure 6.4 displays the graph of the collective series in terms of moments and its rotation. The curve is also perfectly elastic, which shows the loading and the unloading process. The initial stiffness of specimen B when bent about the strong axis $S_{jini,y,A}$ is shown on the expression (6.5) and demonstrated on figure 6.4:

$$S_{jini,z,B} = 593,8 \ kNm/rad \tag{6.5}$$
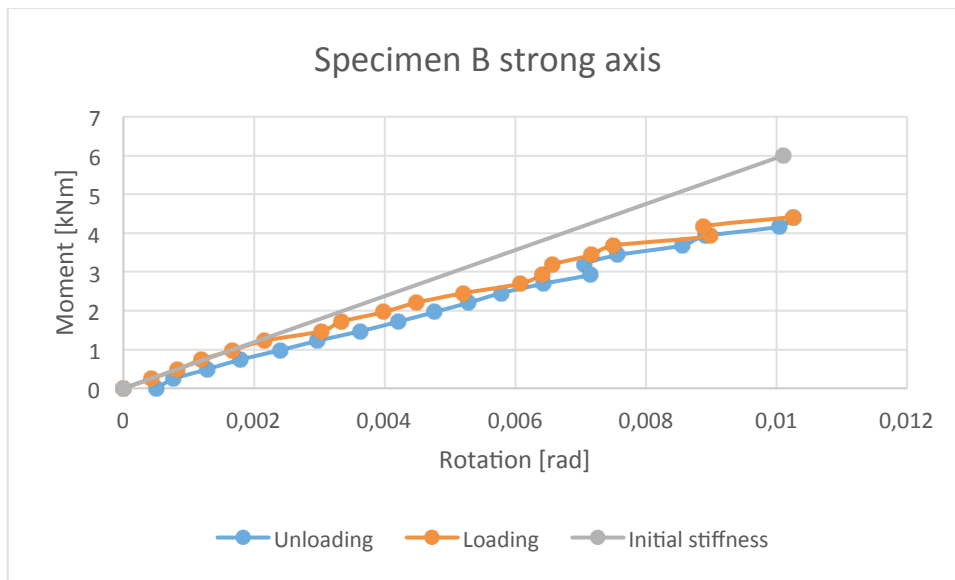
Figure 6.4: Stiffness curve for specimen B, strong axis

The table below shows the maximum weight of each series with their corresponding increase in moment.

Series	1	2	3	4	5
Weight [kg]	80	100	120	140	160
Moment [kNm]	1,96	2,45	2,94	3,43	3,92

Table 6.4: The maximum weight for each series

6.3 Column base classification

In this chapter, the end plate connections are classified by its stiffness when considered as a column base. The classification boundary for the rigid joints are obtained from the Eurocode as depicted on the expression (6.6). The area moment is obtained from the formula book [24] and the length of the column is equivalent to the moment arm, which is 2500 mm long.

$$S_{jini} \geq \frac{30EI_C}{L_C} = \frac{30 \cdot 210000 \cdot 1.16 \cdot 10^6}{2500} = 2923,2 \; kNm/rad \qquad (6.6)$$

The pinned limit classification for the column base does not exist on the Eurocode. Therefore Birkeland [6] deduced the pinned classification for the column base, which is in this case is a joint connection with welded RHS. The expression deduced is:

$$S_{jini} \geq \frac{0,5EI_C}{L_C} = \frac{0,5 \cdot 210000 \cdot 1.16 \cdot 10^6}{2500} = 48,7 \; kNm/rad \qquad (6.7)$$

Figure 6.5 shows that the initial stiffness obtained from chapter 6.2 lies between the rigid and the pinned boundary. These connections does not meet the requirement of the rigid limit or the pinned limit as depicted on figure 6.5.Therefore, all the specimens are classified as semi-rigid.

Specimen A, weak axis is the only connection that is closer to the pinned limit, although its stiffness 191.2 kNm/rad is far greater than the limit's value of 48.7 kNm/ rad.
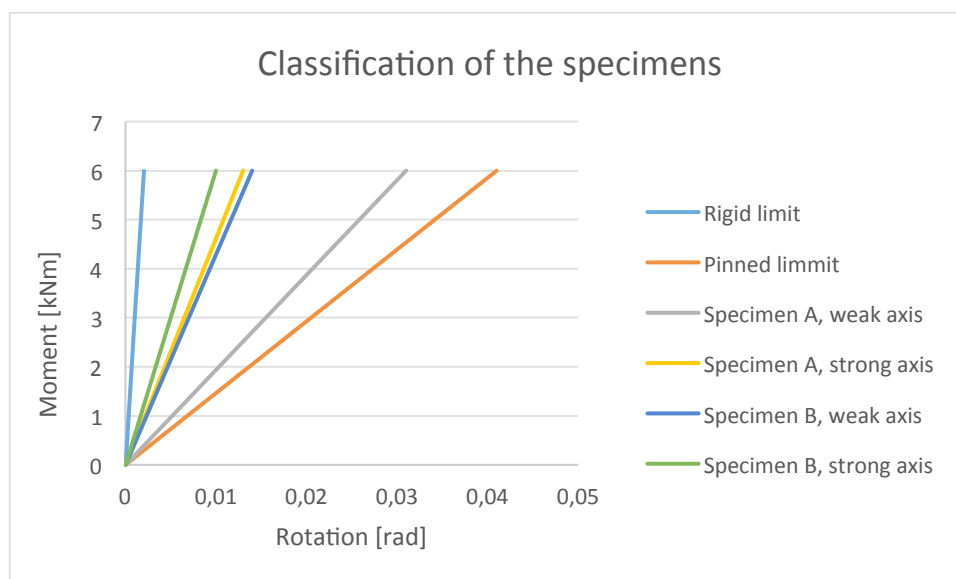
Figure 6.5: The classified specimens

6.3.1 Discussion

The $M - \varphi$ graphs of each specimen displayed in chapter 6.2 initially start as a straight line and as the curve progresses it becomes less linear at the top as demonstrated on figure 6.4. This is due to an increase of weight for each series and therefore the curve at the top will somewhat vary from the initial point. Furthermore, the average values of each loading interval becomes as one approaches top of the curve, which Kirkerud also observed [9]. Otherwise, the initial stiffness for each cases presented in chapter 6.2 are accurate.

6.4 Plastic procedure

This chapter represents the results obtained from the plastic experiment conducted in the laboratory for each specimens, when bent about both axis. According to the Eurocode, the rotational stiffness S_j of a semi-rigid joint with its corresponding bending moment $M_{J,Ed}$ should generally be used in the elastic global analysis if $M_{J,Ed}$ does not exceed 2/3 $M_{j,Rd}$ [1]. The initial stiffness is no longer of use in this case, since $M_{J,Ed}$ does exceed the upper elastic limit.

The following simplification of the rotational stiffness for all values of the moment $M_{j,Ed}$ as shown on figure 3.3 in chapter 3.2.1:

$$S_j = S_{j,ini}/\eta \ \text{ if } \ \frac{2}{3}M_{j,Rd} \leq M_{j,Ed} \leq M_{j,Rd} \tag{6.8}$$

This rotational stiffness S_j also known as the secant stiffness is used in this case as an indication for evaluating when the plastic region starts, which theoretically lies in the lower interval as shown on expression 6.6. Furthermore the capacity of the joint as a column base is evaluated in term of its strength by determining the ultimate moment ($M_{j,u}$) that is when the joint is permanently deformed. The graphs in the following chapters show the initial stiffness curves demonstrated in chapter 6.2 including the secant stiffness curve which is specifically $\frac{2}{3}M_{j,Rd}$ from the origo.

6.4.1 Specimen A: Bending about the weak axis

Specimen A deformed permanently at the weight of 230 kg which is equivalent to the maximum moment capacity $M_{j,u,z,B}$ bending about the weak axis depicted on expression (6.9).

$$M_{j,u,z,B} = 5{,}30 \ kNm \tag{6.9}$$

The stiffness curve intersects at the point on the response curve which is beyond knee point, which is the point where the elastic region makes a transitions to the plastic region. The initial stiffness depicted on figure 6.6 is the same value as the expression (6.1). The secant stiffness of the response curve is shown below:

$$S_{J,z,B} = 109{,}8 \ kNm/rad \tag{6.10}$$

Figure 6.6: Plastic region, Specimen A-Z axis

	$S_{jini,z,B}$ $\left[\dfrac{kNm}{rad}\right]$	$S_{J,z,B}$ $\left[\dfrac{kNm}{rad}\right]$	$S_{J,z,B} = S_{j,ini}/\eta$ $\left[\dfrac{kNm}{rad}\right]$
Specimen A, Z-axis	191,2	109,8	63,7

Table 6.5: The corresponding rotational stiffness

6.4.2 Specimen A: Bending about the strong axis

In this investigation the moment capacity is obtained from the lowest range of the expression (6.8) shown above. In this case the maximum moment plastic capacity $M_{j,u,y,B}$ of specimen A when bent about the strong axis reaches when the column base deforms at 290 kg, which is equivalent to the expression (6.9).

$$M_{j,u,y,B} = 7{,}11 \; kNm \tag{6.11}$$

The stiffness curve intersects at the point on the response curve which is also beyond knee point, which is the point where the elastic region makes a transitions to the plastic region. The initial stiffness depicted on figure 6.7 is the same value as the expression (6.3). The secant stiffness of the response curve is shown (6.6) including table.

$$S_{J,z,B} = 192{,}8 \; kNm/rad \tag{6.12}$$

Figure 6.7: Plastic region, Specimen A- Y axis

	$S_{jini,y,B}$ $\left[\dfrac{kNm}{rad}\right]$	$S_{J,yB}$ $\left[\dfrac{kNm}{rad}\right]$	$S_{J,z,B} = S_{j,ini}/\eta$ $\left[\dfrac{kNm}{rad}\right]$
Specimen A, Y-axis	463,7	192,8	154,6

Table 6.6: The corresponding rotational stiffness

6.4.3 Specimen B: Bending about the weak axis

In this case the maximum moment plastic capacity reaches when the connection deforms also at 290 kg as specimen A did about the strong axis. The 290 kg is equivalent to the expression (6.13)

$$M_{j,Rd,yz,B} = 6,7 \ kNm \qquad (6.13)$$

The stiffness curve intersects at the point on the response curve which is also beyond knee point. The initial stiffness depicted on figure 6.8 is the same value as the expression (6.4). The secant stiffness value of the response curve shown on (6.14) is included on the figure 6.8.

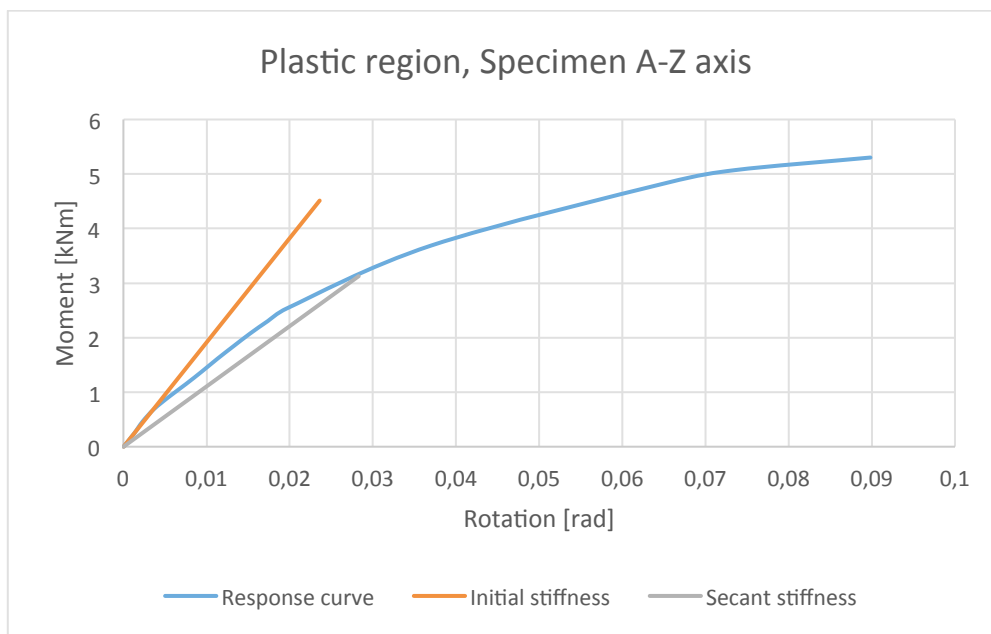$$S_{J,z,B} = 198,7 \ kNm/rad \qquad (6.14)$$

Figure 6.8: Plastic region, Specimen B-Z axis

	$S_{jini,z,B}$ $\left[\dfrac{kNm}{rad}\right]$	$S_{J,z,B}$ $\left[\dfrac{kNm}{rad}\right]$	$S_{J,z,B} = S_{j,ini}/\eta$ $\left[\dfrac{kNm}{rad}\right]$
Specimen B, Y-axis	429,6	198,7	143,2

Table 6.7: The corresponding rotational stiffness

6.4.4 Specimen B: Bending about the strong axis

In this case the maximum moment plastic capacity $M_{j,u,y,B}$ reaches when the column base deforms also at 360 kg. This specimen has the highest capacity and 360 kg is equivalent to the expression (6.15).

$$M_{j,u,y,B} = 8,8 \ kNm \tag{6.15}$$

The intersection between the stiffness curve and the response curve is much further away from the knee point. The stiffness of the response curve is shown (6.16) including table 6.8. The initial stiffness depicted on figure 6.8 is the same value as the expression (6.5). The secant stiffness of the response curve is shown as (6.5) including table 6.8.

$$S_{J,z,B} = 192,8 \ kNm/rad \tag{6.16}$$
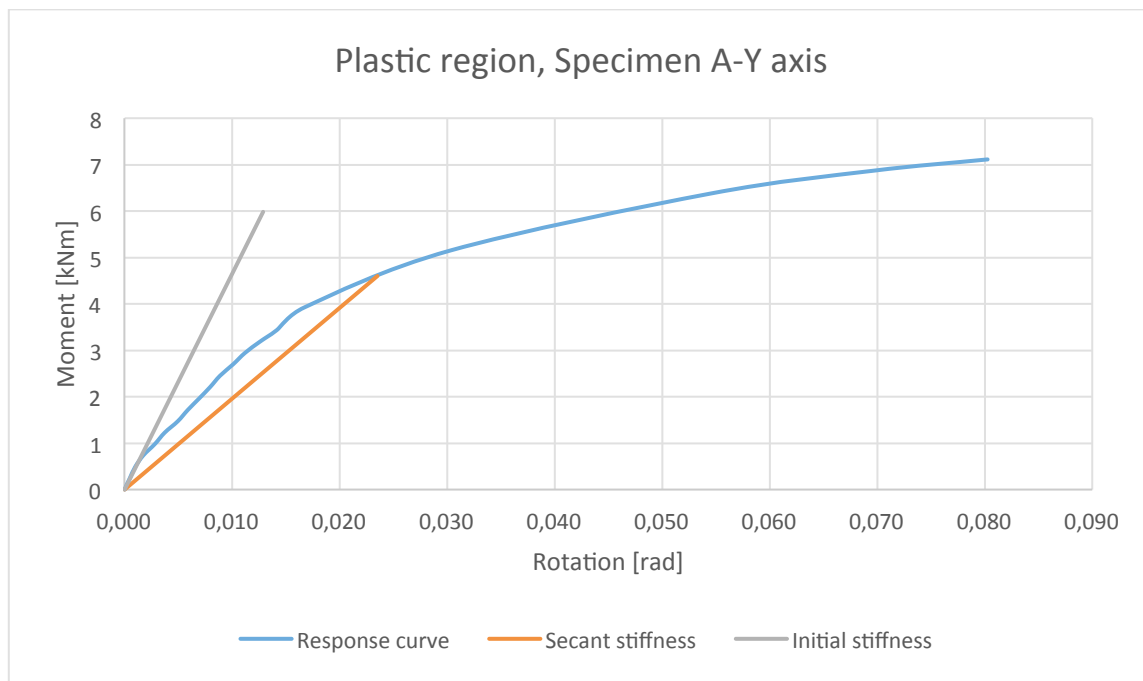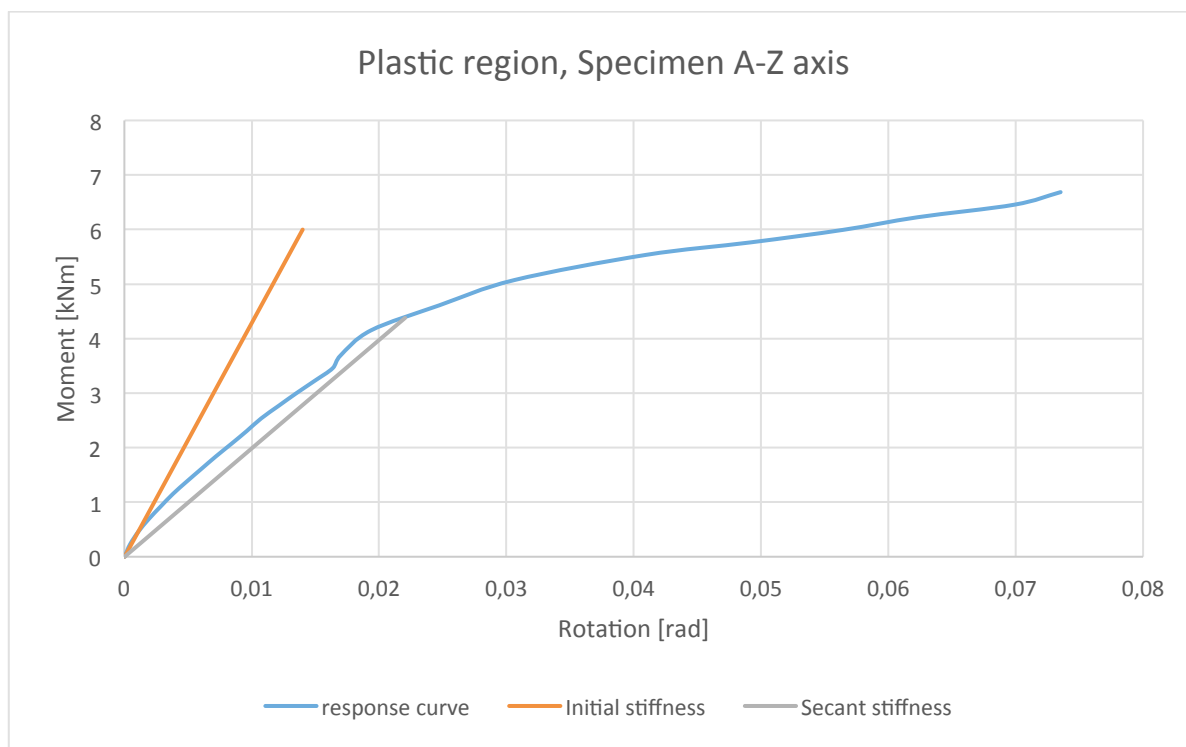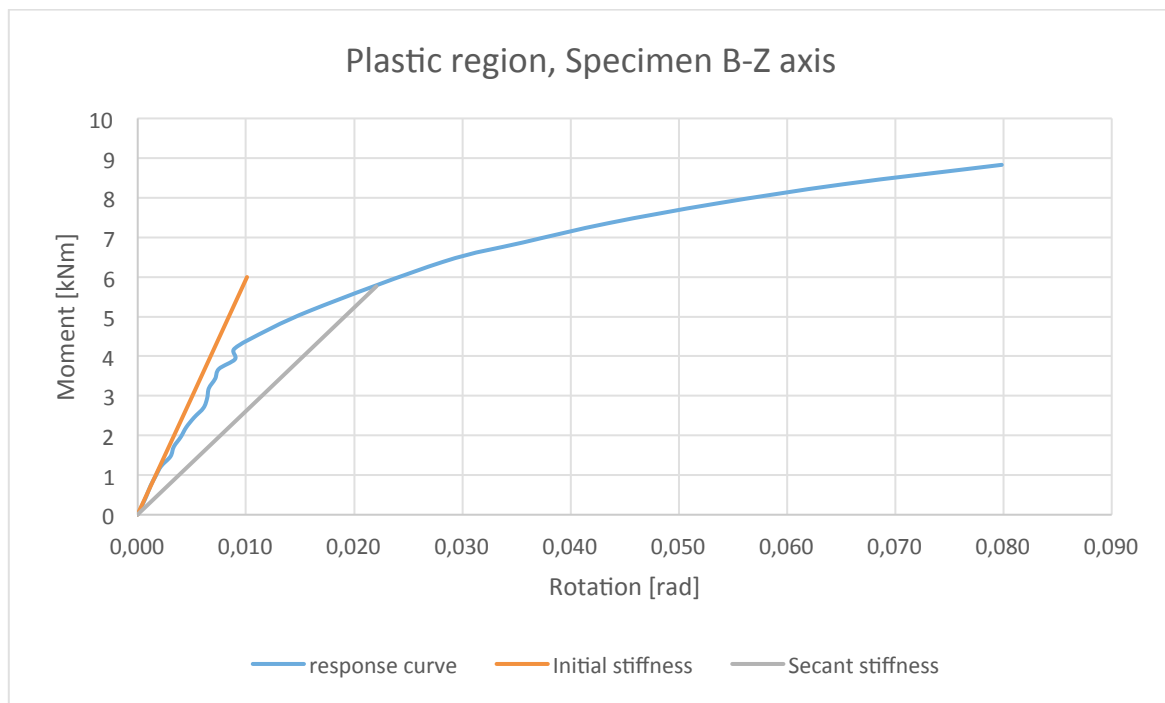

Figure 6.9: Plastic region, Specimen B-Y axis

	$S_{jini,y,B}$ $\left[\dfrac{kNm}{rad}\right]$	$S_{J,yB}$ $\left[\dfrac{kNm}{rad}\right]$	$S_{J,z,B} = S_{j,ini}/\eta$ $\left[\dfrac{kNm}{rad}\right]$
Specimen B, Y-axis	593,8	261,4	197,9

Table 6.8: The corresponding rotational stiffness

6.4.5 Discussion

The secant stiffness in most figures presented in chapter 6.4 intercepts the response curve at the point beyond the knee point, which is a point when the elastic region transitions to the plastic region. As Kirkerud pinpointed that it's hard to exactly locate the point at which the plastic region starts, which in theory is located on the plateau part of the curve [9]. For instance the secant stiffness curve demonstrated figure on 6.8 intersects substantially beyond the knee point.

Uhre proposed the design stiffness for the non-linear curve, which are the graphs demonstrated on chapter 6.4 by creating a straight line fitted to the response curve such that it intersects the moment corresponding to the initiation of permanent rotation [25]. In other words, the interception between the response curve and at point when moment starts to yield, which is known as in this report as secant stiffness modified. Uhre's method is followed to obtain the solution to the problem in chapter 6.4.4 as shown on figure 6.10 and 6.11.

Figure 6.10 demonstrates the initial stiffness which is 593.8 kNm/rad, which is obtained from chapter 6.2.4, i.e. expression (6.5) and the secant stiffness modified is 436.6 kNm/rad. The secant stiffness modified was obtained by using the same procedure of calculating the initial stiffness procedure as demonstrated on chapter 6.2.1.

Finding the point where the moment starts to yield can be challenging but the transitions from the elastic to the plastic regions assumes to start at the knee point where the moment is 4 kNm. This is judged by observing 6.10 and figure 6.11, which shows the specimens B's final capacity about the strong axis in the plastic region.
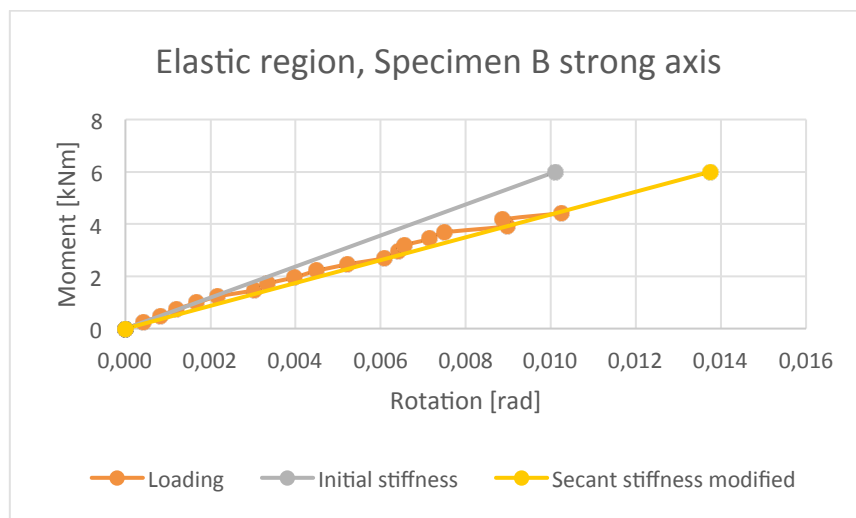
Figure 6.10: Specimen B strong axis bending in the elastic region.
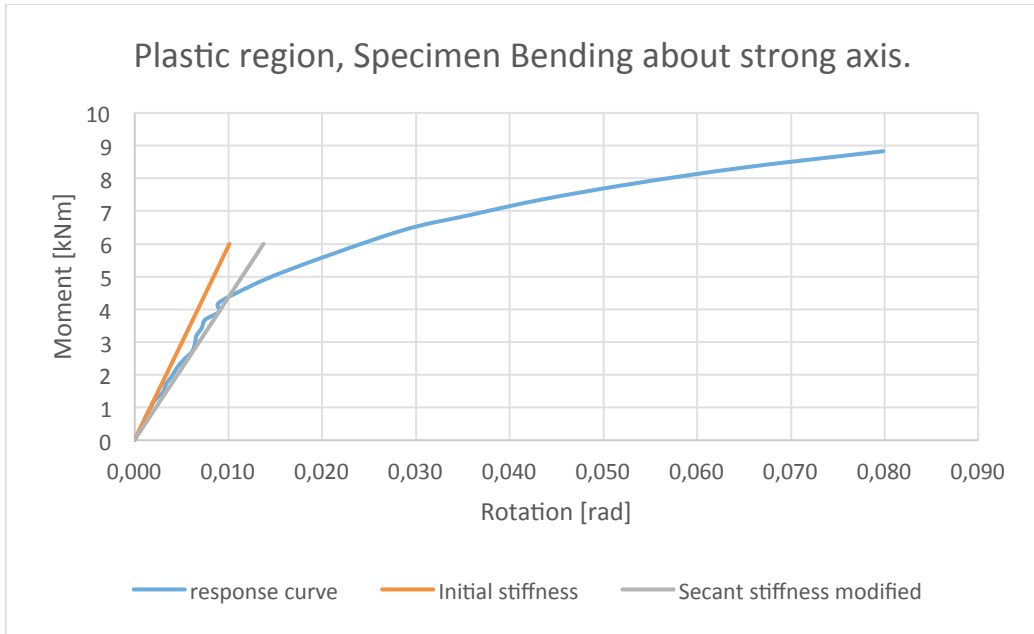
Figure 6.11: Plastic region, Specimen B bending about strong axis.

6.4.5.1   Dead load

Generally the unloaded cantilever beam is initially affected by its dead load due to the weight of the members. Therefore the connection is somewhat slightly bent before it's loaded as shown on figure 6.12. Figure 6.14 shows the cantilever beam subjected to the point load and dead load, which is the representation of the situation on figure 6.12 and 6.13 that shows the connection bolted to the rigid wall as a cantilever beam.

Figure 6.15 shows the moment diagram of the cantilever beam subjected to the point load only and the expression (6.17) used to obtain the moment caused by the point load M_p. Figure 6.16 shows the moment diagram of the cantilever beam subjected to the dead load only and the expression (6.18) used to obtain the moment caused by the point load M_g. L_o is the moment arm at 2.35 m long and L is the length of the beam at 2.54 m for both specimens when bent about the weak axis and 2.50 m and 2.75 m long for both specimen when bent about the strong axis as shown on table 5.2.

$$M_p = P_{max}L_o \tag{6.17}$$

$$M_g = \frac{1}{2}gL^2 \tag{6.18}$$

However, it's been observed that the dead load affects the ultimate moment capacity for the plastic experiment for all bending cases of the specimens by 3-5% as shown on table 6.9. Therefore it is safe to neglect the dead weight.
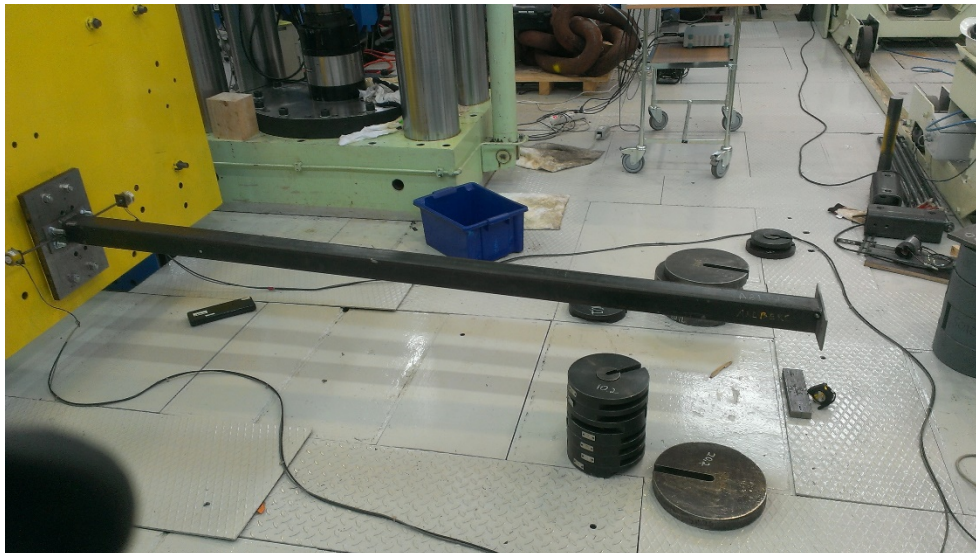
Figure 6.12: Cantilever beam before loading process
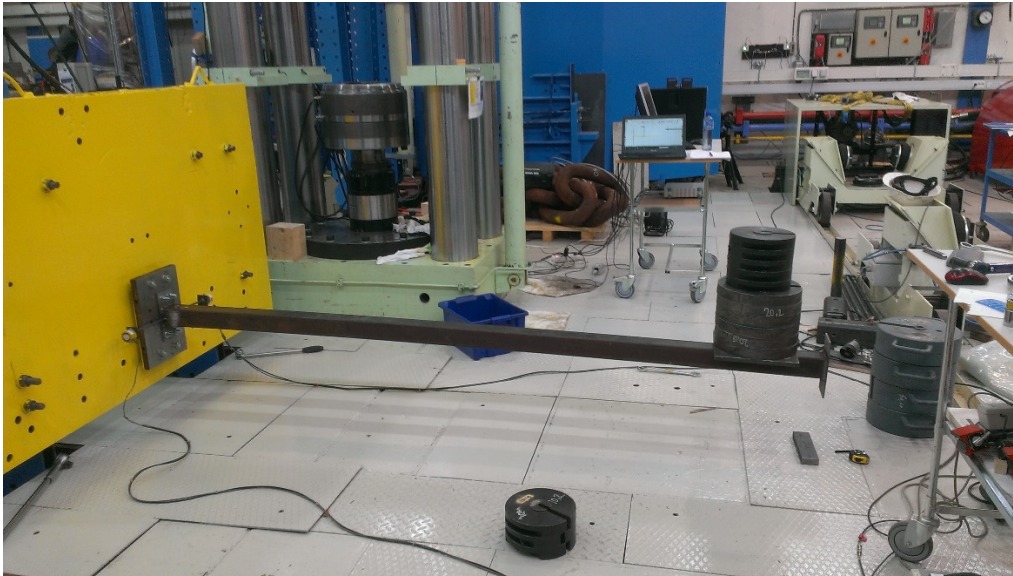
Figure 6.13: The actual connection, bolted to the rigid wall as a cantilever beam.
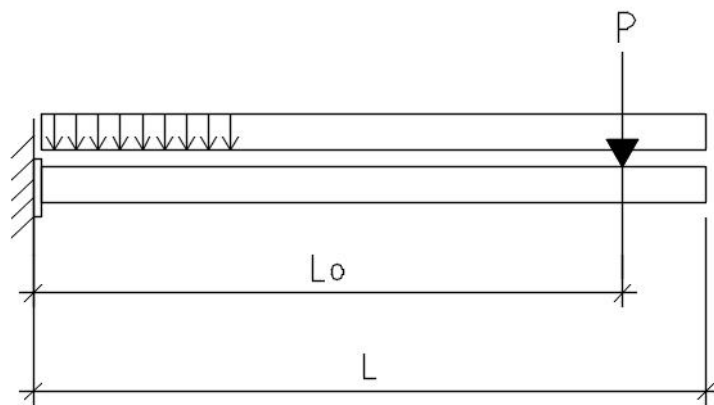
Figure 6.14: The cantilever beam subjected to point load and dead load
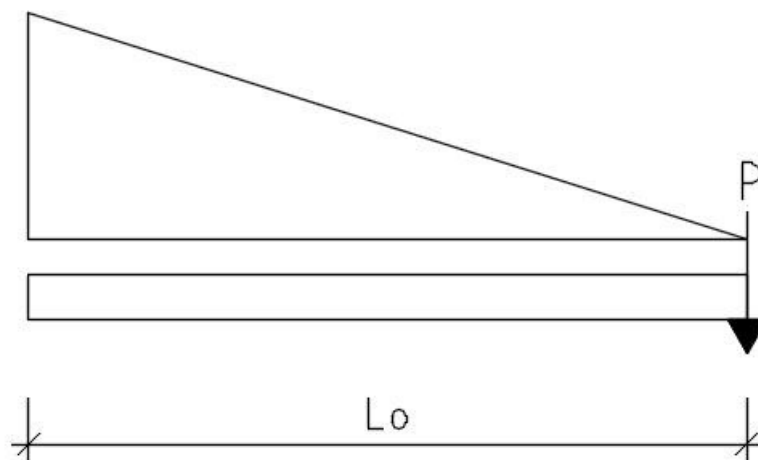
Figure 6.15: Moment diagram of a cantilever beam subjected to point load
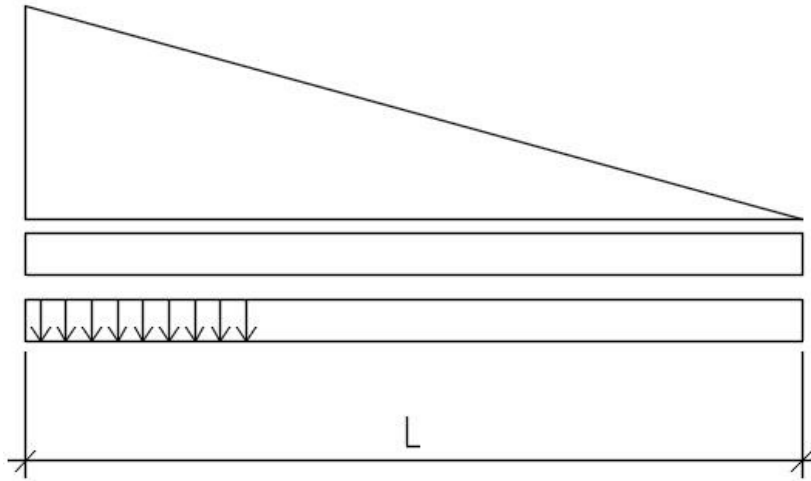
Figure 6.16: Moment diagram of a cantilever beam subjected to dead load

Specimens type, bending axis	M_p [kNm]	M_g [kNm]	M_g/M_p [%]
Specimen A, weak axis	5,3	0,3	5,6
Specimen A, strong axis	7,1	0,3	4,2
Specimen B, weak axis	6,7	0,3	4,5
Specimen B, strong axis	8,8	0,3	3,4

Table 6.9: The results of the moment effects

6.5 Tensile properties of the end plate

6.5.1 General

The tensile testing of Weldox 700 was conducted in the laboratory to obtain its material properties, with the use of two material samples, which were obtained from the longitudinal and transverse direction of a large Weldox steel plate. The standard geometry of the samples is shown on figure 6.9

The force- displacement curve were obtained as the results from the tensile testing in which the engineering strain and stress can also be calculated from. Furthermore, these values can be converted to true strain and true stress with the following formulas… assuming constant volume, which are then entered in Abaqus as the plastic material properties of the Weldox 700 end plate. The use of true strain and true stress takes into account the cross sectional area change when the specimens are subjected to varying stress.

Engineering stress:

$$\sigma = \frac{F}{A_O}$$

(6.19)

Engineering strain:

$$\varepsilon = \frac{L - L_O}{L_O}$$

(6.20)

True stress:

$$\sigma_{true} = \sigma(1 + \varepsilon)$$

(6.21)

True strain:

$$\varepsilon_{true} = \ln(1 + \varepsilon)$$

(6.22)

True plastic strain:

$$\varepsilon_{true}^{pl} = \varepsilon_{true} - \frac{\sigma_{true}}{E}$$

(6.23)
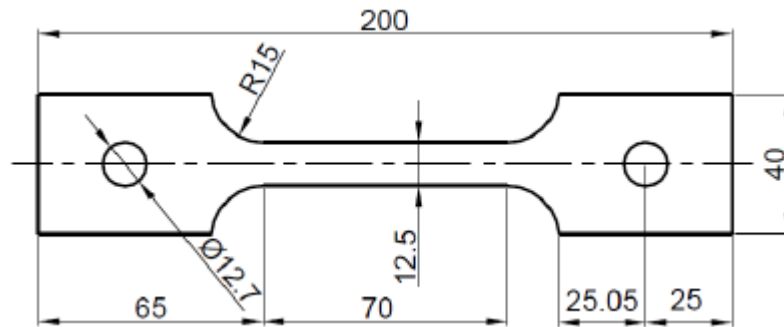
Figure 6.17: Tensile specimens
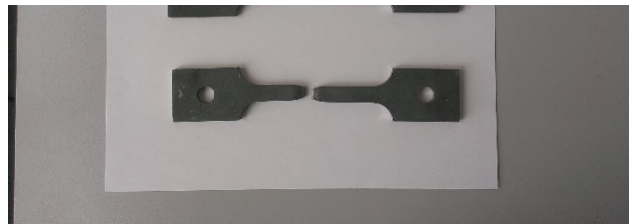
Figure 6.18: Deformed tensile specimens

Table 6.10 contains the exact measurements of the specimens before the testing started.

Material specimens	Thickness [mm]	Width [mm]
W700-A	12,50	6,09
W700-B	12,51	6,16

Table 6.10: Dimensions of tensile specimens

The material specimens were subjected to tension on the machine at a rate of 2.1 mm/min until failure. The extensometer were initially placed on the gauges section of the specimen which has the length of 35 mm in order to register the small elongation with the corresponding force applied. The extensometer were removed from the specimens as the tension reached 62 kN and 63 kN for W700-A and W700-B, respectively. The reason of the removal is to prevent the extensometer from being damaged as the specimens were approaching failure. Figure (6.18) shows the specimens after failure.

The raw data obtained from these tests were used to calculate the strains in the gauge length section for both material specimens by linear interpolation. This is done by assuming that the deformation is equally distributed along the distance between the shoulders, which is at the length of 70 mm as shown on figure (6.18).

Figure (6.19) and (6.20) shows the force displacement for both specimens. The displacement was obtained from the extensometer along the gauge length of 35 mm. The maximum force experienced by W700-A is 62 kN at a displacement of approximately 5 mm while W700-B experienced the maximum force of 63 kN at displacement of 5.3 mm.
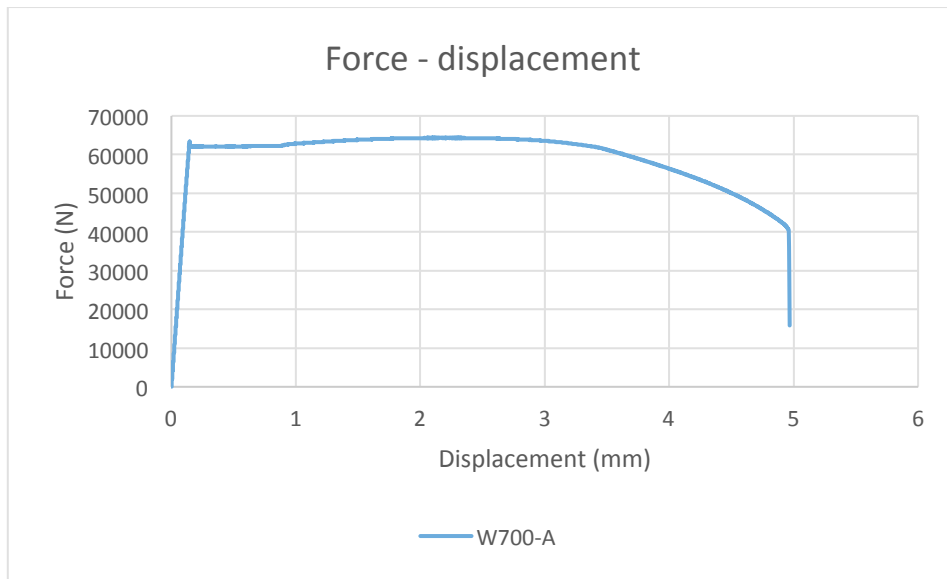
Figure 6.19: Force displacement curve of W700-A
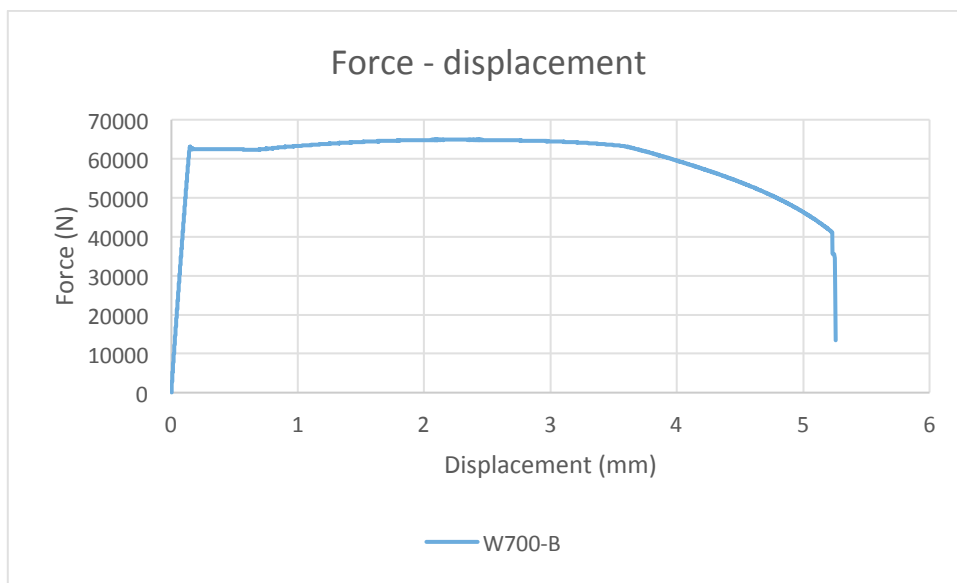
Figure 6.20: Force displacement curve of W700-B

The true engineering stress curve in W700-A in figure (6.21) and (6.22) is equivalent to the maximum engineering stress which is equal to 905 MPa and 909 MPa for W700-B. The average of these two values are 907 MPa.
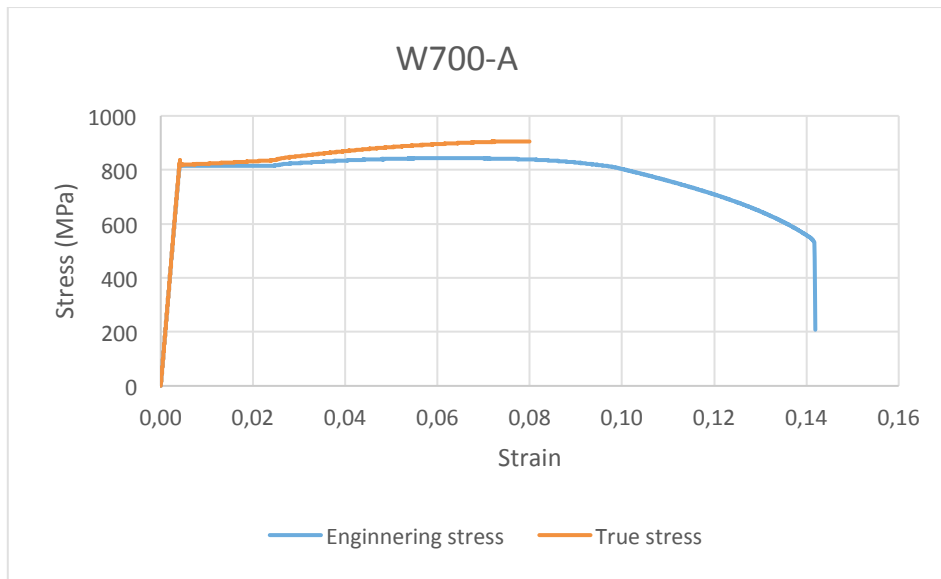
Figure 6.21: Engineering curve and True curve for W700-A
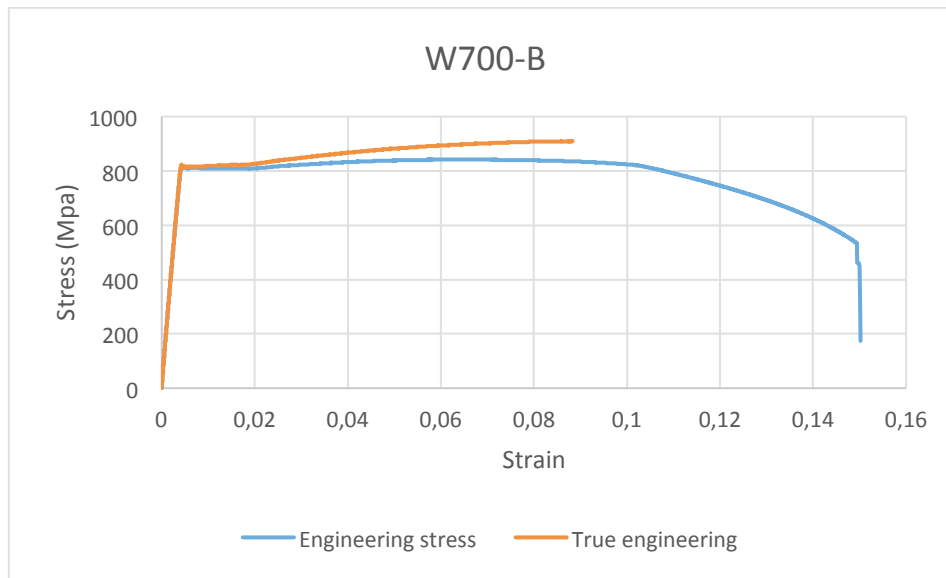
Figure 6.22: Engineering curve and True curve for W700-B

Table 6.11 shows the results obtained from the graphs shown at figure 6.21 and 6.22. Both specimens of W700 satisfies the ductility requirement of ultimate strain and fracture strain shown on table 4.3. Yet, the yield stress/ ultimate tensile stress (f_y/f_u) ratio is not satisfied. The fracture strain at 5.65 is equivalent to 17.6 %, which exceeds the fracture limit set by NS EN 1993-1-1 [21] and NS EN 1993-1-12 [20]. This indicates that the W 700 is reasonable ductile. Both specimen stretches/elongate at 6% at the maximum engineering stress, which is greater than $15f_y/E$.

	$f_y[MPa]$	$f_u[MPa]$	Fracture strain $\delta_{5.65}$ [%]
W700-A	819	843	17.6
W700-B	821	841	17.6

Table 6.11: Results obtained from the tensile test for the specimens

7 Analytical calculations

7.1 General

This chapter represents the analytical approach through hand calculations for the stiffness and the capacities of the end plate connections, which were performed by following the rules stated by the NS EN 1993-1-8 [1] Furthermore, the calculation models that are based on derived virtual work expressions developed by Uhre [25] are also represented in this chapter. This models are also applied to the specimen B so as to observe the alternative yield mechanism. The steps taken to determine the relevant stiffness coefficients are shown on appendix E.

The results obtained from hand calculations are further compared to the results that were obtained from the laboratory and numerical analysis.

7.2 Capacity

Uhre developed a calculation model for obtaining the moment capacity of the end plate subjected to plastic moment capacity. This model is based on the principle of yield mechanisms whereby if the failure mechanism of an end plate is known, the plastic moment M_p can directly be determined [12].

The expression Uhre arrived by equating the external plastic work to the internal are shown in the appendix B.2 and the result is depicted on the expression (7.1) and (7.3) in the following chapters. The measured stiffness and capacity are calculated from the actual thickness of the end plate for both specimens, which is 6.3 mm.

7.2.1 Capacity for bending in the weak axis

7.2.1.1 Specimen A

The deformation of specimen A about the weak axis forms yield patterns that were observed by Uhre [7], which is depicted on figure 7.1. The yield lines A and B are assumed to be symmetrical on both sides of RHS. This is a physically possible mechanism and was shown by Uhre to give accurate results.
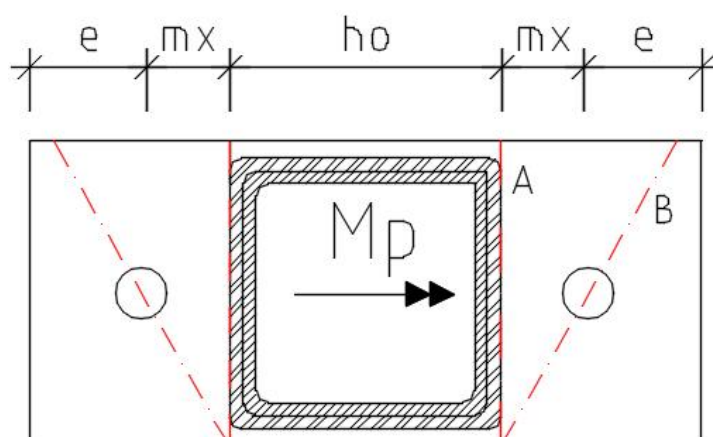
Figure 7.1: Specimen A, weak axis

The bolts are assumed to not deform, although yield line B passes through it. The expression (7.1) is used to calculate the moment capacity M_p of the connection in this case.

$$M_p = \frac{2m_p}{m}\left(b_p^2 + 2m^2\right) \tag{7.1}$$

The expression (7.2) assures that the bolts in this specimen do not deform. The bolts are assumed to have sufficient tensile strength, which is equal to 1.3 times the force obtained directly from the external loading. This is supposed to less or equal to the tension resistance of the bolts as depicted on expression (7.2), which is also applied to Specimen B bending about the weak axis.

$$F_{t,Rd} = \frac{k_2 f_{ub} A_S}{\gamma_{M2}} \geq F_{t,Ed} = 1{,}3\frac{M_p}{b_p} \tag{7.2}$$

	$M_p [kNm]$	Point load $[kg]$
Specimen A_Z-axis	4,41	180
Specimen A_Z-axis- (measured)	5,69	250

Table 7.1: Results of moment plastic capacity

7.2.1.2 Specimen B

3 possible yield mechanisms were considered for specimen B, bending about the weak axis in which the upper bolts are in tension while the lower bolts aren't. The expressions for calculating the plastic moment capacities were obtained by following Uhre's procedure which is based on the principle of virtual work as shown on the following chapters.

7.2.1.2.1 Yield mechanism 1

This mechanism is identical to the case in Specimen A when bent about the weak axis therefore the moment capacity expression is still the same, which is:

$$M_p = \frac{2m_p}{m_x}\left[b_p^2 + 2m_x^2\right] \tag{7.3}$$

The diagram of the yield mechanism is depicted below, which is also identical to the figure 7.1. The yield patterns in this case is likely to happen based on Kirkerud's deformed specimens from his investigation [9].
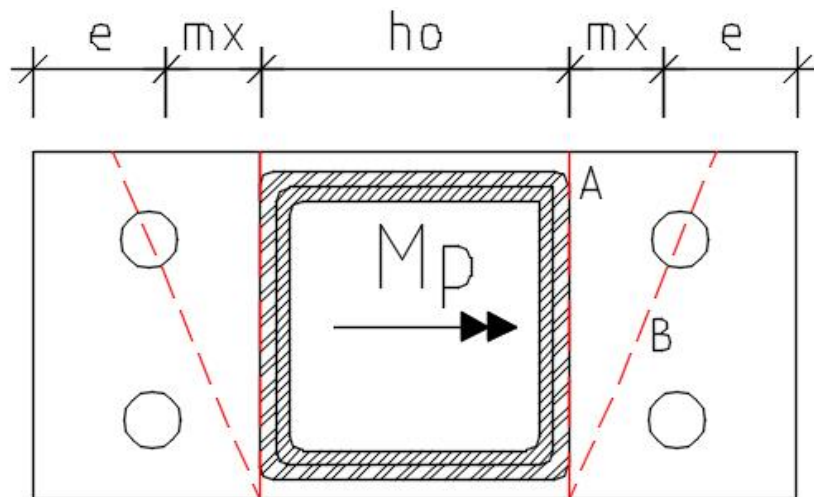
Figure 7.2: Yield mechanism 1, Specimen B weak axis

7.2.1.2.2 Yield mechanism 2

The yield mechanism is altered slightly, there are two **A** and **B** yield lines, which are located at both sides of the end plates as shown on figure 7.3. A new yield line is added, which is along length **C** under the RHS. The moment capacity expression is depicted on the expression (7.4). Appendix.B.2,shows the steps taken to obtain this expression:

$$M_p = M_p \left[c + \frac{2b^2}{L_2} + \frac{2Lb}{r} \right] \tag{7.4}$$
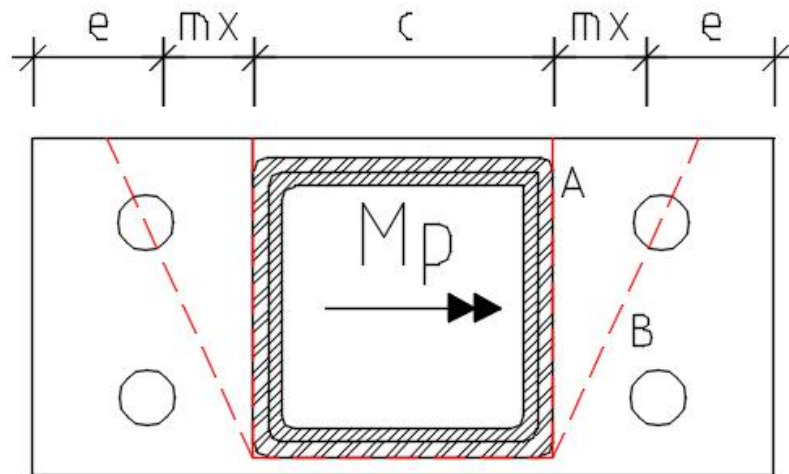
Figure 7.3: Yield mechanism 2, Specimen B weak axis

7.2.1.2.3 Yield mechanism 3

This mechanism is identical to yield mechanism 1.The slight difference is that yield line located at **e**, which is vertical instead of slanted. The moment capacity expression for this mechanism is depicted below:

$$M_p = 2m_p b_p \left[\frac{e}{m} + \frac{b_p}{L_2} + \frac{L}{r} + \frac{m}{e} + \frac{e}{m} \right] \tag{7.5}$$

The diagram of the third yield mechanism is depicted below whereby yield line **A**, **L**, **e** and **r** are apparent on both sides of the hollow profile on the extended end plate.
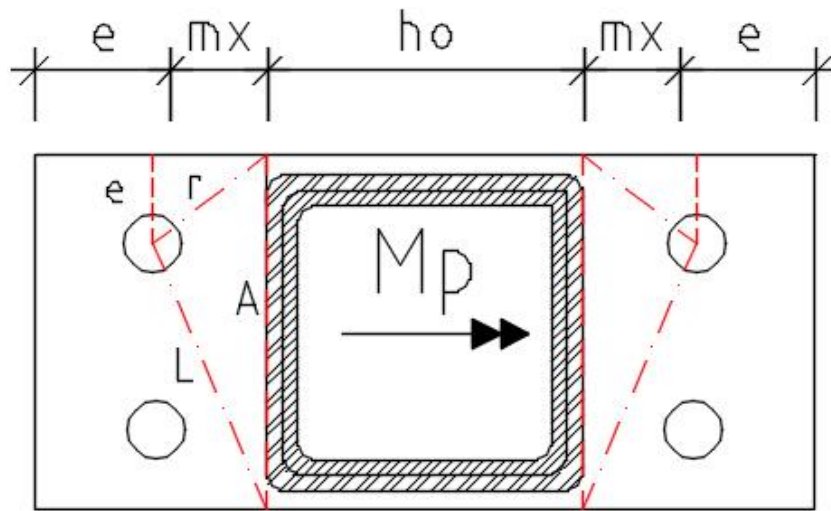
Figure 7.4: Yield mechanism 3, Specimen B weak axis

7.2.1.3 Results

Table 7.2 shows the results obtained from using the moment capacity expression for each yield cases. Yield mechanism 1 has an equal capacity compared to Specimen B when bent about the weak axis. Yield mechanism 2 has a higher capacity compared to the previous one due to having an extra yield line which is along C as shown on the diagram. The final yield mechanism has the highest moment capacity with a substantial difference compared to the other two. The nominal value of the moment arm is 2500 while the measured moment arm is 2350 mm.

	$M_p[kNm]$ Nominal values	$M_p[kNm]$ Measured values	Point load[kg] Nominal values	Point load [kg] Measured values
Yield Mechanism 1	4,4	5,7	191	247
Yield Mechanism 2	5,7	7,4	248	320
Yield Mechanism 3	8,4	10,8	364	469

Table 7.2: The moment plastic capacity of the yield mechanisms

7.2.2 Capacity for bending in the strong axis

7.2.2.1 Specimen A

The deformation of specimen A about the strong axis forms yield patterns that were observed by Uhre [7] , which is depicted on figure 7.5. The yield lines are apparent at point marked with red lines on the end plate. The expression of calculating the plastic moment capacity is obtained through virtual work, which is shown on the expression (7.3) and the in the appendix B.2.

$$m_p = 2m_p b_p \left[\frac{h_0}{m_x} + 1 \right] \tag{7.6}$$
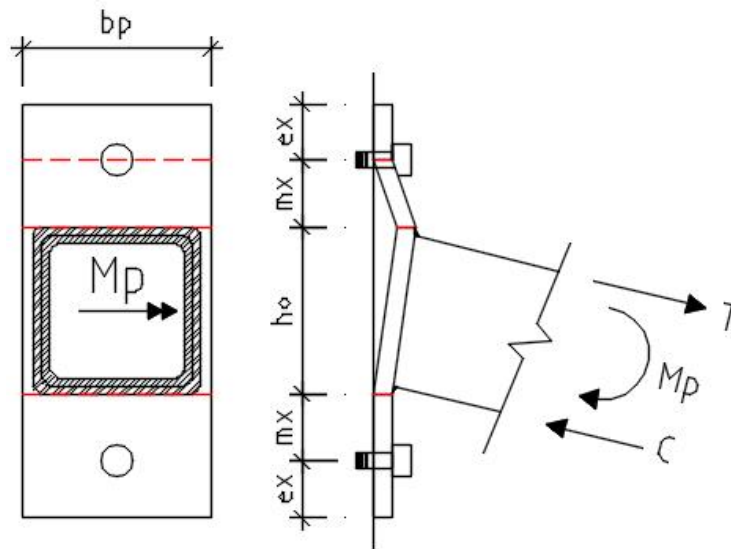
Figure 7.5: Specimen A bending about strong axis

	$M_p [kNm]$	Point load $[kg]$
Specimen A Y-axis	4,3	177
Specimen A Y-axis measured	5,6	229

Table 7.3: Results of specimen A bending about strong axis

7.2.2.2 Specimen B

The deformation of specimen B about the strong axis forms yield patterns that were observed by Kirkerud [9], which is depicted on figure 7.6. The yield lines are apparent at point marked with red lines on the end plate as demonstrated on figure 7.6. The expression of calculating the plastic moment capacity is obtained through virtual work. The moment capacity of expression can also be applied in this case despite the additional number of bolts since the yield patterns in both cases are identical and this is crucial.

$$m_p = 2m_p b_p \left[\frac{h_0}{m_x} + 1 \right] \tag{7.7}$$
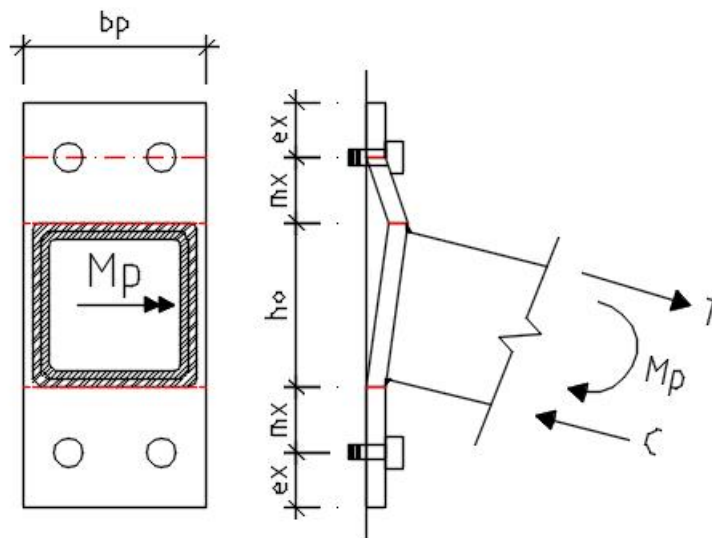
Figure 7.6: Specimen B bending about the strong axis

The bolts located on the upper part of the extended end plate is tension and the bolts below are not affected by the acting forces.

	$M_p[kNm]$	Point load $[kg]$
Specimen B Y-axis	4,3	177
Specimen B Y-axis measured	5,6	229

Table 7.4: Results of specimen B bending about strong axis

7.3 Stiffness

7.3.1 General

This chapter presents a calculation model for the stiffness of the end plate connections of high strength steel subjected to bending moment. The rules and guidelines for calculating the rotational stiffness is represented in the Eurocode [1]. The effective length of a T-stub obtained about strong axis, which is crucial in obtaining the stiffness of the joint. The capacity formulas obtained from the previous chapters are used to derive the expression of calculating the effective length about the weak axis. The expressions used in this chapter are deduced in the appendix C.

7.3.2 Specimen A
7.3.2.1 Stiffness about the weak axis

The expression (7.7) was obtained by equating the expression (4.4) with the moment capacity, which is equivalent to the force times the moment arm. The moment arm is two third of the end plates width. This is the result of the joint rotating about point *a* as demonstrated on figure (7.7). This is the contact between the end plate and the stiff wall. The yield line A increases from point a to b linearly on an inclined end plate shown on figure 7.7. The steps taken to obtain the formula of effective length for this case is shown in the appendix C.

$$l_{eff} = 0.75b_p + 1.5\frac{m_x^2}{b_p} \qquad (7.8)$$

Figure 7.7: Specimen A bending about the weak axis

7.3.2.2 Stiffness about the strong axis

The effective length in this case is obtained from table 6.6 in the EC3-1-8 [1] as being the smallest value, which is also in chapter 4.3.5.This is given again as follows:

$$l_{eff} = 0{,}5b_p \tag{7.9}$$

The effective length of the T-stub model in this case is $0{,}5b_p = 50mm$ and the resistance is 37kN as shown in the appendix table D.1.

The diagram of the yield pattern line is shown below and the effective length in this case is half of the length of the end plate.
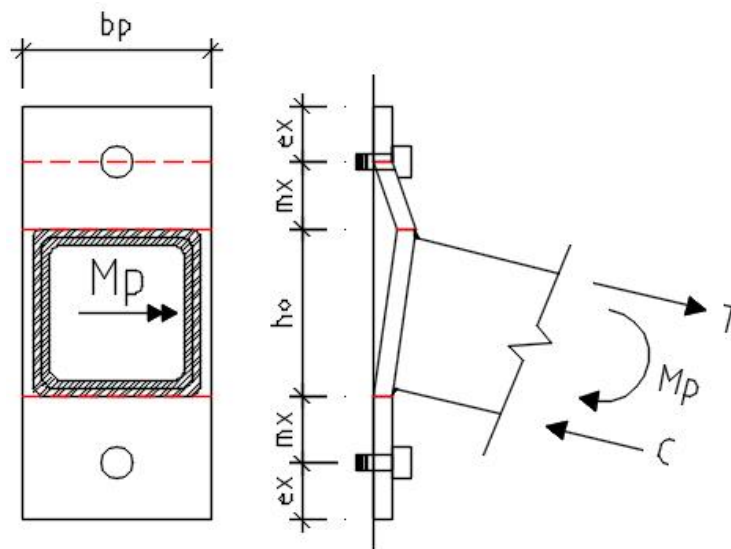
Figure 7.8: Specimen A bending about strong axis

7.3.2.3 Stiffness results stiffness of specimen A

Table 7.5 shows the results obtained from the use of expressions shown above. The nominal values are the theoretical (engineering) yield stress at 700 MPa and the thickness of the end plate is 6 mm, which in reality it's slightly different.

The $S_{j,ini}$ measured is based on the measured values which were obtained from the experiment, the actual yield stress of Weldox 700 is 820 MPa as shown on chapter 9 and the actual thickness is 6.3 mm.

	$S_{j,ini}[kNm/rad]$ (Nominal values)	$S_{j,ini}[kNm/rad]$ (Measured values)
Specimen A Y-axis	578,6	661,4
Specimen A Z-axis	337,7	386,3

Table 7.5: Stiffness results of the Specimen A--Y axis

7.3.3 Specimen B

7.3.3.1 Stiffness about the weak axis

The expression of calculating the effective length of specimen B bent about the weak axis was developed by Kirkerud [9], which is shown by this expression (7.9). This formula was retrieved by equating the expression (4.4) with expression (7.3) divided by the moment arm z given that the plastic moment capacity is known in both cases as shown at expression (4.7). The effective length is obtained as shown below and the procedure taken to obtain this expression is shown in the appendix C.2. Furthermore, the effective length should not exceed the actual width of the end plate, which is 100 mm as shown on appendix E.2.

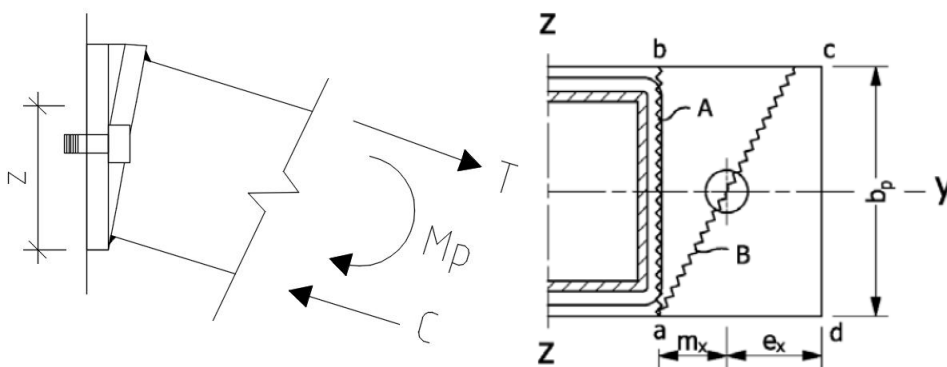$$l_{eff} = \frac{1}{2z}\left[b_p^2 + 2m^2\right] \tag{7.10}$$
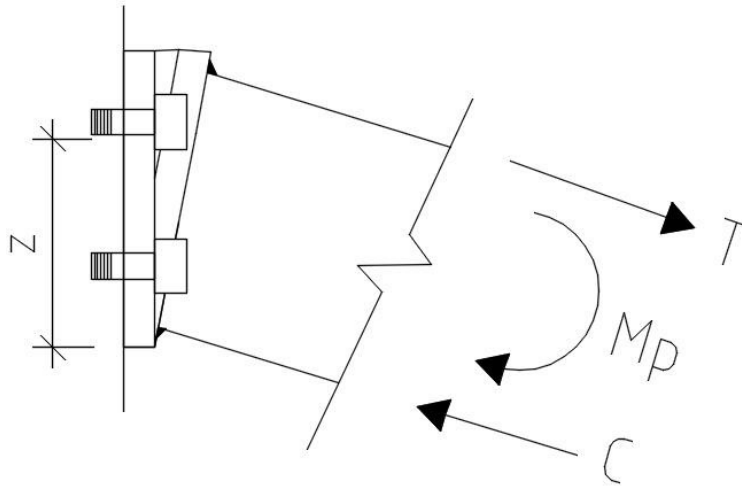
Figure 7.9: Specimen B, bending about weak axis

7.3.3.2 Stiffness about the strong axis

The effective length in this case is obtained from table 6.6 [1] as being the smallest value. This is given again as follows:

$$l_{eff} = 0{,}5b_p \qquad\qquad (7.11)$$

The moment arm in this situation is equivalent to the distance from the centre of the bolts in tension to the compression centre, which is assumed to be located between the weld and the lower part of the profile. As demonstrated on the figure below.
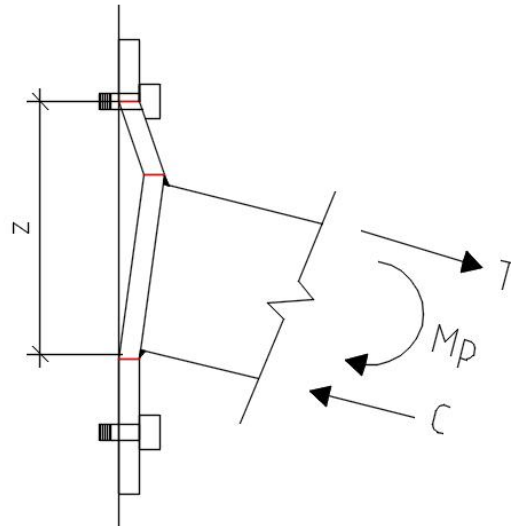
Figure 7.10: Specimen B bending about strong axis

7.3.3.3 Stiffness results of specimen B

The results are shown on the table below and the steps taken to obtain these results are shown in the appendix… The effective length calculated for these yield mechanism were 158 mm and 149 mm. Therefore the rotational stiffness of the yield mechanism 2 and 3 have the same value because their effective length exceeded the width of the end plate. The $S_{j,ini}$ measured is based on the measured values which were obtained from the experiment and these are 820 Mpa and 6.3 mm.

	$S_{j,ini}[kNm/rad]$ (Nominal values)	$S_J[kNm/rad]$ (Measured values)
Specimen B Y-axis	602	694
Specimen B Z-axis	339	388
Specimen B Z-axis Yield mech_2&3	358	409

8 Comparisons of results between hand calculations and the experiments.

In this chapter the analytical results depicted on chapter 7 are compared to the experiment's results on the basis of measured values of the specimens. Each specimens with their respective bending axis are presented on the tables and graphs below. The hand calculations for the stiffness and the capacity are demonstrated in the appendix D and E.

8.1 Specimen A

8.1.1 Bending about the weak axis

Table 8.1 shows the results obtained from the two method of analysis. As noted, the hand calculation overestimates substantially especially the initial stiffness by almost 50%. On the other hand, the calculated capacity is marginally greater than experiment's capacity by approximately 6 %.

Method of analysis	$S_{jini,zA} \left[\dfrac{kNm}{rad} \right]$	Capacity [kNm]
Hand Calculations	386,3	5,7
Lab experiment	191,2	5,3

Table 8.1: Specimen A results

The values obtained from the hand calculation as are also depicted on figure 8.1 together with the response curve. The response curve and the yield mechanism are converging at an approximately similar point. Although, the calculated initial stiffness curve is much steeper in relation to the loading curve.
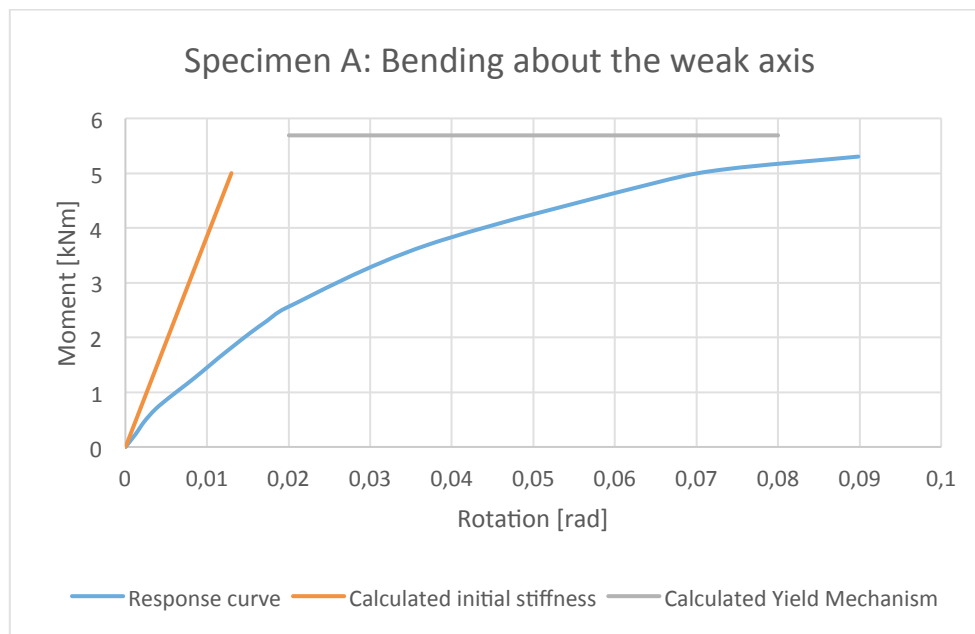
Figure 8.1: Specimen A bending about the weak axis

8.1.2 Bending about the strong axis

As shown on table 8.2 the analytical calculations overestimates the initial stiffness by 30 % but the calculated capacity is lower than the value obtained from the laboratory by 21%.

Method of analysis	$S_{jini,y,A}\left[\dfrac{kNm}{rad}\right]$	Capacity [kNm]
Hand Calculations	661,4	5,6
Lab experiment	463,7	7,1

Table 8.2: The capacity and initial stiffness results for specimen A

The calculated values are displayed on the graph below. The initial stiffness curve does not entirely coincide with loading curve in the elastic region. The loading curve surpasses the calculated yield mechanism curve as shown on figure 8.2.

Figure 8.2: Specimen A bending about the strong axis

8.2 Specimen B

8.2.1 Bending about the weak axis

The results of the hand calculations as depicted on table 8.3 are within the acceptable range in relation to the results obtained from the experiment. The hand calculation has predicted the values on table 8.43 with an uncertainty approximately at 15 %. The results of the hand calculations are obtained from the expression (4.12) for the initial stiffness and chapter 7.2.1.2.

Method of analysis	$S_{jini,z,B}\left[\dfrac{kNm}{rad}\right]$	Capacity [kNm]
Hand Calculations Yield mech-1	387,8	5,8
Lab experiment	429,6	6,7

Table 8.3: Results of capacity and the initial stiffness of B

The following alternative yield mechanisms for specimen B are shown on table 8.4. The results obtained from yield mechanism 2 are closer to the experiments result compared to yield mechanism 1 when it comes to the initial stiffness. Yet, its capacity at 9 kNm is much higher compared to 5.7 kNm. Both capacities of yield mechanism 2 and the experiment are marginally equal.

Method of analysis	$S_{jini,z,B}\left[\dfrac{kNm}{rad}\right]$	Capacity [kNm]
Calc-Yield mech-2	408,7	7,4
Calc-Yield mech-3	408,7	10,8
Lab experiment	429,6	5,7

Table 8.4: The results of capacity and the initial stiffness of yield mechanism of B

Figure 8.3 shows the loading curve with the graphed initial stiffness and capacity obtained from table 8.3. The calculated initial stiffness coincides relatively adequate in relation to the actual stiffness of 429.6 kNm/rad.

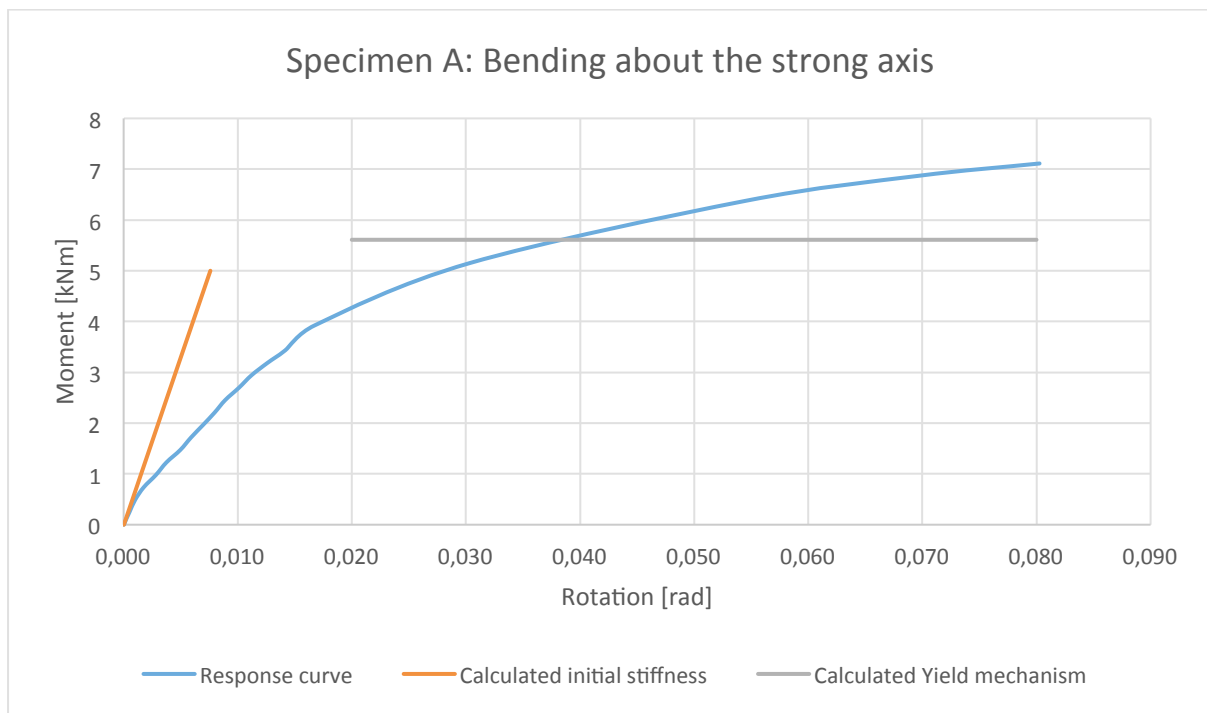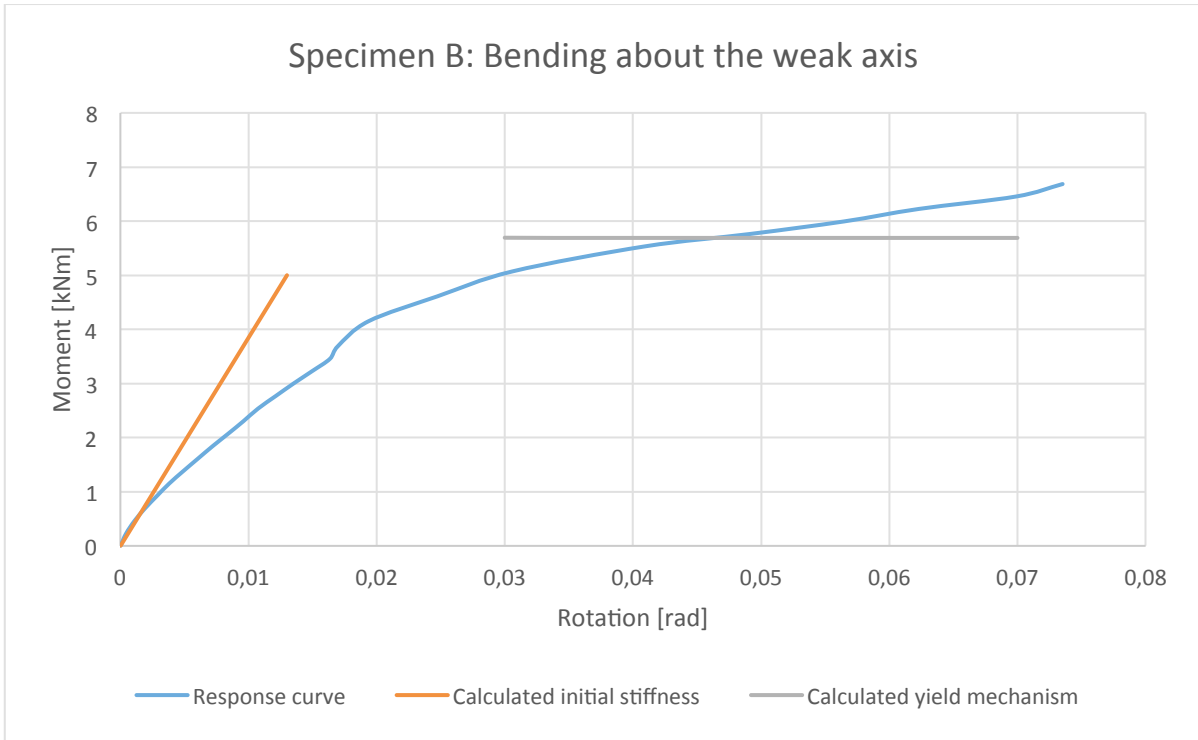**Figure 8.3: Specimen B, bending about the weak axis**

8.2.2 Bending about the strong axis

The hand calculation overestimates the initial stiffness by 15 %. On the contrary it underestimates the capacity by 40 % as shown on table 8.4.

Method of analysis	$S_{jini,y,B} \left[\dfrac{kNm}{rad} \right]$	Capacity $[kNm]$
Hand Calculations	693,7	5,6
Lab experiment	593,8	8,8

Figure 8.4: The results of capacity and initial stiffness of specimen B

Figure 8.5 shows the values from table 8.4 together with the response curve, which was obtained from the experiment. The initial stiffness curve obtained from the hand calculations interprets the loading curve relatively well.

Figure 8.5: Specimen B bending about the strong axis

8.2.3 Discussion

Based on the available data depicted above, the hand calculations overestimates the capacity and the initial stiffness when Specimen A i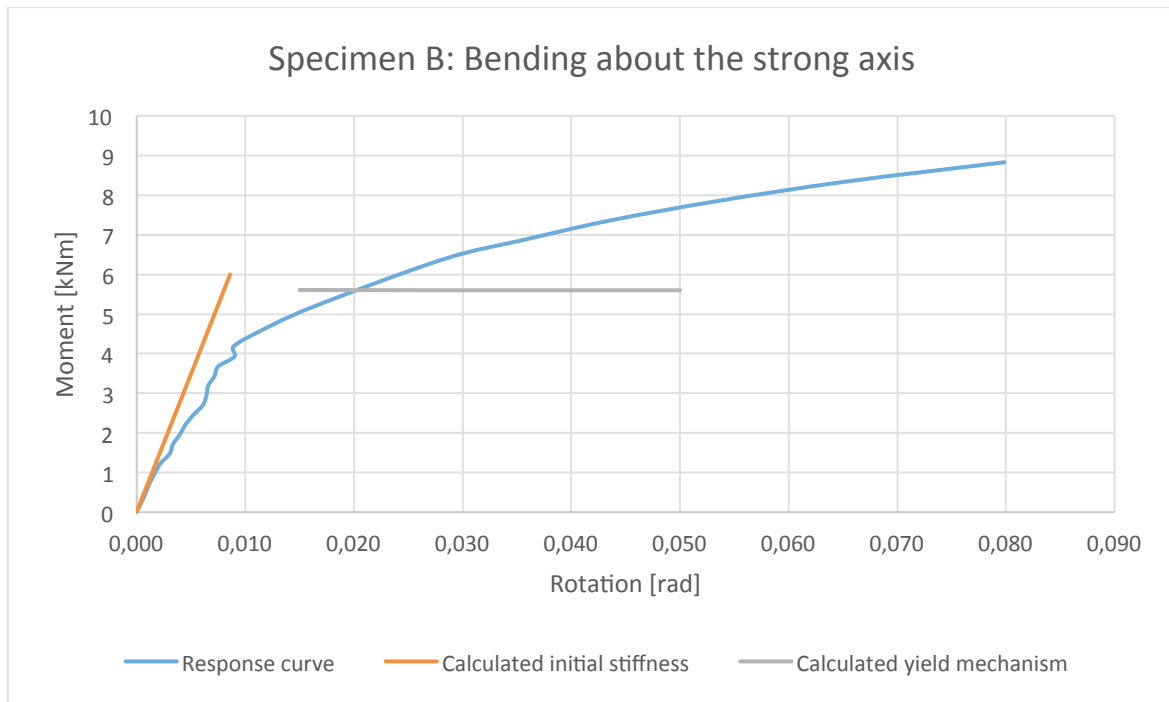s subjected to bending about the weak axis. In other words the analytical results are leaning on the conservative side. As for the bending about the strong axis for Specimen A, the initial stiffness obtained analytically is also overestimated by 30 % and this is the opposite case for the capacity. Therefore the analytical calculations are conservative for both bending axis of specimen A when dealing with initial stiffness. This circumstance was also observed with specimen B when bent about both axis. Furthermore, the analytical calculations underestimates the capacity for specimen A and B only when bent about the strong axis.

Table 8.5 shows the capacity utilization of each specimens when bent about the weak and strong axis.

Specimen	Bending about an axis	Capacity Utilization $\dfrac{M_p}{M_{max}}$
Specimen A	Weak	1,1
Specimen A	Strong	0,79
Specimen B	Weak	0,87
Specimen B	strong	0,64

Table 8.5: The capacity utilization of moment capacity and the ultimate moment

78

9 Numerical analysis

9.1 Introduction

Numerical analysis of a column base welded to an extended end plate of high strength steel was conducted in Abaqus 6.14-1, which is one of the alternative procedures in this investigation. The laboratory experiments is simulated in Abaqus so as to produce expected equivalent results with uncertainties. The Abaqus models for specimen A and B were initially constructed by the previous students. The models has undergone some few modifications to fit with the use of high strength steel in this investigation. These were used to obtain numerical results for this investigation depicted in the moment-rotation graphs.

This chapter describes the general procedures undergone to create the Abaqus models since the previous students have already explained it in detail. Furthermore the results obtained from numerical simulations are also presented.

9.2 The analysis models of the two specimens

The Abaqus models represents the actual geometries of the specimens as shown on figure 9.1. The specimens are rather complex in nature compared to the Abaqus models because simplifications of the model's geometries had to be into consideration so as convergence takes place.
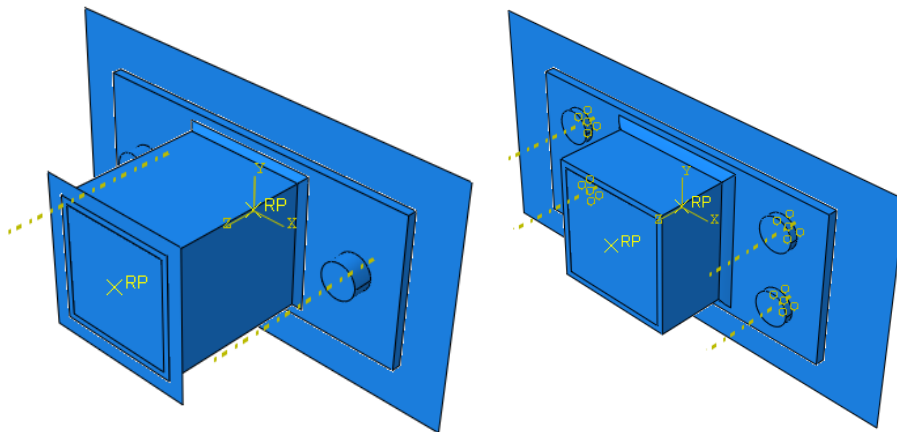
Figure 9.1: Specimen A and B

The lengths of the hollow profiles for both Abaqus specimen is much shorter than the actual ones. It is 100 mm and 50 mm long for specimen A and B respectively. Bringsvor and Kirkerud's parameter studies show that the Abaqus model gives approximately the same results irrespective of the profile length based on their parameter study [8] [9].The bolts thread length is reduced to the length equivalent to end plates' thickness at 6mm.

Furthermore the bolts are placed towards the edge of the holes on the end plates so as to establish contact so as the analysis can initiate. Otherwise the models would not converge if the bolts were placed in the middle of the holes. Figure 9.2 demonstrates the positions of the bolts according the bending of the column base about strong and weak axis.
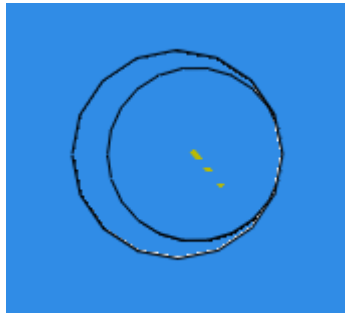

Figure 9.2: The placement of the bolt in the hole.

9.2.1 Material properties

The components of the Abaqus models are assigned to their material properties so as to simulate the actual scenario described in chapter as accurate as possible. The elastic properties for all components are can be found in NS EN 1993-1-1 [21], which is also shown in the table… below.

Young's modulus (E)	210 000 Mpa
Poisson's ratio (v)	0,3

Table 9.1: Elastic properties of the materials

The plastic properties of the components used in this investigation are retrieved from the tensile tests conducted initially by Karlsen [2], which were also used by most previous students mentioned in chapter 2. The plastic properties of the components are shown on table 9.2.

Components	$\sigma\ [Mpa]$	ε_{pl}
Weld	600	0
	700	0,02
	800	0,06
Bolts	640	0
	896	0,1091

Components	$\sigma\ [Mpa]$	ε_{pl}
Hollow profile	440	0
	441	0,02015
	549	0,05664
	597	0,09477
	620	0,12710

Table 9.2: Plastic properties of the components

9.2.2 End plate

The plastic properties of the W700 end plate was retrieved from the tensile strength testing conducted in the laboratory. The results are shown on figure 9.1 and it's apparent that the material starts to yield around 820 Mpa, which is greater than the theoretical yield stress at 700 Mpa.
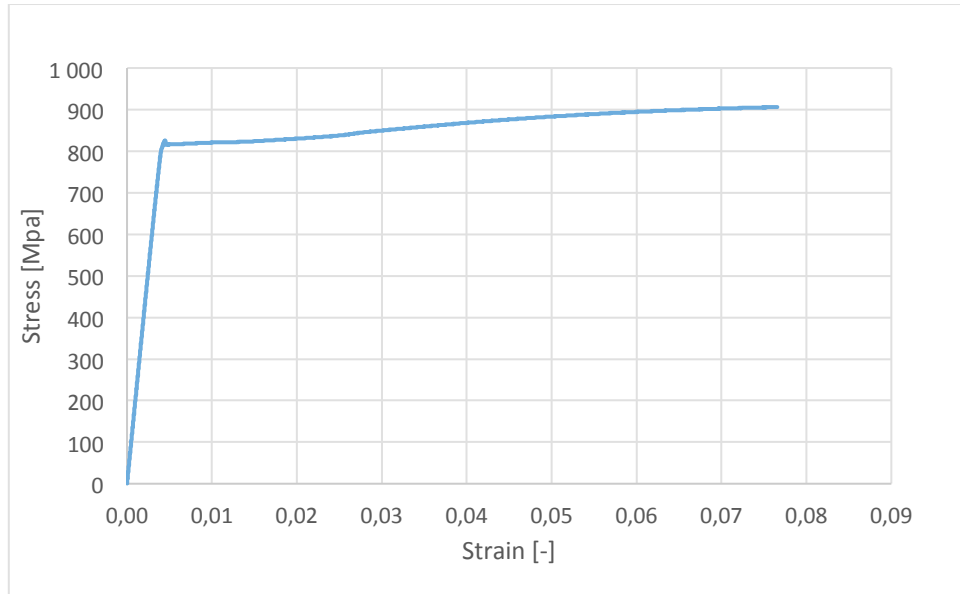

Figure 9.3: The results from the tensile testing of W700

9.2.3 Element type

Two kinds of elements were used on different components and these are C3D8R and C3D10. C3D8R is a cubical volume element of 8 nodes, which are positioned in the corners of the element as demonstrated on figure 9.2. Reduced integration is taken into consideration with this particular element, which is positioned in the middle. It contributes to accurate results at a faster computational time [26]. These elements are assigned to end plate and the hollow profile. The number of elements throughout the thickness of the hollow profile for specimen A and B is 1. In the end plate's case for specimen A and B is 4 as shown on figure 9.2 and 9.3.
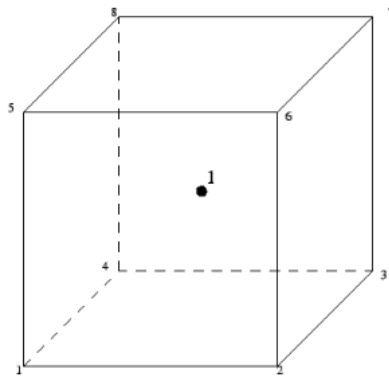
Figure 9.4: 8 node cubical volume element

C3D10 is a 10 node tetrahedral element [26], which is assigned to welds and bolts. This type of model is suitable for rather complex figures. The number of elements throughout the thickness of the thread length is 2 and 3 for specimen A and B respectively. The figure below shows the mesh of the joint components in Abaqus. The corner section of the weld and the end plate is only presented below. This makes it easier to see the composition of the element on the component's surface.
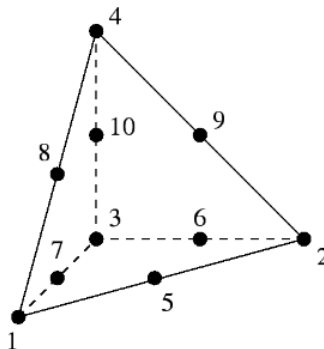
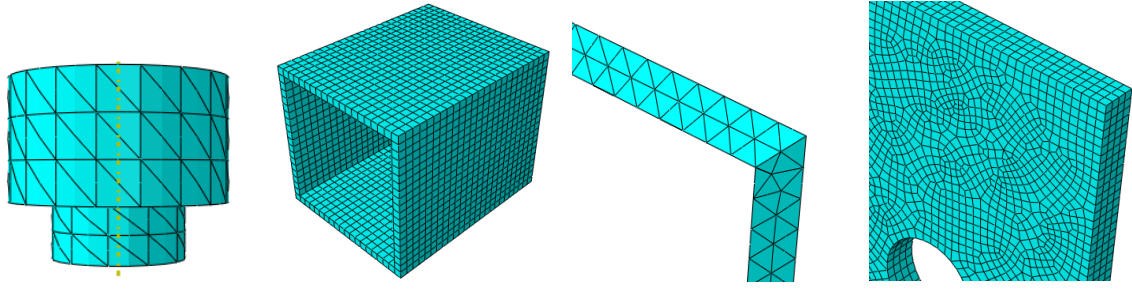**Figure 9.5: 10 node tetrahedral element**

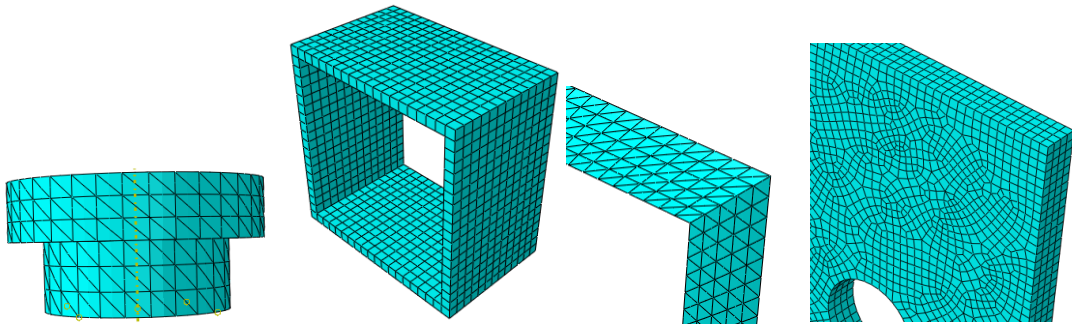**Figure 9.6: Abaqus model of specimen A**

Figure 9.7: Abaqus model of specimen B

9.2.4   Data extraction

In the laboratory a point load is placed at the tip of the cantilever beam to create moment at the joint. In the simulation case, rotation is placed on the analytical stiff plate at the same position where the reference point is placed. The procedures of how the front (analytical) stiff plate was placed onto the column cantilever beam is already been explained by Bringsvor and Kirkerud including the boundary conditions of each components in the joint [9] [8]. The node is also placed at the reference point to extract data as shown on figure 9.8, which contributes to the setup of the graphs as shown in chapter 10. The rotation of the joint is limited at 0.1 radians for bending about weak and strong axis. The Abaqus models for both specimens operate with the maximum increment size of 0.02 at a total duration equivalent to 1.
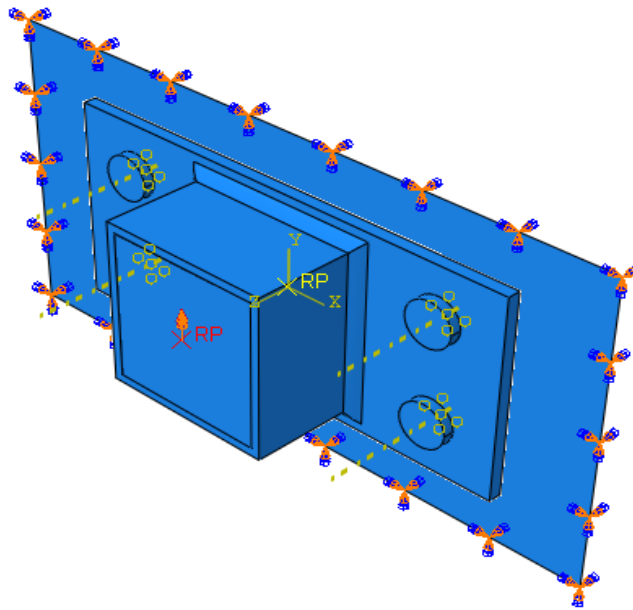
Figure 9.8: The application of the rotation at the reference point

9.2.5 Comparisons of deformation patterns

This chapter shows the comparisons between the deformation patterns obtained from the numerical simulations and the actual patterns from the experiment. As mentioned before the numerical models are less complex compared to the actual ones in term of the geometrical structure. The results are presented in chapter 10 and it is compared to the results retrieved from the experiment.

Figure 9.9: Deformation of specimen A about the weak axis
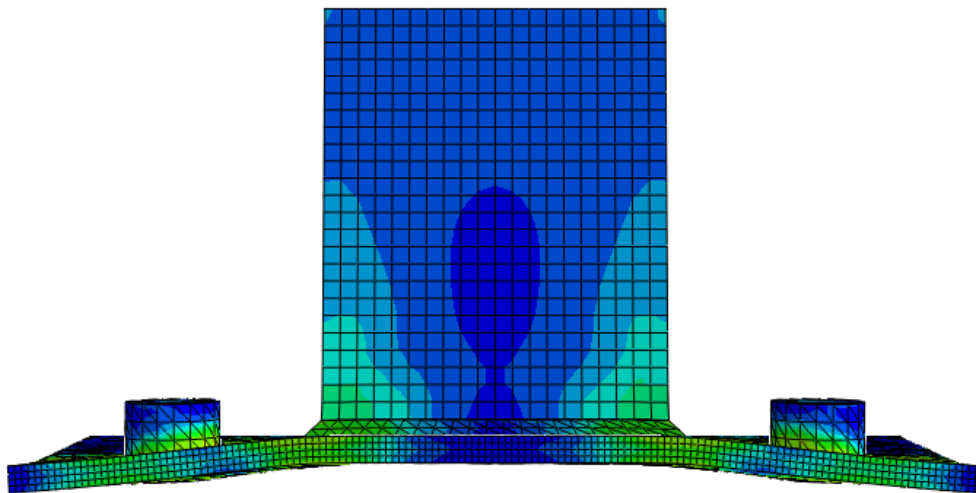
Figure 9.10: Numerical deformation of specimen A about the weak axis

Figure 9.11: Deformation of specimen A about the strong axis
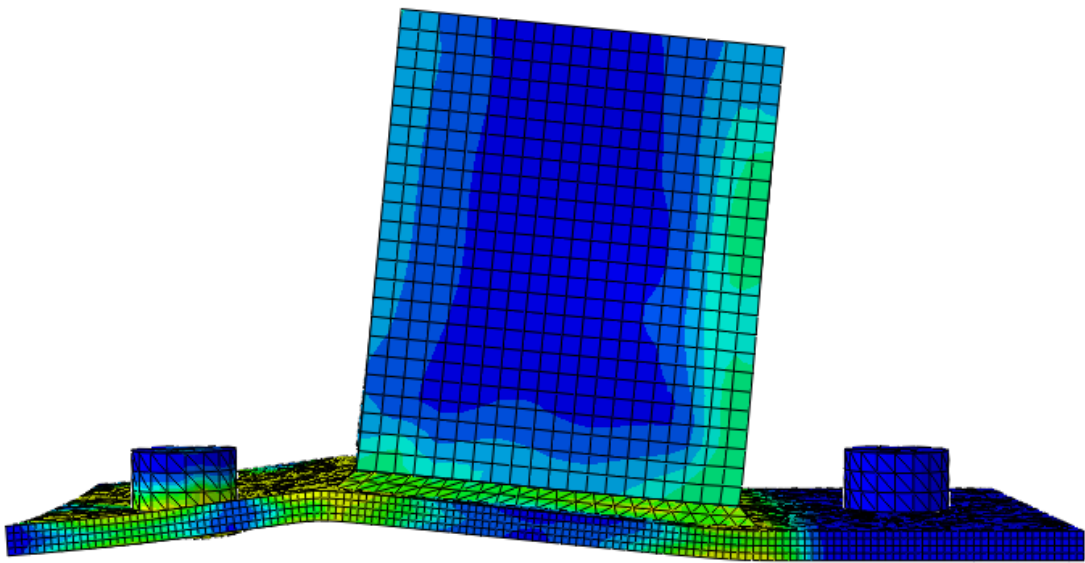
Figure 9.12: Numerical deformation of specimen A about the weak axis

Figure 9.13: Deformation of the specimen B about the weak axis

Figure 9.14: Numerical deformation of specimen B about the weak axis

Figure 9.15: Deformation of specimen B about the strong axis

Figure 9.16: Numerical deformation of specimen B about the strong axis
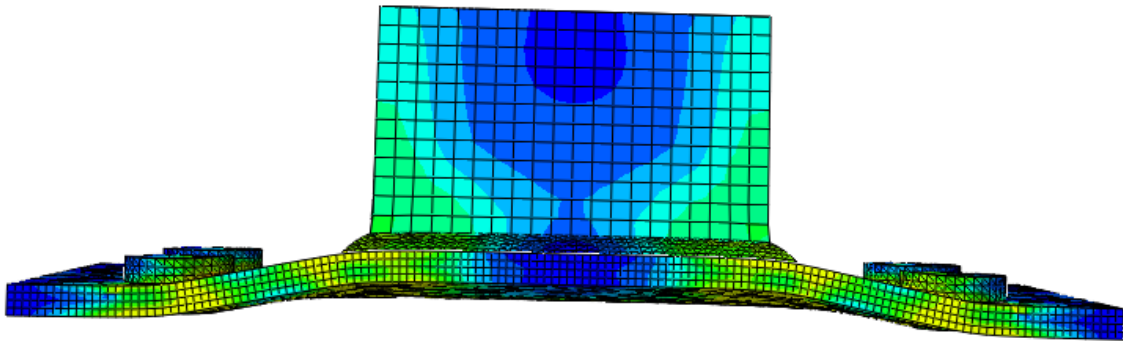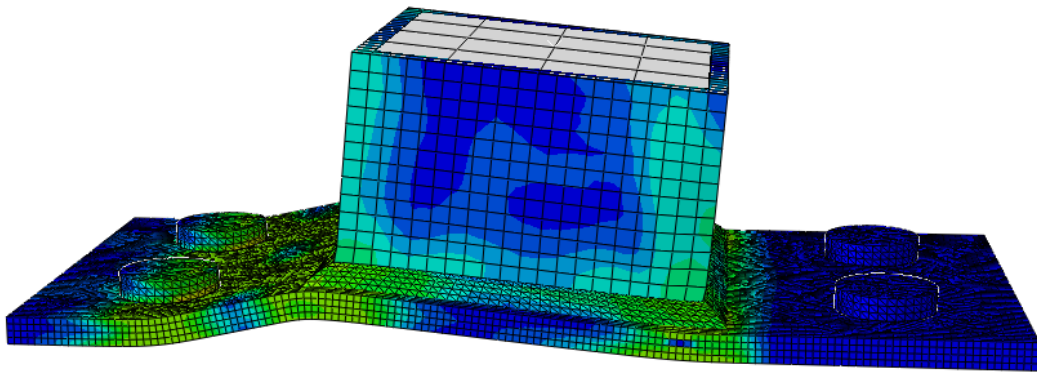
The figures of the numerical deformations shows how accurate Abaqus models produces these models compared to the actual deformation. The lighter colours represents the higher stress subjected by the components

9.3   The bulging deformation on the RHS profile.

The RHS profiles in the Abaqus models had a bulging surface after the numerical analysis of specimen A and B were processed. This occurs when the lower part of the RHS profile bends inwards as demonstrated by the red circle on figure 9.17, which in reality is very unlikely to occur as demonstrated by a red circle on figure 9.18 from the actual experiment for specimen A, bending about the strong axis.

The solution in this case was assigning 2 volume elements of C3D8R elements across the width of the RHS profile. The result of the numerical analysis produced a RHS without a bulging surface as demonstrated on figure 9.19. This would give an adequate interpretation of the bending stresses, which occurs in the transitions point between the weld and the profile. The result of figure 9.19 is demonstrated in chapter 11.3.
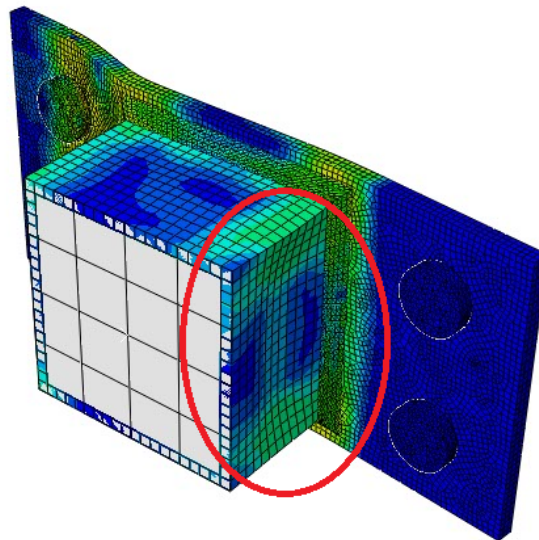

Figure 9.17: Example of the bulging of the RHS profile

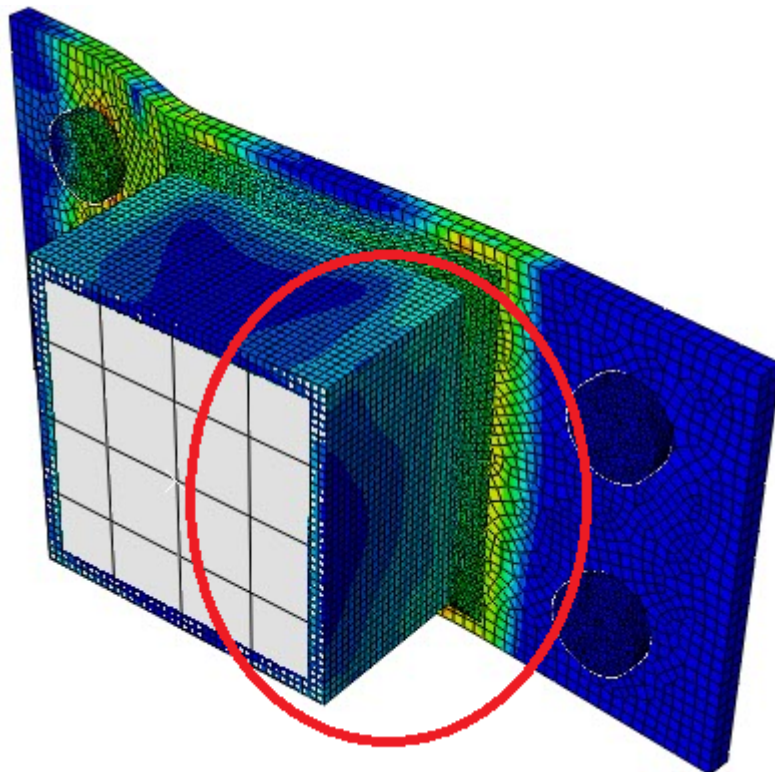**Figure 9.18: The bottom of the RHS profile of specimen A**

**Figure 9.19: The RHS profile without the bulging surface**

10 Comparisons of results between numerical analysis and the experiment

In this chapter the stiffness and the capacity obtained from the experiment and the numerical simulations are compared to each other. The capacity and the stiffness for both specimens about the weak and the strong axis are tabulated in the following chapters. The actual thickness of the end plate is 6.3 mm and 6.0 mm in the Abaqus model. The graphs illustrated in the following chapters only show the initial stiffness curves of each models so as to see the comparisons between the simulation curve and the response curve properly.

10.1 Specimen A.

10.1.1 Bending about the weak axis.

The results from both models are shown on table 10.1. The moment capacity, initial stiffness and the secant stiffness ($\frac{2}{3}M_{j,Rd}$) of Specimen A modelled in Abaqus are approximately equivalent to the results obtained from the laboratory. This is a good indication that Abaqus represents adequate results. On the other hand, the substantial difference between the initial stiffness lies at 33 %.
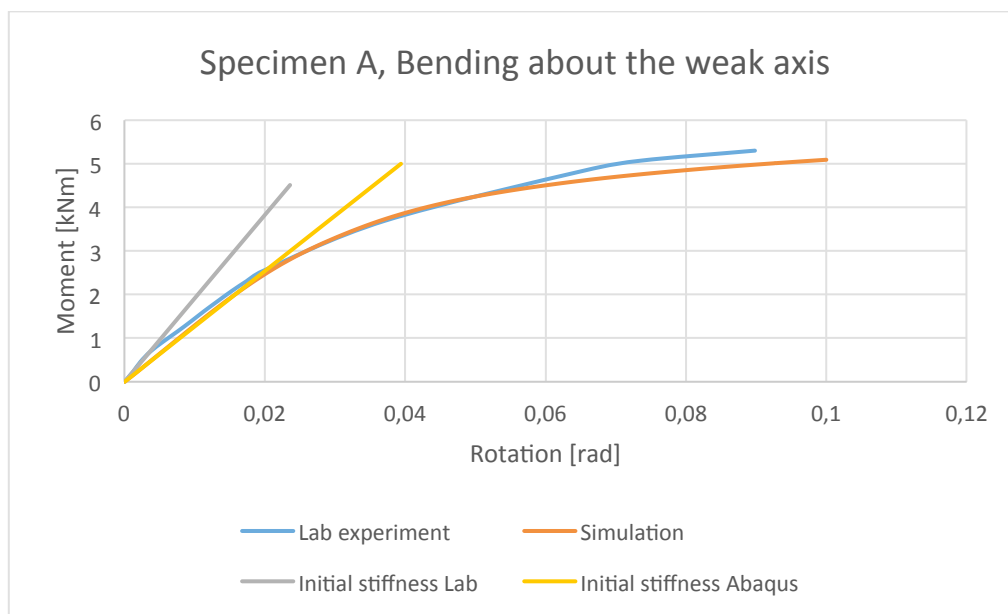
	$S_{jini,zA}\left[\dfrac{kNm}{rad}\right]$	$S_{J,zA}\left[\dfrac{kNm}{rad}\right]$	Capacity [kNm]
Abaqus Simulation	126,9	108,2	5,1
Lab experiment	191,2	109,8	5,3

Table 10.1: The results of the lab experiment and Abaqus

The initial stiffness as mentioned is the average of the $M - \varphi$ gradient values in the elastic region which is equivalent to 10 to 30 kg. Both curves in this case are approximately the same especially on the bending point but there is a slight difference in the elastic region. The curves deviates as the deformation progresses and this starts at approximately 4.34 kNm, which is equivalent to 188 kg.

10.1.2 Bending about the strong axis.

The discrepancies in all three cases have increased compared to the previous one especially in the case of the initial stiffness at almost 50 % while the other values lie within the acceptable range.

	$S_{jini,y,A} \left[\dfrac{kNm}{rad}\right]$	$S_{J,y,A} \left[\dfrac{kNm}{rad}\right]$	Capacity [kNm]
Abaqus Simulation	223,6	185,6	6,6
Lab experiment	463,7	192,9	7,1

Table 10.2: The results of the lab experiment and Abaqus
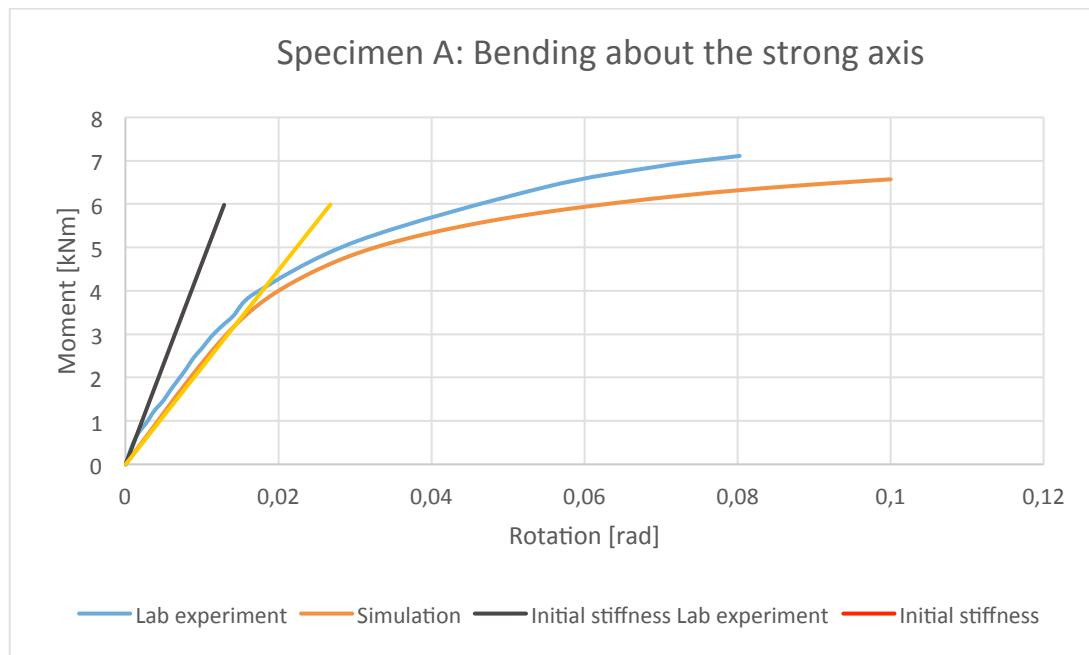

Figure 10.1: Specimen A, bending about the strong axis

The Abaqus model as depicted on figure 10.3 underestimates the capacity and the stiffness of specimen B by having a lower steepness compared to the counterpart. Both curves are almost parallel from the start but the deviation initiates as both curve enter the plastic region.

10.2 Specimen B

10.2.1 Bending about the weak axis.

The initial stiffness obtained from the simulations is approximately 50% lower compared to the one obtained from the experiment.

	$S_{jini,zB} \left[\dfrac{kNm}{rad}\right]$	$S_{J,z,B} \left[\dfrac{kNm}{rad}\right]$	Capacity $[kNm]$
Abaqus Simulation	222,4	178,6	6,3
Lab experiment	429,6	198,7	6,7

Table 10.3: The results of the lab experiment and Abaqus
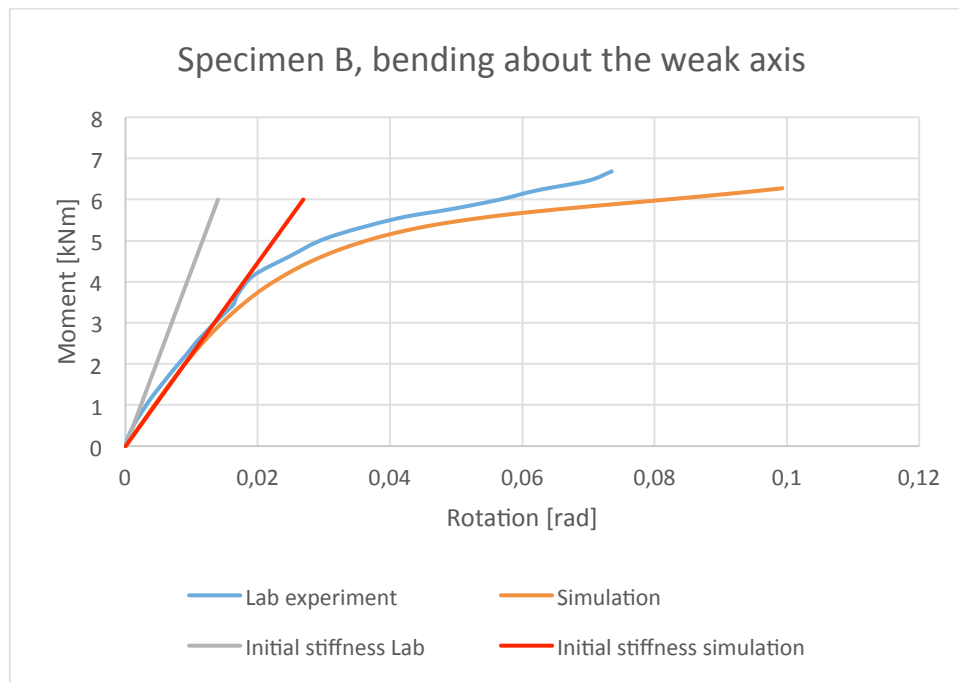

Figure 10.2: Specimen B, bending about the weak axis

The simulation curve interprets the lab experiment curve very well especially on the elastic region as shown on figure 10.5. The deviation as previously noted initiates as both curves enters the plastic region, which is noticeable with the knee point of the lab experiment curve.

10.2.2 Bending about the strong axis.

The Abaqus models predicts the moment capacity very well as demonstrated on table 10.6 and the rotational stiffness are within acceptable range. As observed before the initial stiffness case is obtained from the experiment is 36% higher than the counterpart.

	$S_{jini,zA} \left[\dfrac{kNm}{rad}\right]$	$S_{J,ZA} \left[\dfrac{kNm}{rad}\right]$	Capacity [kNm]
Abaqus Simulation	374,5	296,5	7,8
Lab experiment	593,7	261,4	8,8

Table 10.4: The results of the lab experiment and Abaqus

Both curves do not entirely coincide with each other especially in the elastic region in relation to the previous curves. The simulation and the experiment curve deviate from each other from the knee point as observed from the previous curves.
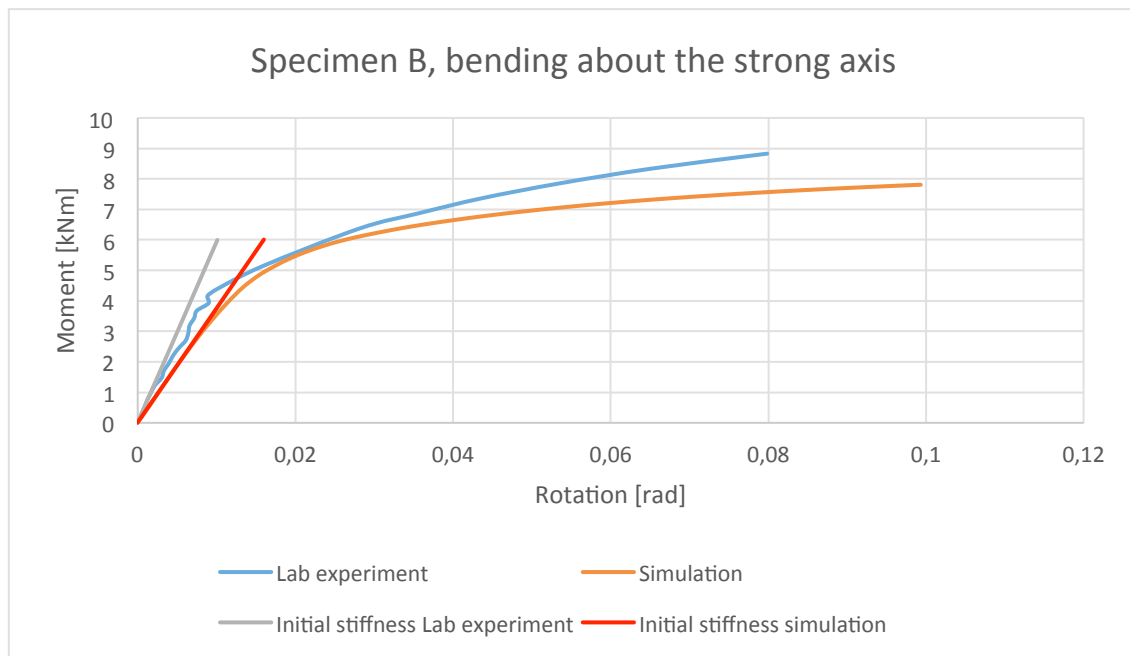

Figure 10.3: Specimen B, bending about the strong axis

10.3 Results

Generally the Abaqus model is a good prediction tool for predicting the response curve in this case. The Abaqus model underestimates the initial stiffness of both specimens when bent about both axis even up to 50 %. Furthermore, the numerical simulations do not take into account to clamping forces and tensioning forces which influences the rigidity of the connection's stiffness in the actual experiment. This is the reason to the differences between the experimental and numerical stiffness. As shown from the previous figures including figure 10.3

As Uhre discussed that the initial part of the response curve would ideally be linear over a significant part of the loading range, which makes it easier for the initial stiffness to define that part [25]. This corresponds well with the Abaqus models that has a perfect linear elastic range compared to the response curve obtained from the experiment. This is the reason of high uncertainty for the initial stiffness prediction.

Table 10.5 gives an overview of the uncertainties the simulation model in relation to the experiment model. As demonstrated on table 10.5 the Abaqus predicts the capacity of the specimens very well when compared to the results obtained from the lab.

Specimen, Bending axis	Initial stiffness uncertainty $\left[\dfrac{S_{J,ini.abaqus}}{S_{J,ini.exp}}\right]$	Capacity uncertainty $\left[\dfrac{C_{abaqus}}{C_{experiment}}\right]$
Specimen A, weak axis	0,66	0,96
Specimen A, strong axis	0,48	0,93
Specimen B, weak axis	0,52	0,94
Specimen B, strong axis	0,63	0,89

Table 10.5: Uncertainty for the results comparisons between simulation model and experiment model

11 Parameter study

The parameter study was conducted in this investigation to determine an optimal number of elements across the thickness of the end plate. The parameter study in this investigation follows the same procedure as Bringsvor did [8]. The end plate is modelled in Abaqus as a simply supported beam and the end plate's geometry is kept the same as demonstrated on figure 11.2.The results retrieved from Abaqus are compared to the analytical deflection, which is calculated from this formula [24].

$$u_{max} = \frac{5}{384} \frac{qL^4}{EI} \tag{11.1}$$

The table below shows the values used in the simulations to compute the deflection.

q'	1 Mpa
E	210 000 Mpa
L	220 mm
b	100 mm
H	6 mm
q= q'b	100 N/mm
I= bh^3/12	1800 mm^4

Table 11.1: Values used to calculate the maximum analytical deflection

The end plate is loaded by a uniformly distributed load of 1 N/mm^2 and the maximum deflection that occurs in the middle is compared to the analytical value so as to determine the deviation. The purpose of this study is to determine the suitable number of elements across the thickness of the endplate in order to improve the accuracy of the Abaqus simulations. The figure of the end plate set up in Abaqus is displayed on the figure below. Figure 11.2 shows the bending of the end plate when its thickness contains 5 elements of C3D84R.
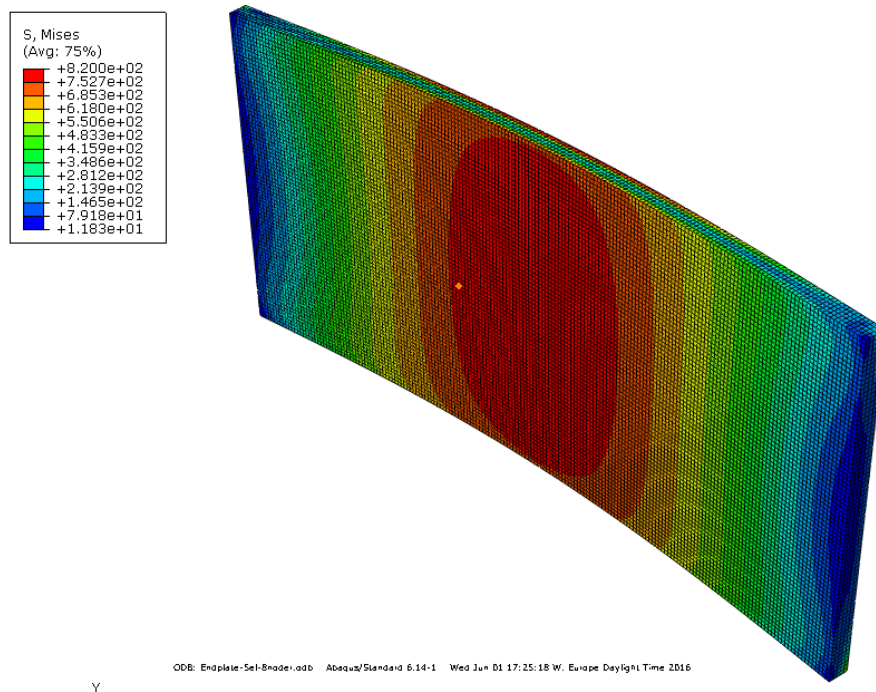

Table 11.2: End plate as a simply supported beam in bending

11.1 The elements chosen

The end plate was initially assigned with an element of C3D8R as demonstrated on figure 9.4 by the previous student's simulations models. C3D8R is a cubical element containing 8 nodes on each corners. The reduced integration point is located at the centroid point of the element as demonstrated on figure 9.4 [26]. This contributes to adequate convergence time (less computational time) and accurate results.

In this investigation the C3D20R element was assigned to the end plate with varying number across the thickness of the end plate. C3D20R is a cubical element with reduced integration (2x2x2 integration points), which contains 20 nodes as demonstrated on figure 11.1 .This element is suitable for bending situations and rarely exhibits hour glass points despite the reduced integration [26].
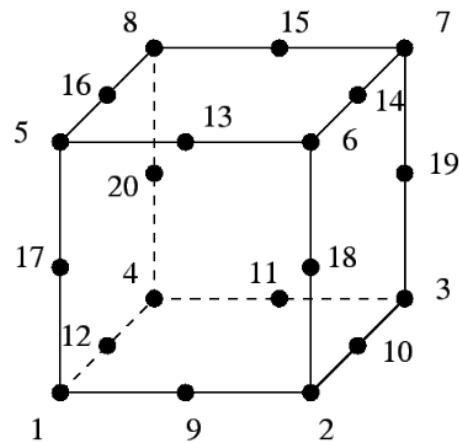

Figure 11.1: C3D20R element

11.2 Results

The table below shows the results from the simulations when the C3D8R and C3D20R elements are used, which are plotted on the graph displayed on figure.

Number of elements	Deflection [mm]	Uncertainty [%]
2	10,63	31,7
3	9,10	12,8
4	8,68	7,62
5	8,51	5,57
8	8,44	4,62
U_{max}	8,07	-

Table 11.3: Results from the C3D8R element

Number of elements	Deflection [mm]	Uncertainty [%]
2	8,16	1,12
3	8,25	2,26
4	8,35	3,52
5	8,37	3,79
8	-	-
U_{max}	8,07	-

Table 11.4: Results from the C3D20R element

The job assigned in Abaqus was aborted when the end plate had 8 number of elements across its thickness due to the computer not having enough capacity to process this model.

The graph shows that the C3D20R element gives an instant accurate analysis at two number of elements with an uncertainty of 1.12%. The C3D8R curve converges to the analytical deflection curve at a much slower rate.
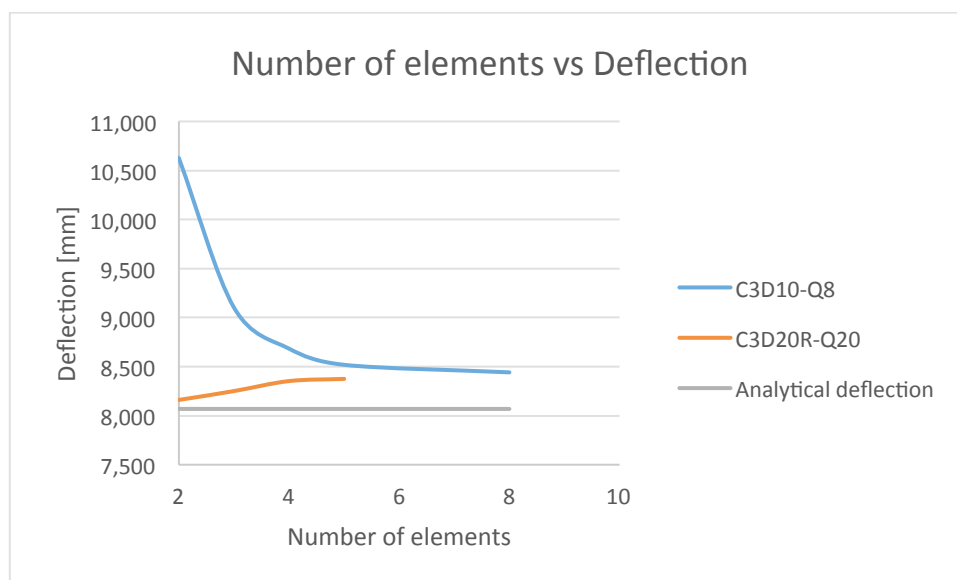

Figure 11.2: The graph of number of elements and the deflection

Based on the results from the previous investigation as shown on figure 11.2, the C3D20R element was then used on the Abaqus model for specimen B bending about the weak to observe how accurate it can simulate the actual deformation.

Figure 11.3 shows the simulation curve and the response curve, which is quite similar compared to figure 10.3. The end plate has 2 elements of C3D20R and the RHS profile had 1 element of C3D8R. Dealing with C3D20R elements has much higher effect on the computational time. Therefore the job was stopped at approximately over 0.04 rad, which is the reason to why the simulation curve in figure 11.3 is incomplete in relation to the response curve.
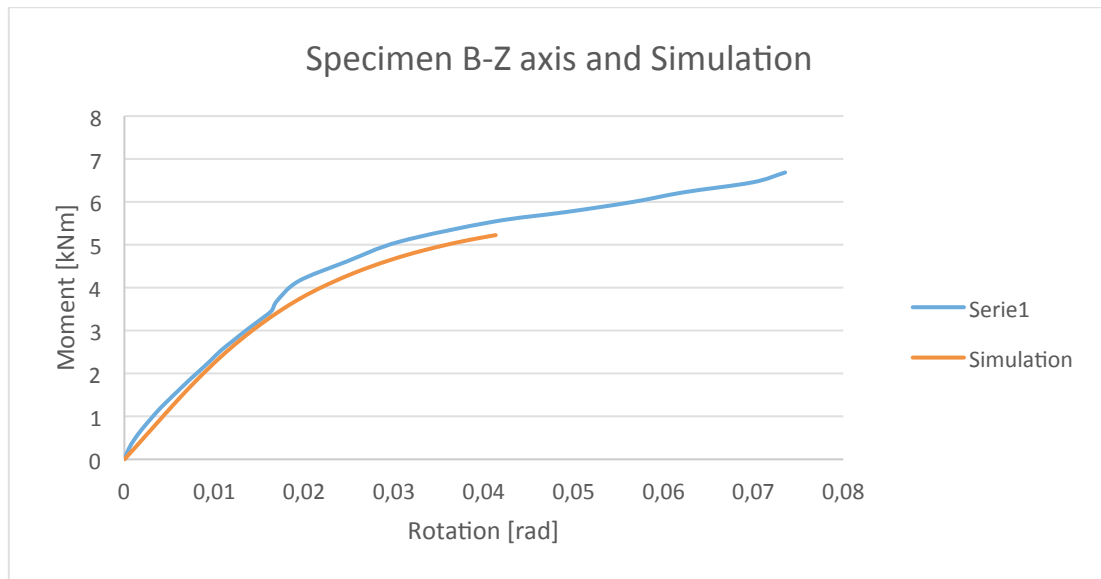

Figure 11.3: Specimen B bending about the weak axis with 2 C3D20R elements and C3D8R element

Despite the long computational time when dealing with C3D20R elements, another study was conducted and this time the end plate had 2 elements of C3D20R and RHS profile had 2 elements of C3D8R. The results on figure 11.4 describes the response curve perfectly compared to figure 11.3. The computational time was the main disadvantage and this took 4 hours to arrive to the results shown on figure 11.4 until the simulation model was automatically aborted.
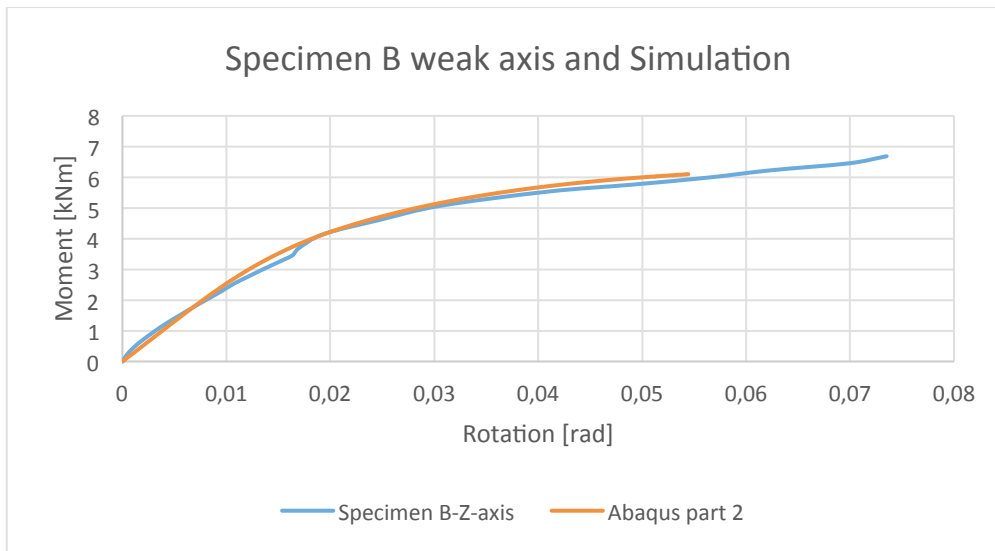
Figure 11.4: Specimen B bending about the weak axis with 2 C3D20R and C3D8R

Based on the results from this parameter study, the use of the element C3D20R was totally abandoned.

11.3 Resolution for the bulging deformation on the RHS profile.

In this investigation, different element combinations between the end plate and the RHS profile were studied in order to optimize the accuracy for the simulation models. This is done by comparing the analysis that produces bulging RHS profile and the ones without. So as to see if the numerical models with bulging RHS profile, which were used in this numerical investigations did affect the final results obtained presented on chapter 9.2.5.

Specimen B, bending about the strong axis was initially chosen in this case due to providing poorer results compared to the rest based results as shown on table 10.5.

Therefore two models were made. The first and the second model has an end plate with 4 elements of C3D8R. The main difference is that first model has 1 element of C3D8R on RHS profile as shown on figure 9.17 while the second model has 2 as shown on figure 9.19.

Another denotation of the first and the second model is 4Q8-1Q8 and 4Q8-2Q8. Note that 4Q8-1Q8 is the same simulation model that was used in 10.2.2 and its results are shown on table 10.4 and again on table 11.6.

11.3.1 Results

Figure 11.5 shows relationship between the response curves obtained from the experiment with 4Q8-2Q8 and 4Q8-1Q8. The values are depicted on table 11.5 and 11.6
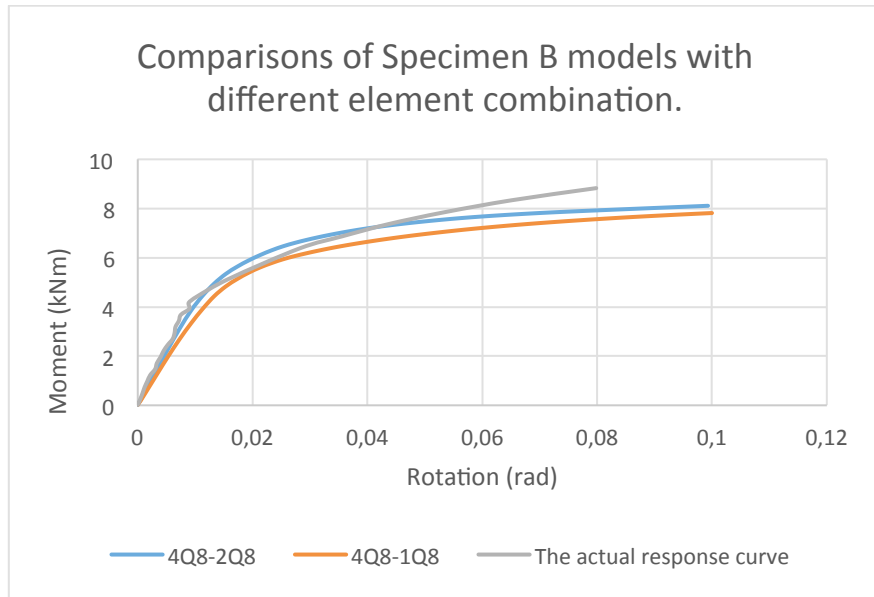

Figure 11.5: Specimen B with different element combinations

	4Q8-1Q8	4Q8-2Q8	Experimental Value
Capacity $[kNm]$	7,8	8,1	8,8
Capacity Utilization $\left[\dfrac{M_p}{M_{max}}\right]$	0,88	0,92	-

Table 11.5: The capacity comparisons

	4Q8-1Q8	4Q8-2Q8	Experimental Value
Initial stiffness $[kNm/rad]$	375	430	594
Stiffness Utilization $\left[\dfrac{S_{j,ini}}{S_{j,ini\ Response}}\right]$	0,63	0,72	-

Table 11.6: The initial stiffness comparisons

Based on the results shown on table 11.5 and 11.6, the 4Q8-2Q8 model gives higher stiffness and capacity utilization. The bulging deformation of the RHS profile obtained by 4Q8-1Q8 gives 10 % less accurate results compared to 4Q8-2Q8. Although the computational time is longer for the 4Q8-2Q8, the 4Q8-1Q8 model provides adequate results at shorter time.

Therefore the Abaqus models of 4Q8-2Q8, which was used initially to conduct numerical analysis in this investigation is a preferable model that gave reasonable numerical results as depicted on chapter 10.

12 Conclusion

12.1 Capacity calculations

Based on the available data depicted on table 12.1, the hand calculations overestimates the capacity when Specimen A is subjected to bending about the weak axis. In other words the analytical results are leaning on the conservative side. As for the bending about the strong axis for Specimen A, the hand calculations underestimates the capacity by 21 %. Therefore the analytical calculations are conservative for bending about the weak axis and it underestimates the capacity when specimen A is bent about the strong axis. As for specimen B, the hand calculations underestimates the capacities when Specimen B is subjected to bending about the weak and the strong axis.

Overall from this investigation, the hand calculations produced good estimations of the specimens' capacities when bent about the weak axis. However, it underestimates the estimations of the capacities when bent about the strong axis. Therefore the hand calculation model, which is based on Eurocode leans on the conservative side for weak axis estimations

Table 8.5 shows the capacity utilization of each specimens when bent about the weak and strong axis.

Specimen	Bending about an axis	Capacity Utilization $\dfrac{M_p}{M_{max}}$
Specimen A	Weak	1,1
Specimen A	Strong	0,79
Specimen B	Weak	0,87
Specimen B	strong	0,64

Table 12.1: The capacity utilization of moment capacity and the ultimate moment

12.2 The rotational stiffness calculations

Based on the available data depicted on chapter 8, the hand calculations overestimates the initial stiffness when Specimen A is subjected to bending about the weak axis and the strong axis. In other words the analytical results are leaning on the conservative side for specimen A.

As for the bending about the weak axis for Specimen B, the initial stiffness obtained analytically underestimates the experimental (response) initial stiffness by 10 %. This is the opposite case for the initial rotational stiffness when specimen B bends about the strong, as it overestimates

Therefore the analytical calculations are conservative for both bending axes for specimen A when dealing with initial stiffness. On the other hand, the hand calculation overestimates the strong axis estimation and underestimates the weak axis estimation when it comes to specimen B.

Since specimen A has more pinned qualities compared to specimen B as observed on chapter 6.3, the hand calculations tend to give the conservative stiffness results in comparison to the results obtained from the laboratory tests.

13 Bibliograpy

[1] CEN, "Eurocode 3: Design of steel structures Part 1-8: Design of joints," Standard Norway, 2005.

[2] F. T. Karlsen, "Knutepunkter for staver med hulprofiltverrsnitt," NTNU, Trondheim, 2011.

[3] K. Lauknes, "Beregninger av endeplateforbindelser i høyfast stål," NTNU, Trondheim, 2013.

[4] B. E. Egeland and I.-M. Torstvedt, "Stivhet til endeplateforbindelser i hulprofil," NTNU, Trondheim, 2013.

[5] K.-A. Knutsen and T. Oma, "Forsøk og stivhetsberegninger for hulprofil-endeplateskjøt," NTNU, Trondheim, 2014.

[6] I. Birkeland, "Knutepunkter i bygningen," NTNU, Trondheim, 2011.

[7] A. M. Uhre, "Hulprofil med endeplateforbindelse," NTNU, Trondheim, 2014.

[8] T. Bringsvor, "Oppførsel til momentbelastede knutepunkter for hulprofiler," NTNU, Trondheim, 2015.

[9] E. E. Kirkerud, "Endeplateforbindelser for rektangulære," NTNU, Trondheim, 2015.

[10] P. K. Larsen, Dimensjonering av stålkonstruksjoner. 2nd.edition, Trondheim: Akademisk forlag, 2010.

[11] M. Braestrup, "Yield line theory and concrete plasticity," no. 8, pp. 1-5, 2008.

[12] P. i. A. Vrouwenvelder and P. i. J. Witteveen, "The plastic behaviour and the calculation of plates subjected to bending," 2003.

[13] R. Park and W. L. Gamble, "Reinforced concrete slabs," 2000, p. 211.

[14] K. Weynand, J.-P. Jaspart and M. Steenhuis, "The stiffness Model of revised Annex J of Eurocode 3," 1996.

[15] A. G. Coelho and F. Bijlaard, "Behaviour of high strength steel moment joints," 2010.

[16] X. Qiang, F. S. Bijlaard and H. Kolstein, "Elevated-temperature mechanical properties of high strength structural steel S460," 2012.

[17] G. Shi, Y. Shi, H. Ban and Y. Wang, "Research progress on the mechanical property of high strength structure steels," 2011.

[18] E. Gogou, "Use of high strength steel grades for economical bridge design," Delft university of technology, Delft, 2012.

[19] A. M.Coelhoa and F. S. Bijlaard, "Experimental behaviour of high strength steel end-plate connections," 2006.

[20] CEN, "Eurocode 3: Design of steel structures Part 1-12: Construction with high steel grades upto S 700," Standard Norway, 2007.

[21] CEN, "Eurocode 3: Design of steel structures Part 1-1: General rules and rules for buildings," Standard Norway, 2005.

[22] X. Qiang, X. Jiang, F. S. Bijlaard, H. Kolstein and Y. Luo, "Post-fire behaviour of high strength steel endplate connections — Part 1:Experimental study," 2014.

[23] A. Heidarpour, N. S. T. A. H. Korayem, X.-L. Zhao and C. R. Hutchinson, "Mechanical properties of very high strength steel at elevated temperatures," 2014.

[24] P. K. Larsen, A. H. Clausen and A. Aalberg, "Profiler og formler," in *Stålkonstruksjoner*, tapir akademisk forlag.

[25] A. Aalberg, A. Uhre and P. K. Larsen, "End plate connections for rectangular hollow section in bending," 2015.

[26] M. I. o. Technology. [Online]. Available: http://web.mit.edu/calculix_v2.7/CalculiX/ccx_2.7/doc/ccx/node30.html.

[27] R. Cook and W. Young, Advanced Mechanics of Materials – 2nd ed, Essex: Pearson education, 1999.

Appendix

A Detail drawings of the specimens A and B used in the laboratory

A.1 Specimen A and B for test object 1 (weak axis)/ AA

These are the detail drawings for the test object 1 as shown on figure 5.7, which was conducted for both specimens when bent about weak.
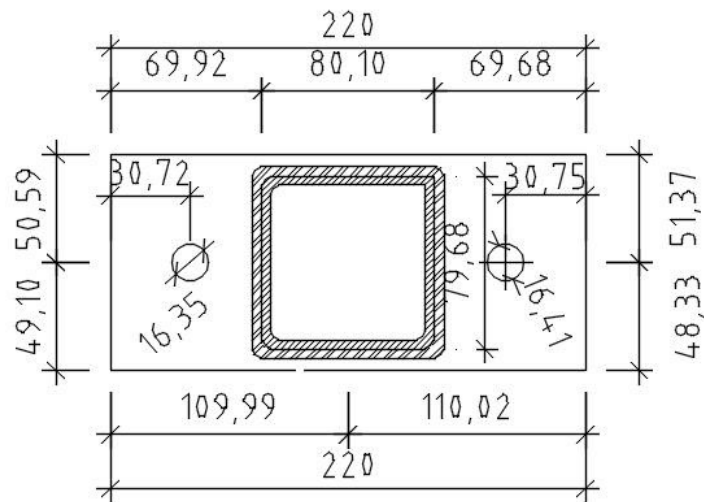

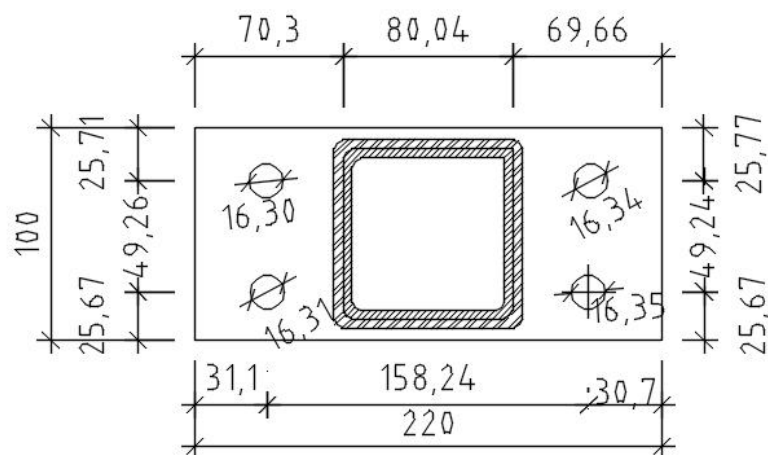**Figure A.1: Detail drawing of specimen A, weak axis**

Figure A.2: Detail drawing of specimen B, weak axis

A.2 Specimen A and B for test object 2 (strong axis)/ RG

The diagram shown on figure 5.7, which was conducted for both specimens when bent about the strong axis.
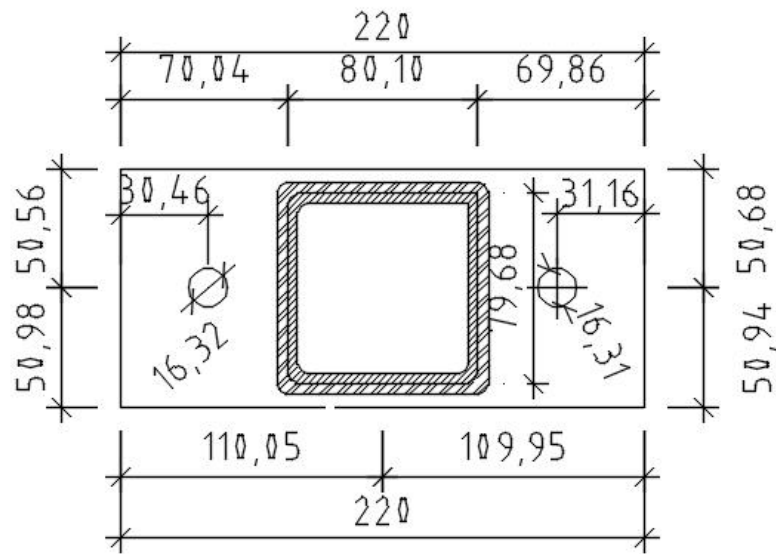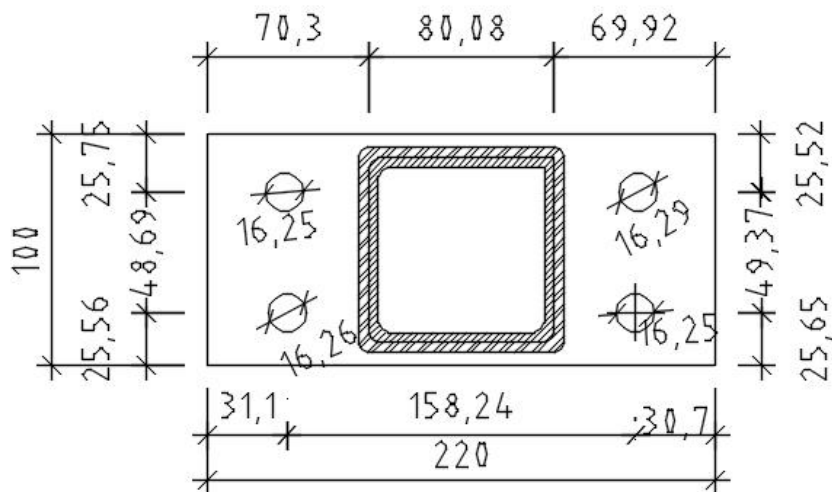
Figure A.3: Detail drawing of specimen A, strong axis

Figure A.4: Detail drawing of specimen B, strong axis

B Deduction of virtual work expressions

The formulation of the moment plastic capacity expressions are based on the principle of virtual work. These expressions were presented in chapter 7 and the appendix shows how these expressions were obtained.

B.1 Cantilever beam subjected to point load

When a cantilever beam is subjected to a point load P at length L. If P exceeds the moment capacity M_p, the permanent deformations occurs as shown on figure (B.1)
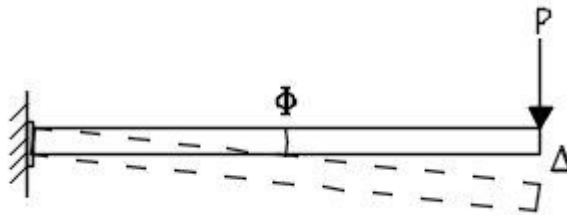

Figure B.1: Point load

P causes the deflection Δ at the tip of the beam and the angle $\emptyset$ to develop. The principle of virtual work is applied in this situation whereby the external work W_{ext} is equal to $P\Delta$ and the internal work is equal to $M_p\emptyset$. The virtual is principle is then applied when the internal is equivalent to the external work as demonstrated on B.1

$$W_{int} = W_{ext} \tag{B. 1}$$

$$M_p\emptyset = P\Delta \tag{B. 2}$$

$$M_p\frac{\Delta}{L} = P\Delta \tag{B. 3}$$

$$P = \frac{M_p}{L} \tag{B. 4}$$

This situation is same applied to the connections, which were bolted to a rigid wall as demonstrated in chapter 5 and shown on figure (6.12).

The figure (B.1) is a simplification of the connection of figure (B.2), which displays the equilibrium of the moment at the connection.
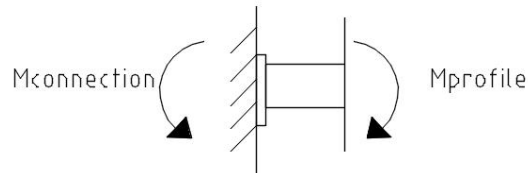

Figure B.2: Figure of the connection with acting moments

The sum of moment at the equilibrium $\sum M = 0$, leads to the moment from the profile being equal to the moment which is transmitted to the connection. This expression is shown at B.5.

$$M_{connection} = M_{profile} \tag{B. 5}$$

This situation is the basis of the moment equilibrium at the connection of different specimens shown on (B.1) and (B.2) when they are bent about the strong axis and weak axis. In the case of end plate connections the value $m_x = m$ when determining the design resistance of the T-stub according to the Eurocode (reference).

B.2 Deduction of the moment plastic capacity M_p expression

This chapter shows how M_p for each specimens were deducted.

B.2.1 Specimen A: Bending about the strong axis

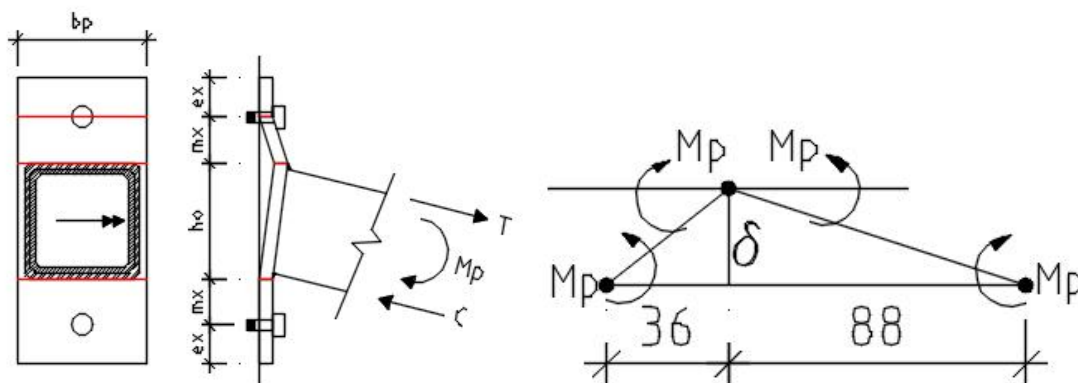In this case, m and h_o is 36 mm and 88 mm.

Figure B.3: Specimen A, bending about the strong axis

$$W_{ext} = W_{int}$$

$$M_{profile} = M_{connection}$$

$$M_p \emptyset = \sum m_p \, l \, \theta$$

$$M_p \frac{\delta}{h_0} = m_p b_p \frac{\delta}{m} + m_p b_p \left(\frac{\delta}{m} + \frac{\delta}{h_0} \right) + m_p b_p \frac{\delta}{h_0}$$

$$M_p \frac{\delta}{h_0} = 2 m_p b_p \delta \left(\frac{1}{m} + \frac{1}{h_0} \right)$$

$$M_p \frac{\delta}{h_0} = 2 m_p b_p \frac{\delta}{h_0} \left(\frac{h_0}{m} + 1 \right)$$

$$M_p = 2 m_p b_p \left(\frac{h_0}{m} + 1 \right) \qquad\qquad (\text{B. 6})$$

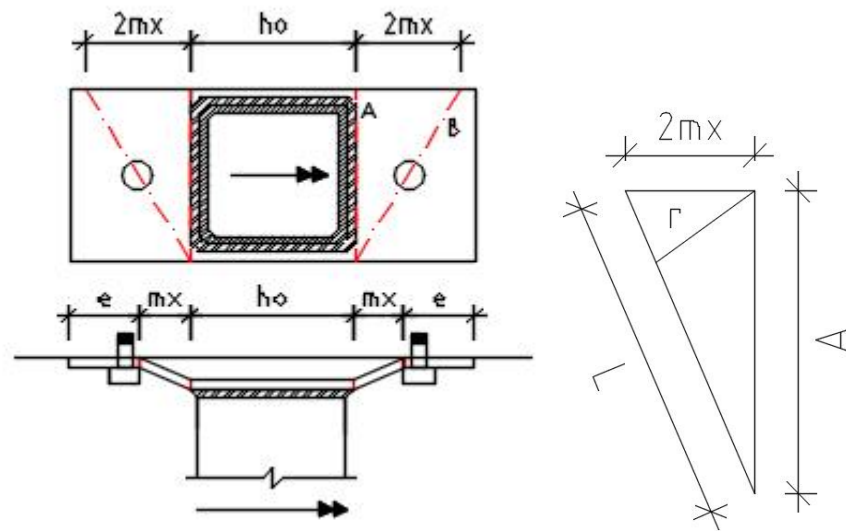### B.2.2 Specimen A: Bending about the weak axis

Figure B.4: Specimen A, bending about the weak axis

L is the length of the slanted yield line B as demonstrated by the dotted line on figure (B.4) and r is the line which is perpendicular to line L. The expression for line L is shown on the equation below and the expression for r is obtained from sinus relation as shown on figure (B.4) and its expression is shown below. The yield line A is equivalent to b_p, which is the length of the end plate.

$$L = \sqrt{(2m)^2 + b_p^2} = \sqrt{4m^2 + b_p^2}$$

$$sin\alpha = \frac{2m}{L} = \frac{r}{b_p}$$

$$r = \frac{2mb_p}{L}$$

$$W_{ext} = W_{int}$$

$$M_p \emptyset = \sum m_p \, l \, \theta$$

$$M_p \frac{\delta}{b_p} = 2b_p m_p \frac{\delta}{2m} + 2m_p L \frac{\delta}{r}$$

$$\frac{M_p}{b_p} = \frac{b_p m_p}{m} + \frac{2m_p L}{r}$$

6

$$M_p = \frac{2b_p}{m}\left(b_p^2 + 2m^2\right) \tag{B. 7}$$

B.2.3 Specimen B: Bending about the weak axis

Specimen B has three possible mechanisms, which are demonstrated on figure (B.5)
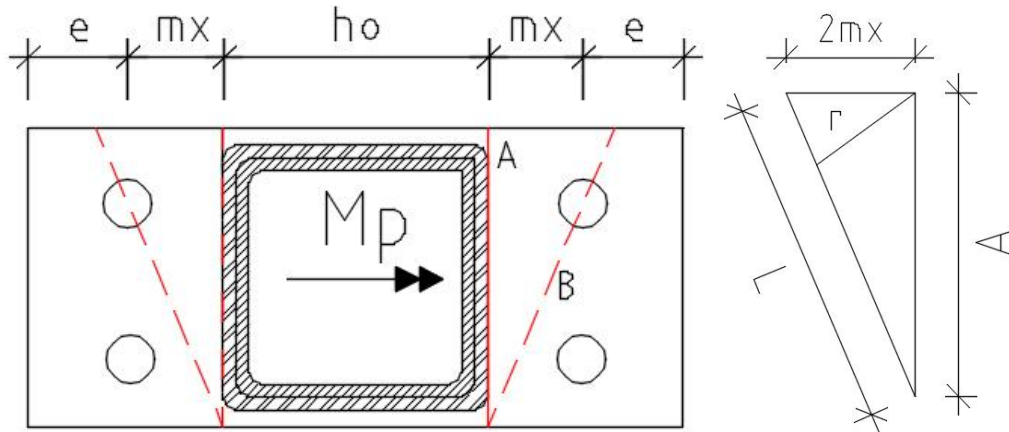
B.2.3.1 Yield Mechanism 1

Figure B.5: Yield mechanism 1

$$M_p = \frac{2b_p}{m}\left(b_p^2 + 2m^2\right) \tag{B. 8}$$

B.2.3.2 Yield Mechanism 2

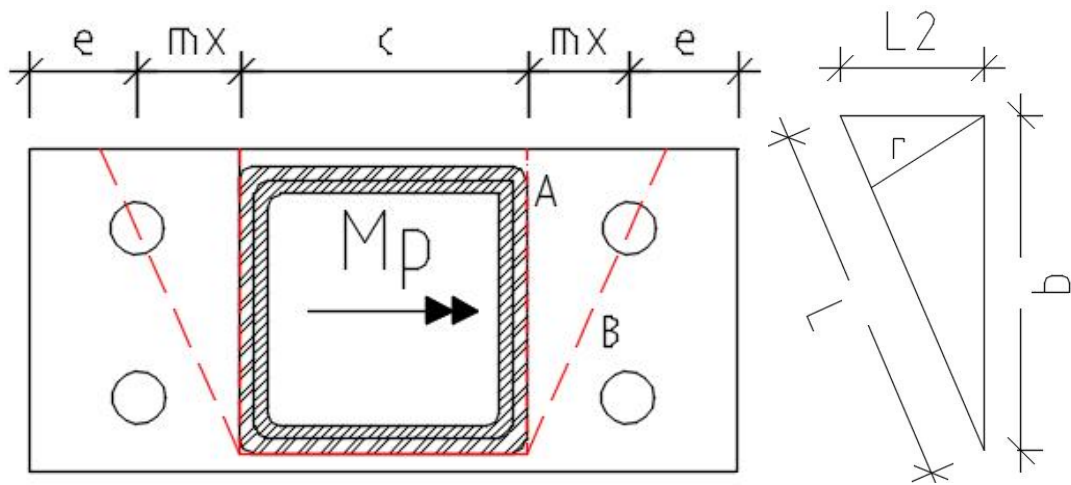The line r is not a yield line, it's a length from the centre of the bolt to the corner of L_2 and b.

Figure B.6: Yield mechanism 2

$$W_{ext} = W_{int}$$

$$M_p \emptyset = \sum m_p \, l \, \theta$$

$$L = \sqrt{L_2^2 + b^2} = 106 \, mm$$

$$r = b_p \sin\left(tan^-\left[\frac{m_x}{b-e}\right]\right) = 44 \, mm$$

$$L_2 = b_p \tan(tan^- (m/b - e)) = 49 \, mm$$

$$M_p \frac{\delta}{b} = 2bm_p \frac{\delta}{L_2} + 2m_p L \frac{\delta}{r} + m_p c \frac{\delta}{b}$$

$$M_p = m_p \left[(c + \frac{2Lb}{r} + \frac{2\,b^2}{L_2} \right] \qquad (B.\,9)$$

B.2.3.3 Yield Mechanism 3

The line r is a yield line from the centre of the bolt to the intersection between m_x and yield line A.
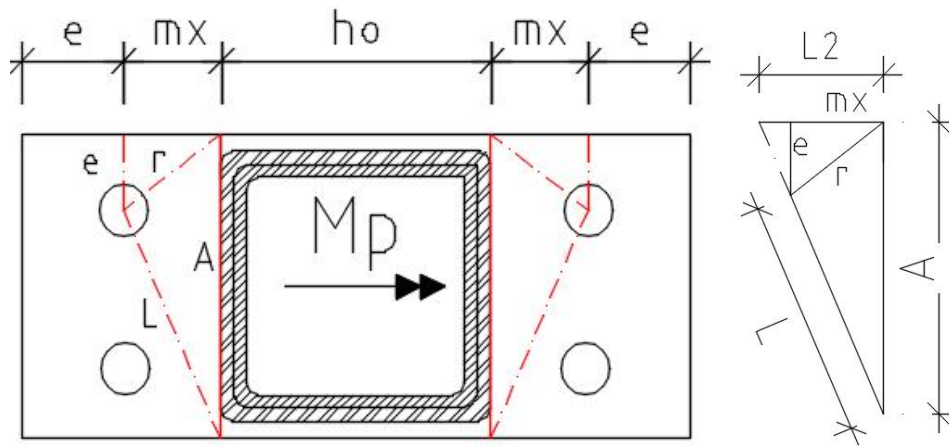

Figure B.7: Yield mechanism 3

$$r = b_p \sin\left(tan^-\left[\frac{m_x}{b-e}\right]\right) = 46 \; mm$$

$$L_2 = b_p \; \tan(tan^-\,(m/b-e)) = 53 \; mm$$

$$W_{ext} = W_{int}$$

$$M_p \emptyset = \sum m_p \, l \, \theta$$

$$M_p \frac{\delta}{b_p} = \frac{2m_p b_p \delta}{L_2} + \frac{2m_p e}{m} + \frac{2m_p L}{r} + \frac{2m_p m}{e} + \frac{2m_p e}{m}$$

$$M_p = 2m_p b_p \left(\frac{e}{m} + \frac{b_p}{L_2} + \frac{L}{r} + \frac{m}{e} + \frac{e}{m}\right) \qquad\qquad (B.\,10)$$

C Effective lengths obtained virtual work

The effective lengths shown in this section were used to calcite the initial stiffness of the specimens. The effective length for the strong axis is obtained from the Eurocode and the effective lengths for the weak axis is derived from the moment plastic capacity expression and the expression 4.7. These expressions were deduced by Bringsvor for specimen A and Kirkerud for specimen B.

C.1 Specimen A

Strong axis bending (Formula obtained from the Eurocode for pure tension).

$$l_{eff} = \frac{b_p}{2} = 50mm \tag{B. 11}$$

Weak axis bending (formula obtained from the virtual work)

$$M_p = \frac{2m_p}{m_x}\left[b_p^2 + 2m_2^x\right] <=> M_p = F_p\frac{2}{3}b_p$$

$$3\frac{m_p}{m_x}\frac{1}{b_p}\left[b_p^2 + 2m_x^2\right]$$

$$F_P = 3m_p\left[\frac{b_p}{m_x} + \frac{2m_x}{b_p}\right]$$

$$F_{T,Rd} = F_p$$

$$F_p = \frac{4m_p l_{eff}}{m_x} = 3m_p\left[\frac{b_p}{m_x} + \frac{2m_x}{b_p}\right]$$

$$l_{eff} = \frac{m_x}{4m_p}3m_p\left[\frac{b_p}{m_x} + \frac{2m_x}{b_p}\right]$$

$$l_{eff} = 0{,}75b_p + 1{,}5\frac{m_x}{b_p} \tag{B. 12}$$

10

C.2 Specimen B

Strong axis bending

$$l_{eff} = \frac{b_p}{2} = 50mm \tag{B. 13}$$

Weak axis bending

$$M_p = F_p \frac{2}{3} b_p$$

$$F_P = 3M_P \left[\frac{b_p}{m_x} + \frac{2m_x}{b_p} \right]$$

$$l_{eff} = \frac{1}{2z} \left[b_p^2 + 2m^2 \right] \tag{B. 14}$$

D Capacity control for the specimens' components

In this section the capacity of the bolt, end plate, weld and the hollow profile are controlled. It is controlled so that the capacity of the end plate must be lower than other components in the cross section. The outcome is that the end plate yields first, which is the main interest in this investigation.

D.1 Specimen A

D.1.1 Strong axis bending

Capacity control:

$$H = m_x + h_0 = 36 + 88 = 124 \; mm$$

$$Tension \; Capacity = \frac{M_p}{H}$$

$$m_X = 36 \; mm$$

$$e_x = 30 \; mm$$

$$f_y = 700 Mpa$$

Effective length with circular patterns $l_{eff,cp}$		Effective length with non-circular $l_{eff,nc}$		
$\dfrac{2\pi m_x}{2}$	$\dfrac{\pi m_x + 2e}{2}$	$\dfrac{4m_x + 1{,}25e_x}{2}$	$\dfrac{e + 2m_x + 0{,}625e_x}{2}$	$0{,}5b_p$
113 mm	87 mm	91 mm	61 mm	50 mm

Table D.1: The effective length of the end plate

The least value of table from the Eurocode is $l_{eff} = 50 \; mm \; t_p^2 = 6mm$

$$m_p = 0{,}25 l_{eff} t_p^2 f_y = 315000 Nmm$$

$$F_{t,1,Rd} = \frac{4M_{pl,Rd}}{m} = \frac{4 * 315000}{36} = 35 kN$$

$$F_{t,2,Rd} = \frac{2M_{pl,Rd} + n \sum F_{Rd}}{m + n} = \frac{2 * 315000 + 30 * 90432}{36 + 30} = 50{,}7 kN$$

$$F_{t,3,Rd} = \sum F_{t,Rd} = \frac{k_2 f_{ub} A_s}{\gamma_{m2}} = 90{,}4 kN$$

12

$$t_p = 6mm: \min\{F_{t,1,Rd}F_{t,2,Rd}F_{t,3,Rd}\} = 35kN$$

End plate capacity:

Plate thickness t_p (mm)	$M_p(kNm)$	Point Load (kg)
6	4,34	177

$$S = \frac{M_P}{H} = \frac{4,34 * 10^6}{124} = 35kN \leq F_{t,Rd} = 35kN$$

Hollow profile capacity:

$$M_{pl,Rd} = \frac{W_{pl}f_y}{\gamma_{m0}} = \frac{34,3 * 10^3 * 355}{1,05} = 11,6kNm$$

$$S = 4,34kNm \leq M_{pl,Rd} = 11,6kNm$$

Weld capacity:

$$F_{w,Ed} \leq F_{w,Rd}$$

$$F_{w,Rd} = f_{vw,d} * a$$

$$F_{w,Rd} = \frac{f_u/\sqrt{3}}{\beta_w\gamma_{m2}}2a$$

$$F_{w,Rd} = \frac{510/\sqrt{3}}{0,9 * 1,25} * 2 * 4 = 2094N \approx 2,1kN$$

$$F_{w,Ed} = \frac{M_p}{L} = \frac{4,34 * 10^6}{2500} = 1736N$$

$$F_{w,Ed} = 1736N < F_{w,Rd} = 2094\ N$$

D.1.2 Weak axis bending

$$M_p = \frac{2b_p}{m}\left(b_p^2 + 2m^2\right)$$

$$m_p = 0{,}25t_p^2 f_y$$

Plate thickness t_p (mm)	$M_p (kNm)$	Point Load (kg)
6	4,41	180

Bolt capacity:

$$F_{t,Rd} = \frac{k_2 f_{ub} A_S}{\gamma_{M2}} \geq F_{t,Ed} = 1{,}3\frac{M_p}{b_p}$$

$$F_{t,Rd} = \frac{0{,}9 * 800 * 157}{1{,}25} = 90{,}4kN \geq F_{t,Ed} = \frac{1{,}3 * 4{,}41 * 10^6}{100} = 57{,}33kN$$

Hollow profile capacity:

$$S = 4{,}41\ kNm \leq M_{pl,Rd} = 11{,}6kNm$$

Weld Capacity:

<div align="center">

NS EN 1993-1-8:4.5.3.3

</div>

$$F_{w,Ed} \leq F_{w,Rd}$$

$$F_{w,Ed} = 1764N < F = 2094N$$

D.2 Specimen B

D.2.1 Weak axis bending

D.2.2 Yield Mechanism 1

$$M_p = \frac{2b_p}{m}\left(b_p^2 + 2m^2\right)$$

$$m_p = 0{,}25t_p^2 f_y$$

Plate thickness t_p (mm)	$M_p(kNm)$	Point Load (kg)
6	4,4	191

D.2.3 Yield Mechanism 2

$$W_{ext} = W_{int}$$

$$M_p \emptyset = \sum m_p \, l \, \theta$$

$$M_p = m_p\left[\left(c + \frac{2Lb}{r} + \frac{2\,b^2}{L_2}\right)\right]$$

$$L = 108\ mm, c = 88mm, b = 94\ mm, L_2 = 46\ mm$$

Plate thickness t_p (mm)	$M_p(kNm)$	Point Load (kg)
6	5,8	248

Bolt capacity

$$F_{t,Rd} = \frac{k_2 f_{ub} A_S}{\gamma_{M2}} \geq F_{t,Ed} = 1{,}3\frac{M_p}{b_p}$$

$$F_{t,Rd} = \frac{0{,}9 * 800 * 157}{1{,}25} = 90{,}4kN \geq F_{t,Ed} = \frac{1{,}3 * 5{,}4 * 10^6}{100} = 70{,}2\ kN$$

Hollow profile capacity:

$$S = 5{,}4\ kNm \leq M_{pl,Rd} = 11{,}6kNm$$

Weld Capacity:

<div align="center">

NS EN 1993-1-8:4.5.3.3

$$F_{w,Ed} \le F_{w,Rd}$$

$$F_{w,Ed} = 1840N < F = 2094N$$

</div>

D.2.4   Yield Mechanism 3

$$W_{ext} = W_{int}$$

$$M_p \emptyset = \sum m_p \, l \, \theta$$

$$M_p = 2m_p b_p \left(\frac{e}{m} + \frac{b_p}{L_2} + \frac{L}{r} + \frac{m}{e} + \frac{e}{m} \right)$$

$$L = 90mm, r = 46mm$$

Plate thickness t_p (mm)	$M_p(kNm)$	Point Load (kg)
6	8,4	364

<div align="center">

Bolt capacity

$$F_{t,Rd} = \frac{k_2 f_{ub} A_S}{\gamma_{M2}} \ge F_{t,Ed} = 1{,}3 \frac{M_p}{b_p}$$

$$F_{t,Rd} = \frac{0{,}9 * 800 * 157}{1{,}25} = 90{,}4kN \le F_{t,Ed} = \frac{1{,}3 * 8{,}4 * 10^6}{100} = 109 \; kN$$

</div>

Bending moment Hollow profile:

$$M_{pl,Rd} = \frac{W_{pl} f_y}{\gamma_{m0}} = \frac{34{,}3 * 10^3 * 355}{1{,}05} = 11{,}6kNm$$

$$S = 8{,}4 \; kNm \le M_{pl,Rd} = 11{,}6kNm$$

Weld Capacity:

<div align="center">

NS EN 1993-1-8:4.5.3.3

$$F_{w,Ed} \le F_{w,Rd}$$

$$F_{W,Ed} = \frac{M_p}{L} = \frac{8{,}4 * 10^6}{2500} = 3360 \; N$$

$$F_{w,Ed} = 2780N < F = 3369 \; N \; \; Not \; ok$$

</div>

D.2.5 Results

Configurations	Strong axis	Weak axis
Geometry 1	M16:8,8	M16:8,8
Geometry 2	M16:8,8	-
Geometry 2 yield mech 1		M16:8,8
Geometry 2 yield mech 2		M16:8,8
Geometry 2 yield mech 3		M16:8,8

E   Stiffness Calculations

Stiffness Coefficients for basic components

End plate in bending (for a single bolt row)

$$k_5 = \frac{0,9 l_{eff} t_p^3}{m^3}$$

Bolt in tension (for a single bolt row)

$$k_{10} = \frac{1,6 A_s}{L_b}$$

Numerical Values:

$$L_{eff} \ mode \ 1 \ and \ mode \ 2 = 50 \ mm$$

$$m_x = 36mm$$

$$A_s = 157 \ mm^2$$

$$L_b = \frac{t_h + t_n}{2} + 2t_w + t_p + t_p = \frac{10 + 13}{2} + 2*3 + 6 + 30 = 53,5mm$$

E.1 Specimen A

E.1.1 Bending in the strong axis

$$l_{eff} = \frac{b_p}{2} = 50mm$$

$$k_5 = \frac{0,9 * 50 * 6^3}{36^3} = 0,208 \ mm$$

$$k_{10} = \frac{1,6 * 157}{53,5} * \frac{1}{2} = 2,350mm$$

$$k_{tot} = \frac{1}{\frac{1}{k_5} + \frac{1}{k_{10}}} = 0,191mm$$

$$S_j = \frac{Ez^2}{\mu \left[\frac{1}{k_5} + \frac{1}{k_{10}} \right]}$$

$$S_{j,ini} = K_{tot}Ez^2$$

$$S_{j,ini} = 0,191 * 210000 * 120^2 = 578kNm/rad$$

E.1.2 Bending in the weak axis

$$l_{eff} = 0,75b_p + 1,5\frac{m_x}{b_p}$$

$$l_{eff} = 0,75 * 100 + 1,5\frac{36^2}{100} = 94,0mm$$

$$k_5 = \frac{0,9 * 94 * 6^3}{36^3} = 0,392 \ mm$$

$$k_{10} = \frac{1,6 * 157}{53,5} = 4,695 \ mm$$

$$k_{tot} = \frac{1}{\frac{1}{0,392} + \frac{1}{4,695}} = 0,362 \ mm$$

$$S_j = \frac{Ez^2}{\mu \sum_i \frac{1}{k_i}}$$

$$S_{j,ini} = K_{tot}Ez^2$$

$$S_{j,ini} = 0{,}362 * 210000 * \left(\frac{2}{3} * 100\right)^2 * 10^{-6} = 338 \ kNm/rad$$

E.2 Specimen B

E.2.1 Bending in the strong axis

$$l_{eff} = \frac{b_p}{2} = 50mm$$

$$k_5 = \frac{0{,}9 * 50 * 6^3}{36^3} = 0{,}208 \ mm$$

$$k_{10} = \frac{1{,}6 * 157}{53{,}5} = 4{,}695 \ mm$$

$$k_{tot} = \frac{1}{\dfrac{1}{0{,}208} + \dfrac{1}{4{,}695}} = 0{,}199mm$$
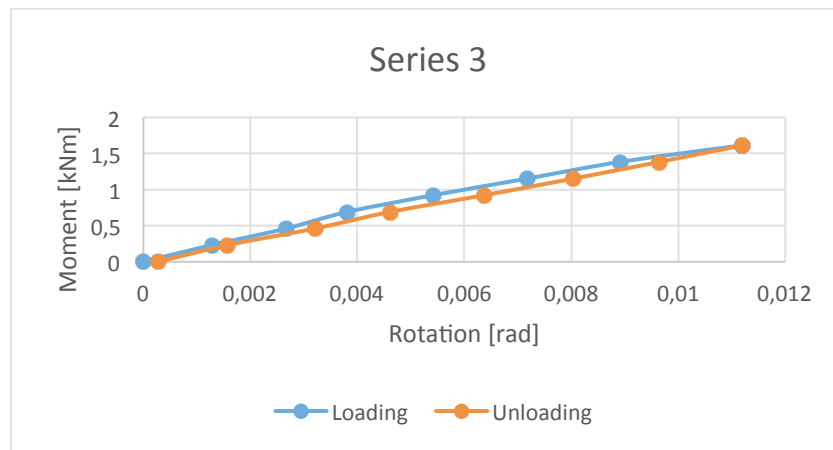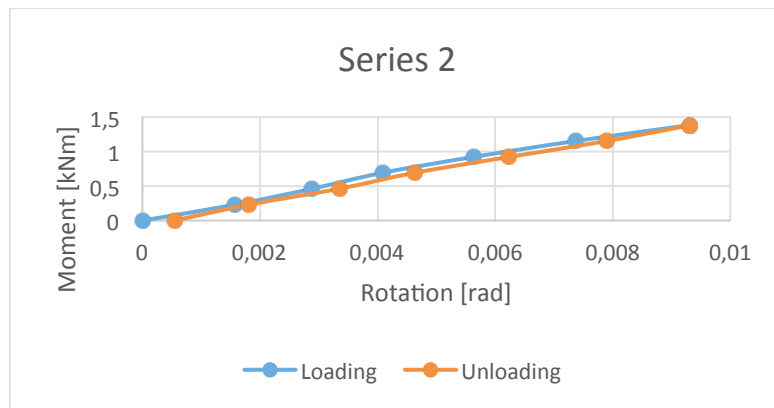
$$S_j = \frac{Ez^2}{\mu\left[\dfrac{1}{k_5} + \dfrac{1}{k_{10}}\right]}$$

$$S_{j,ini} = K_{tot}Ez^2$$

$$S_{j,ini} = 0{,}199 * 210000 * 120^2 = 602 \ kNm/rad$$

E.2.2 Bending in the weak axis

E.2.2.1 Yield mechanism 1

$$l_{eff} = \frac{1}{2z}\left[b_p^2 + 2m^2\right]$$

$$l_{eff} = \frac{1}{2 * 66{,}7}\left[100^2 + 2 * 36^2\right] = 94{,}4mm$$

$$k_5 = \frac{0{,}9 * 94{,}4 * 6^3}{36^3} = 0{,}393 \ mm$$

$$k_{10} = \frac{1{,}6 * 157}{53{,}5} = 4{,}695 \ mm$$

$$k_{tot} = \frac{1}{\dfrac{1}{0{,}393} + \dfrac{1}{4{,}695}} = 0{,}363 \ mm$$
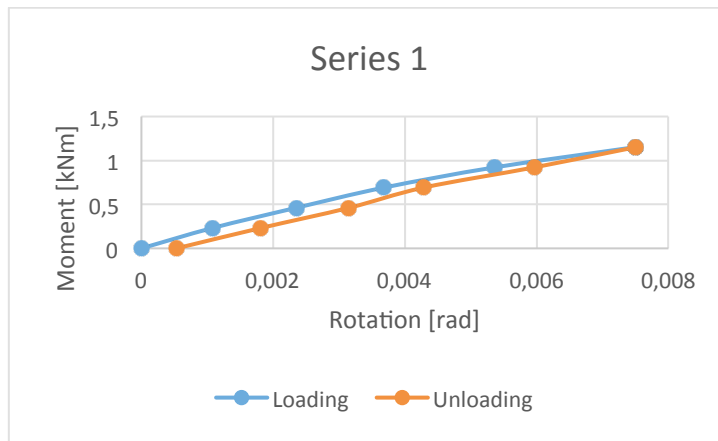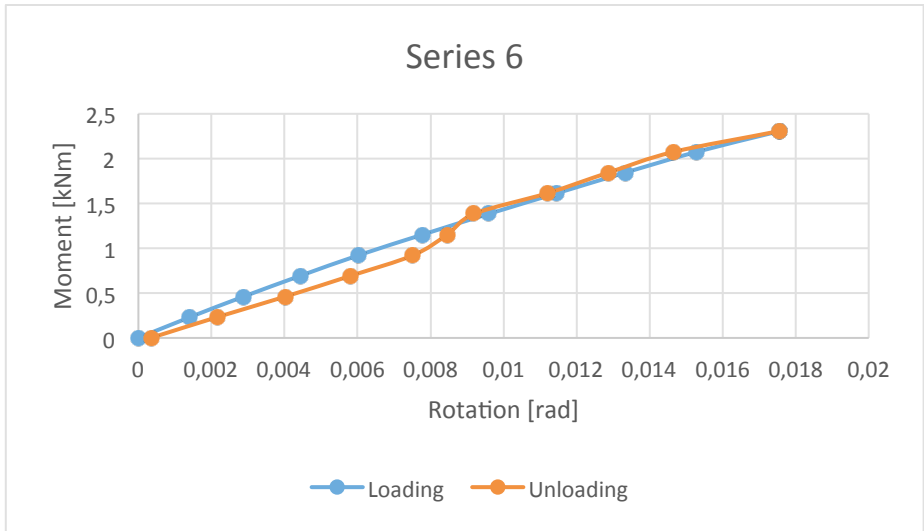
$$S_j = \frac{Ez^2}{\mu \sum_i \dfrac{1}{k_i}}$$
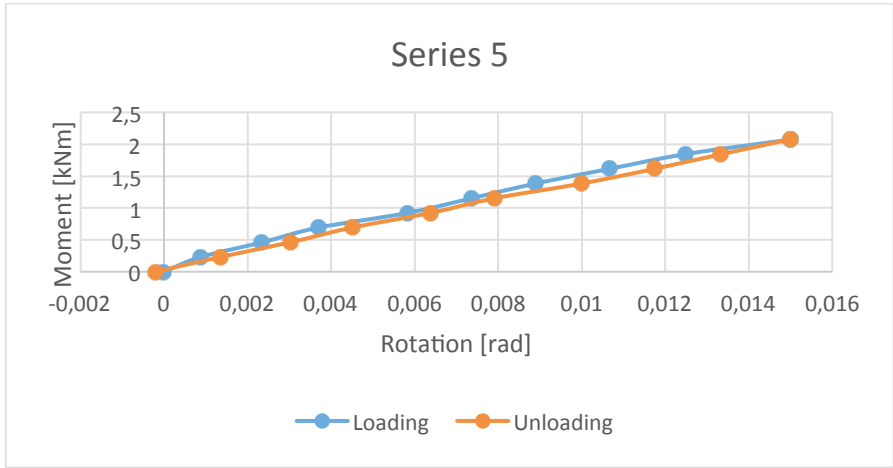
$$S_{j,ini} = K_{tot}Ez^2$$

19

$$S_{j,ini} = 0{,}363 * 210000 * \left(\frac{2}{3} * 100\right)^2 * 10^{-6} = 339 \; kNm/rad$$

E.2.2.2 Yield mechanism 2 and 3

$$F_{T,Rd} = \frac{4M_{pl,Rd}}{m}$$

$$M_{pl,Rd} = Wf_y = \frac{bh^2}{4}\frac{f_y}{\gamma_{mo}} = \frac{l_{eff}}{4}t_p^2\frac{f_y}{\gamma_{mo}}$$

$$M_p = \frac{m_p}{m}(b^2 + L^2 + mc)$$

$$F_{T,Rd} = \frac{M_p}{z}$$

$$l_{eff} = \frac{1}{2z}(b^2 + L^2 + mc) \le b_p$$

$$l_{eff} = \frac{1}{2 \cdot 66{,}7}(95{,}3^2 + 94{,}5^2 + 36 \cdot 88) = 158 mm \le 100$$

$$l_{eff} = 100 \; mm$$

The effective length is greater than the width of the end plate. Therefore the effective length for this mechanism is 100 mm.

$$F_{T,Rd} = \frac{4M_{pl,Rd}}{m}$$

$$M_{pl,Rd} = Wf_y = \frac{bh^2}{4}\frac{f_y}{\gamma_{mo}} = \frac{l_{eff}}{4}t_p^2\frac{f_y}{\gamma_{mo}}$$

$$M_p = 2m_p b_p \left(\frac{b_p + e}{m} + \frac{L}{r}\right)$$

$$F_{T,Rd} = \frac{M_p}{z}$$

$$l_{eff} = \frac{1}{2z}\left(b_p + e + \frac{mL}{r}\right) \le b_p$$

$$l_{eff} = \frac{1}{2 \cdot 66{,}7}\left(100 + 25 + \frac{36 \cdot 90}{44}\right) = 149 \; mm \le 100$$

$$l_{eff} = 100 \; mm$$

The effective length is greater than the width of the end plate. Therefore the effective length for this mechanism is 100 mm.

$$l_{eff} = \frac{1}{2z}\left[b_p^2 + 2m^2\right]$$

$$l_{eff} = \frac{1}{2*66,7}\left[100^2 + 2*36^2\right] = 94,4mm$$

$$k_5 = \frac{0,9*100*6^3}{36^3} = 0,417 \; mm$$

$$k_{10} = \frac{1,6*157}{53,5} = 4,695 \; mm$$

$$k_{tot} = \frac{1}{\frac{1}{0,417} + \frac{1}{4,695}} = 0,383 \; mm$$

$$S_j = \frac{Ez^2}{\mu\left[\frac{1}{k_5} + \frac{1}{k_{10}}\right]}$$

$$S_{j,ini} = K_{tot}Ez^2$$

$$S_{j,ini} = 0,383*210000*\left(\frac{2}{3}*100\right)^2*10^{-6} = 358 \; kNm/rad$$

F   Resultats from the abaqus

In chapter 6, all the $M - \varphi$ graphs for each series were collected on a single graph as an average. Those graphs are the average of graphs for each series depicted on this chapter.
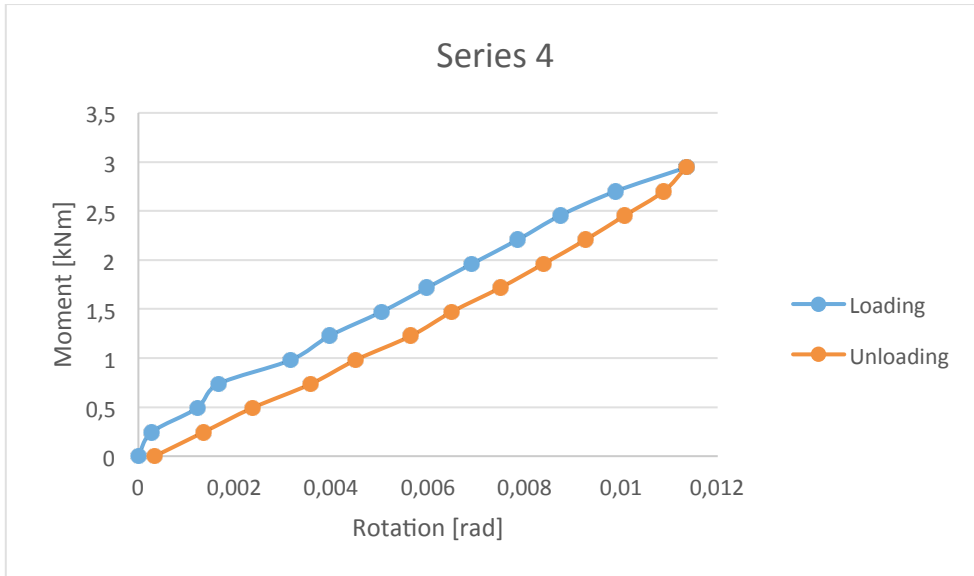
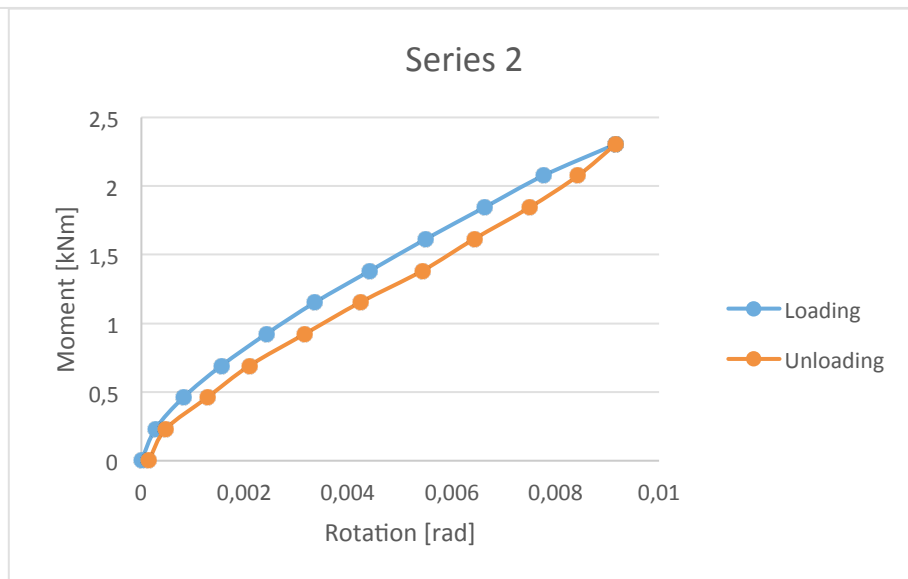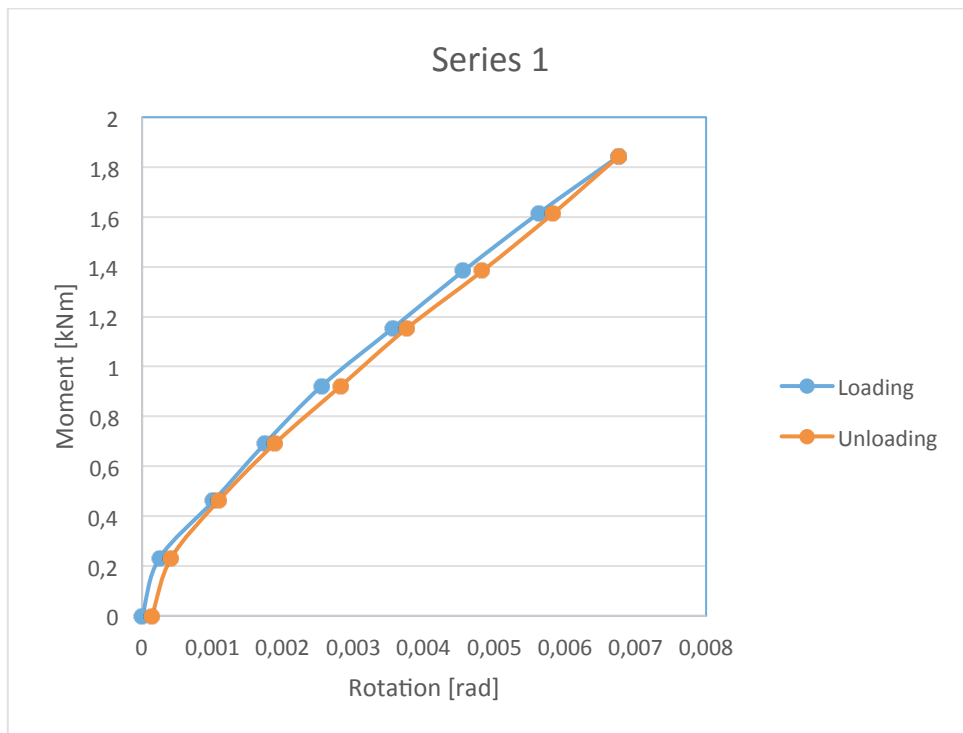## F.1   Specimen A –weak axis

Series 4

Series 5

Series 6

Series 7

Plastic Series 8

F.2 Specimen A – strong axis

Series 1

Series 2

Series 3

F.3 Specimen B – weak axis

Series 5

Plastic-Series 6

F.4 Specimen B –strong axis

Series 1

X-axis: Rotation [kNm]
Y-axis: Moment [kNm]

Legend: Loading, Unloading

Series 2

X-axis: Rotation [rad]
Y-axis: Moment [kNm]

Legend: Loading, Unloading

Series 3

X-axis: Rotation [rad]
Y-axis: Moment [kNm]

Legend: Loading, Unloading

Series 4

Series 5

Plastic Series 6